AD-A048 811 SYSTEMS SCIENCE AND SOFTWARE LA JOLLA CALIF F/G 19/4
NONLINEAR RESPONSE OF BURIED STRUCTURES IN A STRESS WAVE ENVIRO--ETC(U)
JUN 77 J SWEET DNA001-76-C-0103
UNCLASSIFIED SSS-R-77-3215 DNA-4360F NL

| OF |
ADA048811

END
DATE
FILMED
2-78
DDC

AD-E300 067

DNA 4360F

(12)

NONLINEAR RESPONSE OF BURIED STRUCTURES IN A STRESS WAVE ENVIRONMENT

Systems, Science and Software
P.O. Box 1620
La Jolla, California 92038

June 1977

Final Report for Period 29 September 1975—31 May 1977

CONTRACT No. DNA 001-76-C-0103

APPROVED FOR PUBLIC RELEASE;
DISTRIBUTION UNLIMITED.

THIS WORK SPONSORED BY THE DEFENSE NUCLEAR AGENCY
UNDER RDT&E RMSS CODE B344076464 Y99QAXSC06143 H2590D.

Prepared for
Director
DEFENSE NUCLEAR AGENCY
Washington, D. C. 20305

DNA PRINTING PLANT

(18) DNA, SBIE (19) 4360F, AD-E300067

UNCLASSIFIED

SECURITY CLASSIFICATION OF THIS PAGE (*When Data Entered*)

REPORT DOCUMENTATION PAGE

READ INSTRUCTIONS
BEFORE COMPLETING FORM

1. REPORT NUMBER
~~DNA 4360F~~ ✓

2. GOVT ACCESSION NO.

3. RECIPIENT'S CATALOG NUMBER

4. TITLE (*and Subtitle*)
(6) NONLINEAR RESPONSE OF BURIED STRUCTURES IN A STRESS WAVE ENVIRONMENT,

5. TYPE OF REPORT & PERIOD COVERED
Final Report for Period
29 Sep 75 - 31 May 77

6. PERFORMING ORG. REPORT NUMBER
(14) SSS-R-77-3215

7. AUTHOR(s)
(10) J./Sweet

8. CONTRACT OR GRANT NUMBER(s)
(15) DNA 001-76-C-0103

9. PERFORMING ORGANIZATION NAME AND ADDRESS
Systems, Science and Software ✓
P.O. Box 1620
La Jolla, California 92038

10. PROGRAM ELEMENT, PROJECT, TASK AREA & WORK UNIT NUMBERS
NWET Subtask
Y99QAXSC061-43

11. CONTROLLING OFFICE NAME AND ADDRESS
Director
Defense Nuclear Agency
Washington, D.C. 20305

12. REPORT DATE
(11) Jun 77

13. NUMBER OF PAGES
94 (12) 89p.

14. MONITORING AGENCY NAME & ADDRESS (*if different from Controlling Office*)
(9) Final rept. 29 Sep 75–
31 May 77,

15. SECURITY CLASS. (*of this report*)
UNCLASSIFIED

15a. DECLASSIFICATION/DOWNGRADING SCHEDULE

16. DISTRIBUTION STATEMENT (*of this Report*)

Approved for public release; distribution unlimited.

(16) Y99QAXS

17. DISTRIBUTION STATEMENT (*of the abstract entered in Block 20, if different from Report*)

(17) C061

18. SUPPLEMENTARY NOTES

This work sponsored by the Defense Nuclear Agency under RDT&E RMSS Code B344076464 Y99QAXSC06143 H2590D.

19. KEY WORDS (*Continue on reverse side if necessary and identify by block number*)

Finite Element	Structure-Media Interaction
Stress Waves	Cellular Concrete
Nonlinear Response	Reinforced Concrete
Underground Explosions	

20. ABSTRACT (*Continue on reverse side if necessary and identify by block number*)

The theoretical behavior of three buried structural configurations in a stress wave environment has been determined using finite element techniques. The three structures considered are an unlined cylindrical cavity and two thick-walled composite cylinders. Both composite structures are steel lined and each has a thick concrete outer layer; one being cellular concrete and the other reinforced concrete. The impinging wave simulates an underground explosion

DD FORM 1 JAN 73 1473 EDITION OF 1 NOV 65 IS OBSOLETE

UNCLASSIFIED

SECURITY CLASSIFICATION OF THIS PAGE (*When Data Entered*)

388507

20. ABSTRACT (Continued)

and its strength was such that nonlinear behavior occurred in the soil-like surrounding medium (NTS tuff) as well as the composite structures.

PREFACE

This technical report entitled, "Nonlinear Response of Buried Structures in a Stress Wave Environment," is submitted to the Defense Nuclear Agency (DNA). This work was supported by the Defense Nuclear Agency under Contract No. DNA001-76-C-0103. Dr. Kent Goering has been the DNA Contracting Officer. Dr. Joel Sweet has been the Systems, Science and Software (S^3) Project Manager.

TABLE OF CONTENTS

LIST OF ILLUSTRATIONS

LIST OF ILLUSTRATIONS (continued)

LIST OF ILLUSTRATIONS (continued)

CHAPTER I
INTRODUCTION

Three underground cylindrical structures subjected to an impinging time-dependent plane wave have been analyzed in this study. The stress wave is assumed to result from an underground explosion. The structural configurations treated are an unlined cavity, a reinforced concrete-steel liner composite cylinder and a cellular concrete-steel liner composite cylinder. The medium surrounding the structures is a soil-like material (NTS tuff) and the impinging wave amplitude (approximately 0.5 kbar) is such that the tuff experiences significant nonlinear deformation. Also, both composite structures respond in the nonlinear regime.

The highly nonlinear nature of this problem requires the use of numerical simulation techniques. The SWIS finite element code (Frazier and Petersen, 1974; Sweet, et al., 1976), was utilized because of its ability to treat both the structure and the surrounding medium in the nonlinear response regime. This code is described in detail in Appendix A. Material models utilized for this study include the Soil Cap Model (DiMaggio and Sandler, 1971) for the NTS tuff, a variable modulus model for the reinforced concrete (Nelson, et al., 1971), a von Mises plasticity model for the steel liner and a P-α crush-up model (Herrmann, 1969; Carroll and Holt, 1972; Good, 1972; Riney, et al., 1972) for the cellular concrete.

The structural configurations considered in this study are meant to simulate experiments fielded in an underground explosion environment. They represent three different design philosophies; the unlined cavity utilizes the inherent strength of the medium, the reinforced concrete structure strengthens the cavity, and the cellular concrete decouples the liner behavior from that of the surrounding medium. The following sections discuss the results of the SWIS simulations.

CHAPTER II

PROBLEM CONFIGURATION

The configurations analyzed in this study are the response of buried cylindrical structures subjected to an explosion-induced stress wave. Effects due to the earth's free surface are ignored. The structure is assumed to be far enough removed from the explosion so that a plane wave assumption is valid. Also, end effects of the cylinders are not treated and a plane strain cross-sectional configuration is utilized.

Various nomenclature, including the configuration of the structure and surrounding medium, are depicted in Figure 1. As can be seen, a plane of symmetry allows one-half of the problem to be considered. The plane wave is assumed to travel along the horizontal direction from the left towards the right of Figure 1.

A finite element simulation of the buried structures requires definitions of the finite element mesh, material models, and boundary conditions. The following subsections describe the information appropriate for the simulations of this study.

2.1 FINITE ELEMENT REPRESENTATION

The finite element representation of the dashed region of Figure 1 can be seen in Figure 2. The finite element mesh of the tuff medium as well as that of the two composite structures are depicted. For the unlined cavity, all elements surrounding the 5-foot-diameter cylindrical opening are quadrilateral. (This unlined cavity mesh is similar to the one appearing in Figure B.1.)

A study similar to that represented by Figure 1 has been completed for a linear structure-medium configuration (Sweet, 1976B). A finite element mesh identical to that of

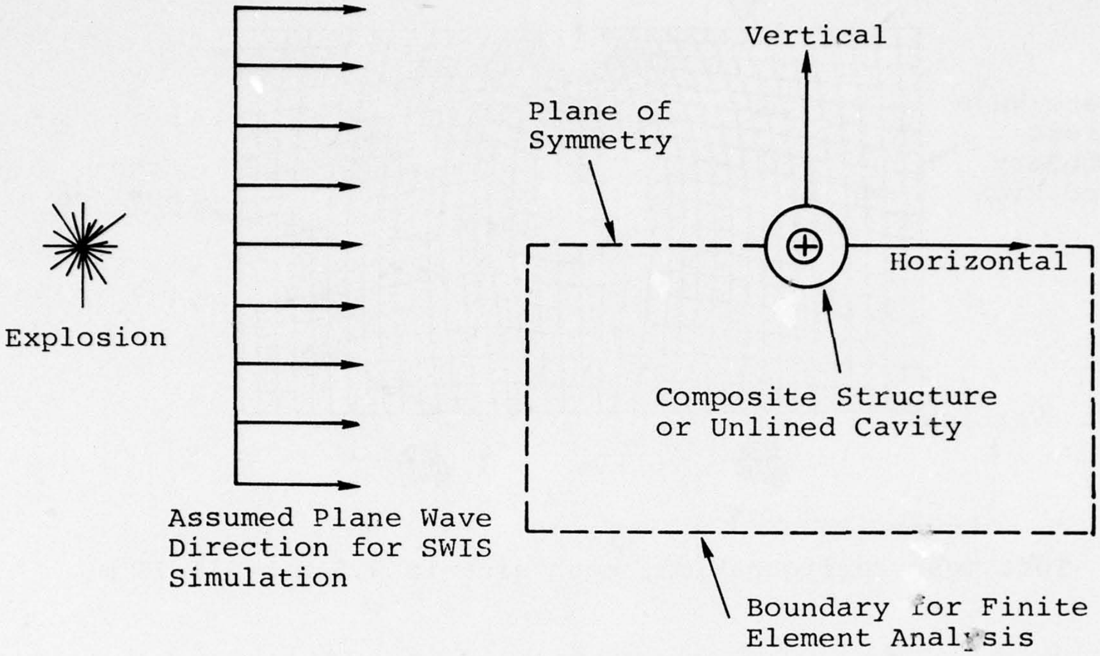

(a) Structure configuration and finite element grid location.

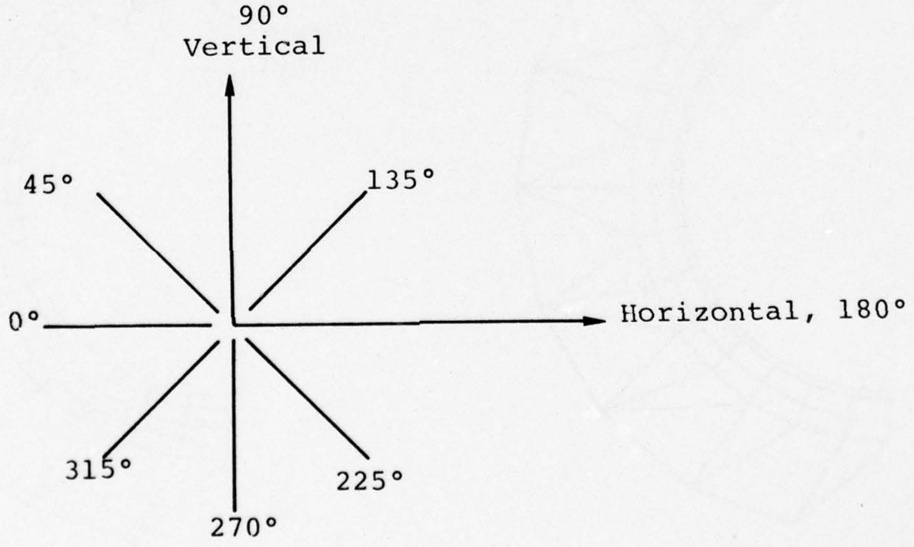

(b) Angular definitions.

Figure 1. Nomenclature and configuration of the unlined cavity and composite structures.

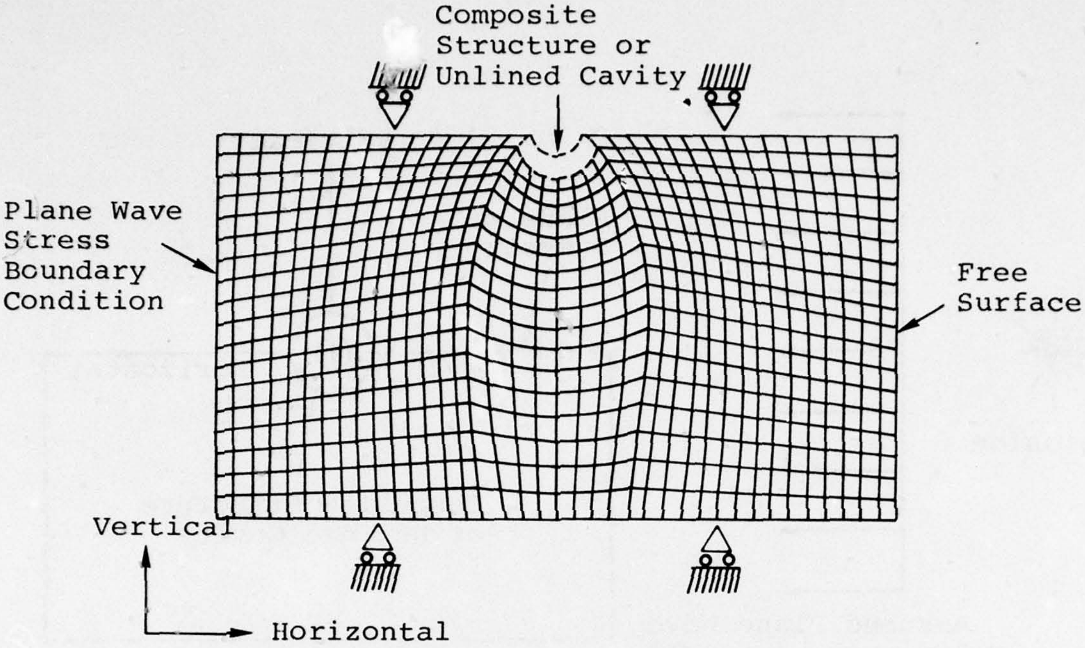

(a) Tuff mesh configuration, mesh size is 9.5 m by 16.75 m.

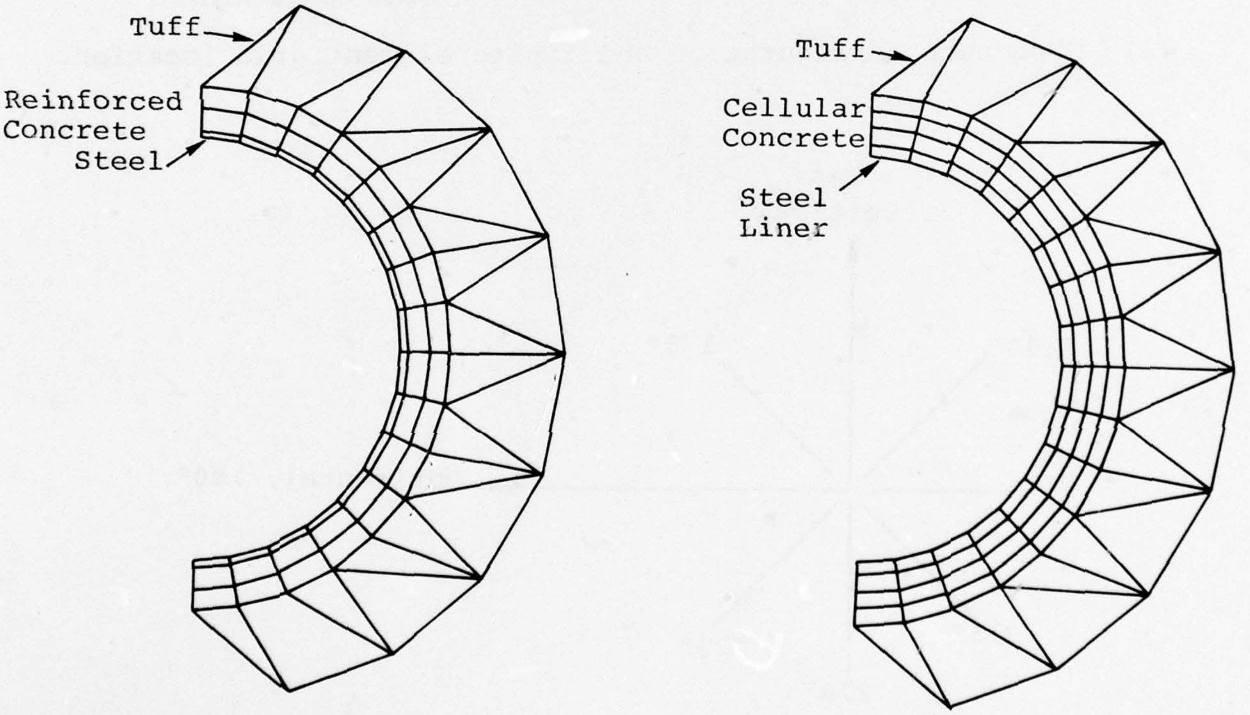

(b) Reinforced concrete detail, inner diameter is 4 feet and thickness of steel and concrete are 3/4 inches and 5 inches, respectively.

(c) Cellular concrete detail, inner diameter is 4 feet and thickness of steel and concrete are 1.5 inches and 6 inches, respectively.

Figure 2. Finite element mesh for both tuff and composite structures.

Figure 2 was utilized for this calculation. The excellent correlation with the theoretical solution obtained for this study serves as a validation of the capability of SWIS for treating structure-medium interaction problems of this type. This linear solution is also summarized in Appendix A.

2.2 NTS TUFF MATERIAL BEHAVIOR

The material model used for the NTS tuff is the Soil Cap Model (DiMaggio and Sandler, 1971). A detailed description of this constitutive model can be found in Appendix A. The highly nonlinear nature of this model allows the observed compaction behavior of this soil-like medium to be simulated. The material parameters used in this model are given below (Baron, 1975; Sandler, 1975A; Sandler, 1975B):

$A = 0.5$ kbar

$B = 0.52$ kbar^{-1}

$C = 0.44$ kbar

$D = 1.8$ kbar^{-1}

$R = 3.0$

$W = 0.015$

$X_o = 0.003$ kbar.

In addition, the tuff has an initial density of 2.0 gm/cm^3 and elastic bulk and shear moduli of 100 kbars and 38 kbars, respectively. The tensile strength of the material is assumed to be zero. The procedure used in SWIS is to test the principal stresses for tensile failure before the cap model is utilized. The state of stress is first assumed to be elastic. If any principal stress is tensile it is set to zero. The resulting state of stress is then modified by the cap model if necessary. This method is superior to the technique of using J_1 ($\equiv \sigma_{kk}$)

as the criterion for tensile failure since J_1 can be compressive and yet an individual principal stress can be tensile.

The uniaxial strain behavior of this material utilizing the above parametric values is depicted in Figure 3. Also appearing in this figure is a comparison with the uniaxial strain behavior for the material properties of Baron, 1975. The stress-strain behaviors for hydrostatic and triaxial states of stress show similar correlations with their corresponding results of this reference.

In the actual buried structural configuration, of course, the medium is subjected to in situ tectonic and gravitational stresses. A dynamic calculation with a static prestressed gravitational load and a stress-free unlined cavity is described in Appendix B. The inclusion of the in situ stresses affected the calculated maximum cavity closure by approximately 15 percent for this configuration. Since this difference is small compared to the unknowns involved in nonlinear constitutive modeling and since the actual in situ stress level is unknown, the in situ stresses are ignored in the results reported in this study.

2.3 CELLULAR CONCRETE

The cellular concrete composite structure analyzed in this study (designed by Lindberg, 1975) requires a cellular concrete with a 1500 psi (0.1034 kbar) crush strength. The actual field test environment is the dynamic loading of a cellular concrete with approximately 250-day strength properties. Existing laboratory material properties data consist of static, 28-day values. It has been previously noted that the behavior of cellular materials is highly strain-rate dependent (Butcher, 1971; Hoff, 1975). It is also true, as with other concrete materials, that the behavior of cellular concrete depends upon its age. Due to a lack of extensive strain-rate data, a

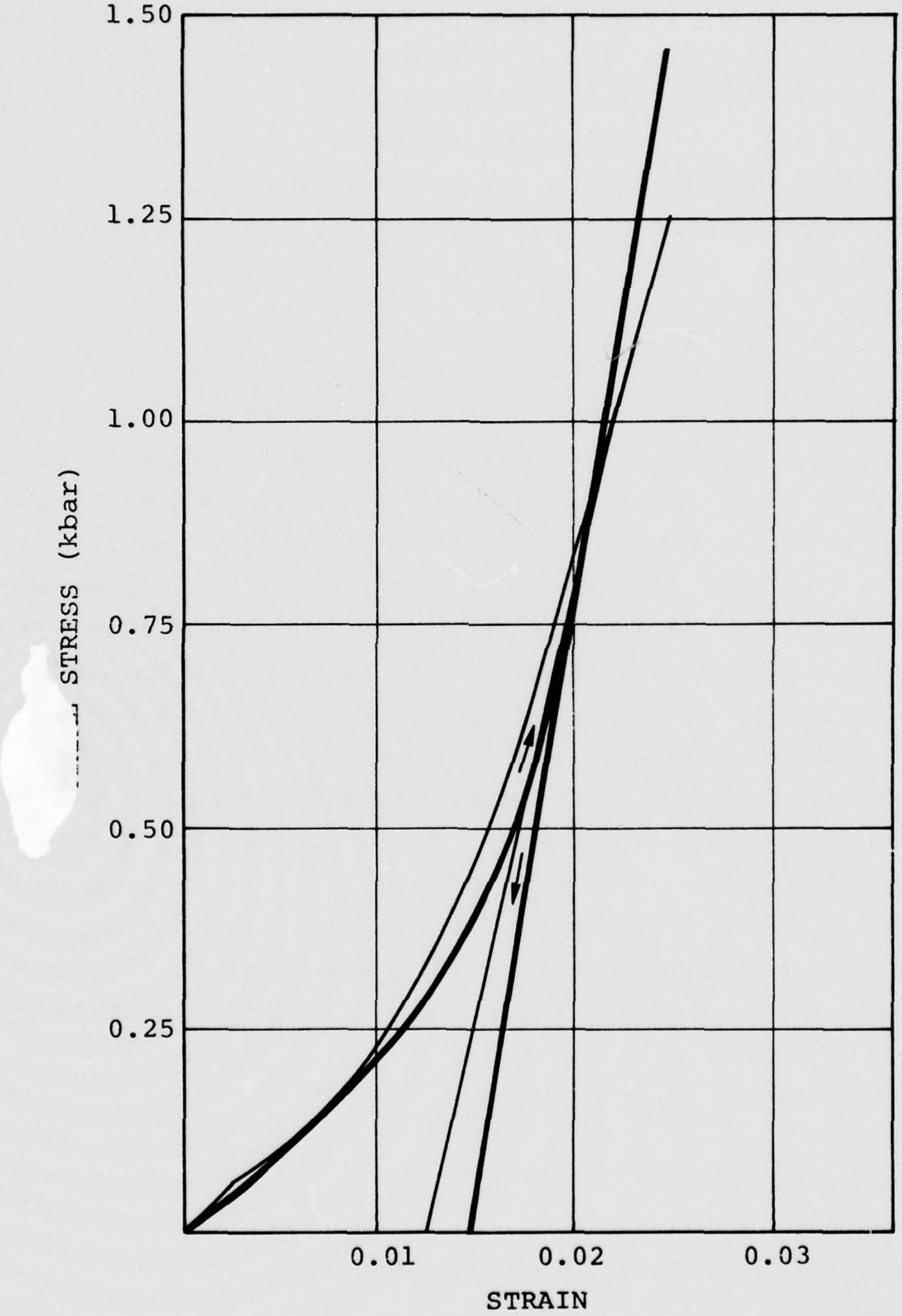

Figure 3. Uniaxial strain behavior of NTS tuff used in calculations (bold line). Behavior of Baron (1975) (light line) is also given.

rate-dependent model such as that given by Butcher (1971) cannot be formulated. Rate-independent properties appropriate for the expected strain rate will be utilized instead. Using Equations (8) and (9) as given by Hoff (1975), yields a static, 28-day strength of 900 psi (0.062 kbar) if a dynamic, 250-day strength of 1500 psi is desired. The P-α crush-up model described in Appendix A will be used to represent the irreversible crush-up behavior.

It will be assumed that the "strength" refers to the value obtained in a uniaxial strain environment. Using available experimental data (Hoff, 1971; Hoff, 1972; Hoff, 1975), the stress-volumetric strain response up to a maximum strain of 0.47 is given in Figure 4. These data are the result of punch tests and thus are not exactly uniaxial strain; however, the differences will be ignored. The P-α model requires P(v) data where P is the pressure and v is the *specific volume.* Uniaxial strain data may be used to derive P(v) if the shear behavior of the porous material is known. It will be assumed that the deviatoric stress behavior of the cellular concrete is described by a simple von Mises yield stress, Y_o, and the associated flow rule. The shear modulus, μ_o, is assumed to be constant. Thus, for a uniaxial strain environment ($\varepsilon_1 \neq 0$) with principal stresses (positive in comparison) $\sigma_1 > \sigma_2 = \sigma_3$, the linear and plastic deviatoric stress behavior is given by

(A) linear: $\sigma_1 - \sigma_2 = 2\mu_o\varepsilon_1$ (1a)

(b) plastic: $\sigma_1 - \sigma_2 = Y_o$. (1b)

In either case the pressure is defined as

$$P = \frac{\sigma_1 + 2\sigma_2}{3} \quad . \tag{2}$$

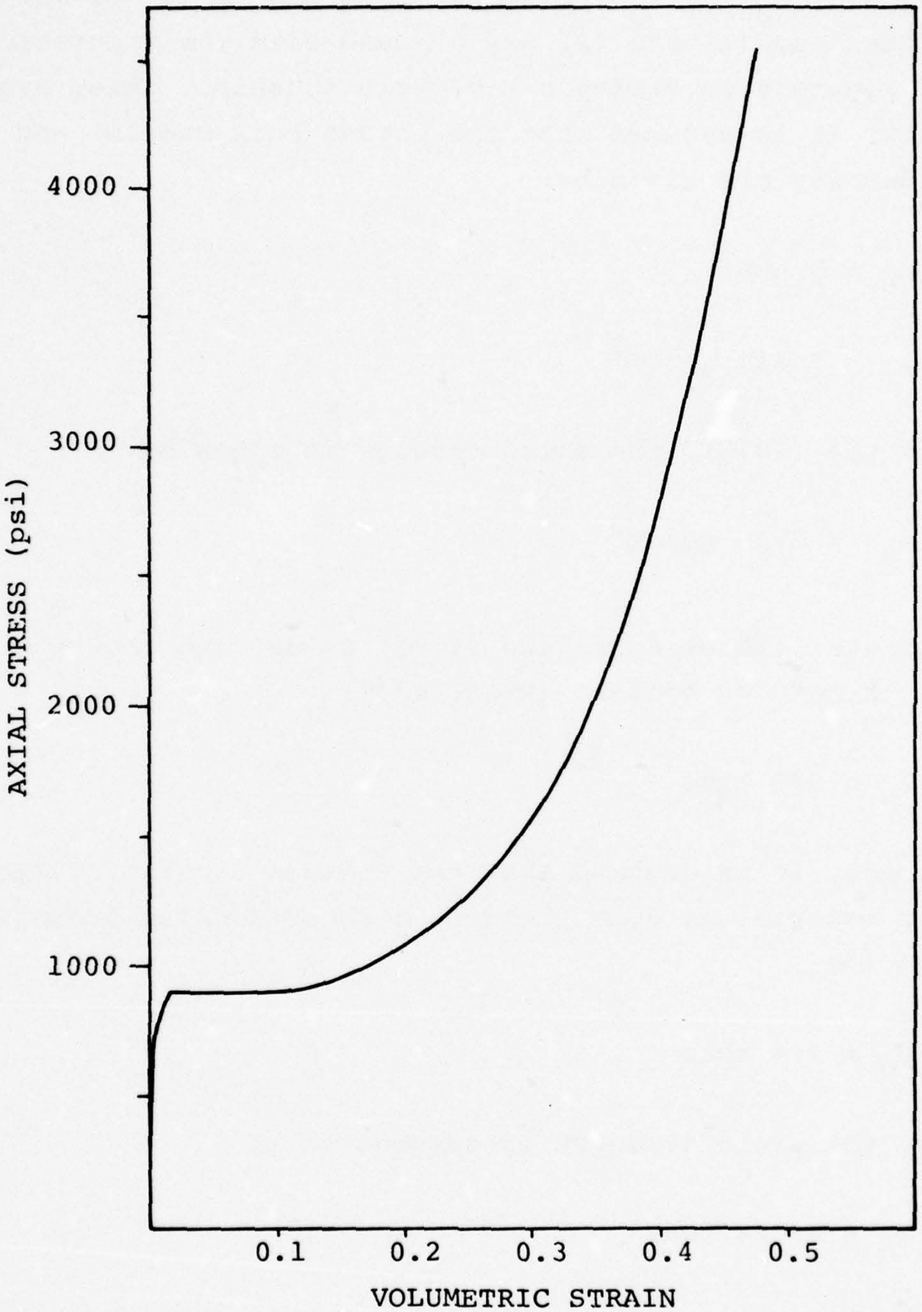

Figure 4. Stress-strain curve for cellular concrete with a 28-day strength of 900 psi.

Assuming that μ_o and Y_o are known, Equation (A-10) of Appendix A and Equations (1) and (2) may be used with the experimental data of Figure 4 to derive a P(v) relationship. Using available data, it is assumed that the porous bulk modulus and the porous density are given by:

$$\begin{gathered} K_o = 9 \text{ kbar} \\ \rho_o = 0.854 \text{ gm/cm} \end{gathered} \tag{3a}$$

and from Lee (1973), the solid density is given by:

$$\rho_{s_o} = 2.25 \text{ gm/cm}^3 \quad . \tag{3b}$$

For concrete without aggregate it may be assumed that the solid bulk modulus becomes (Read, 1971):

$$K_s = 200 \text{ kbar} \quad . \tag{3c}$$

Furthermore, it is assumed that the Poisson's ratio of the cellular material is 0.38 yielding a shear modulus (using Equation (3a)

$$\mu_o = 2.4 \text{ kbar} \quad . \tag{3d}$$

Finally, the yield strength is assumed to be

$$Y_o = 0.024 \text{ kbar} \quad . \tag{3e}$$

The data of Equation (3) along with Figure 4 are sufficient to prescribe the 28-day behavior of the cellular concrete up to a maximum stress, σ_1, of 4500 psi (0.31 kbar). For consistency, a crush pressure of 0.88 kbar is assumed. Using the P-α expressions, data of Figure 4, data of Equation (3), and assuming $P_c = 0.88$ kbar, the resulting P(v) behavior appears in Figure 5. Since it is well-known that strength and modulus of concrete increase at approximately the same ratio, the 250-day, dynamic values are determined by scaling the 28-day properties by the stress ratio $1500/900 \equiv 5/3$. This P(v) curve also is given in Figure 5. The resulting $\alpha(P)$ relationship is given in Figure 6.

The effect of water saturation on the behavior of porous materials is extremely important (Riney, et al., 1972). It can be expected that the material behavior of Figures 5 and 6 would be significantly altered if the cellular concrete were saturated.

2.4 REINFORCED CONCRETE MATERIAL BEHAVIOR

The reinforced concrete material behavior is modeled using a variable modulus model, (Nelson, et al., 1971). Its formulation is described in Appendix A. Parametric values for the material constants are given by:

$$\left.\begin{array}{l} K_o = 195 \text{ kbar} \\ K_1 = -388\ K_o \\ K_2 = -100\ K_1 \end{array}\right\} \quad \text{hydrostatic material properties}$$

$$\left.\begin{array}{l} G_o = 147 \text{ kbar} \\ \gamma_1 = 797 \\ \bar{\gamma}_1 = -920 \end{array}\right\} \quad \text{shear material parameters}$$

In addition, its initial density is 2.415 gm/cm^3. The above properties result in an 8000 psi compressive strength. This strength has been increased from the 28-day static value of 5500 psi to account for dynamic and aging effects.

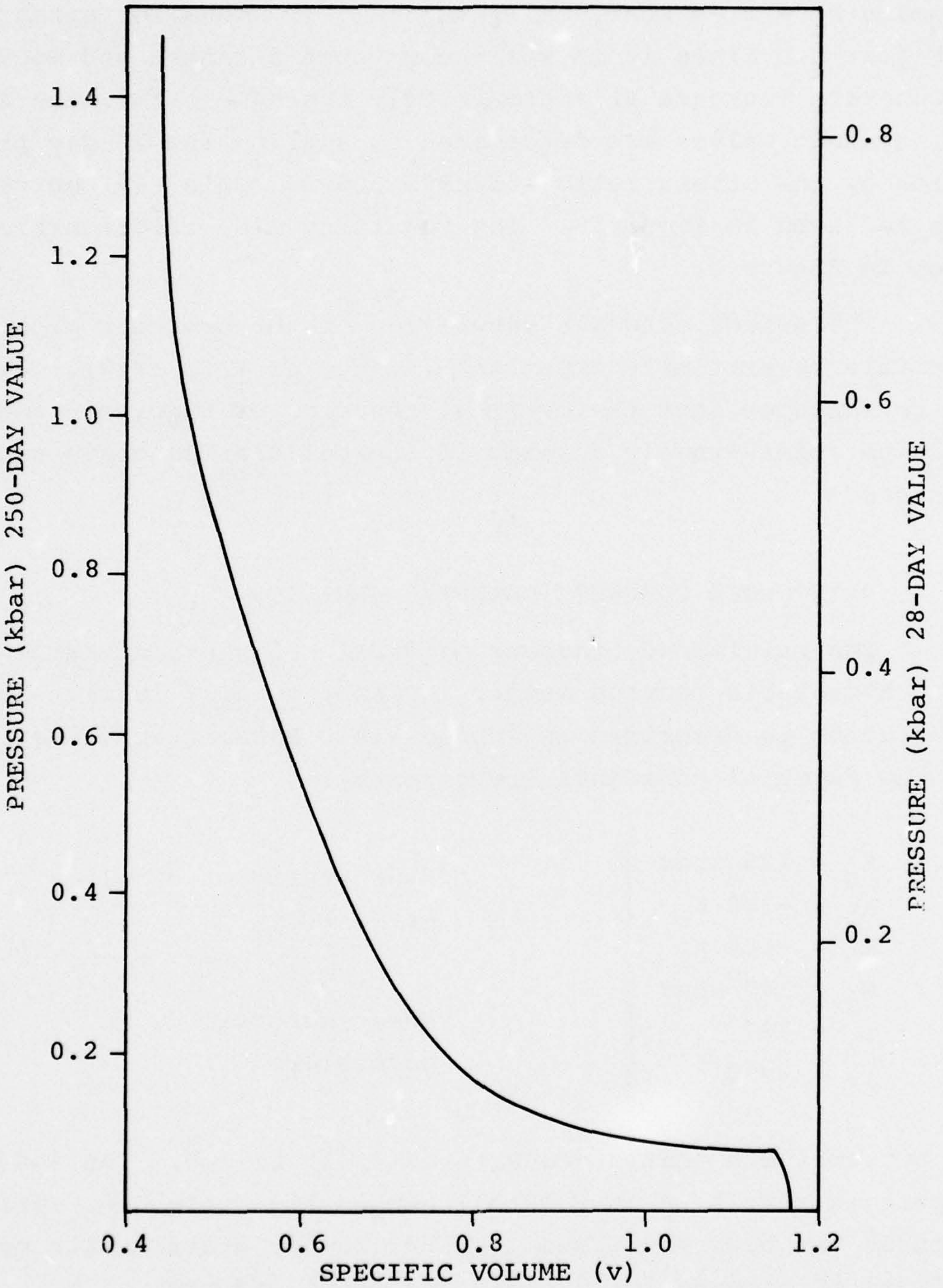

Figure 5. P(v) relationship for 28-day (static) and 250-day (dynamic) cellular concrete.

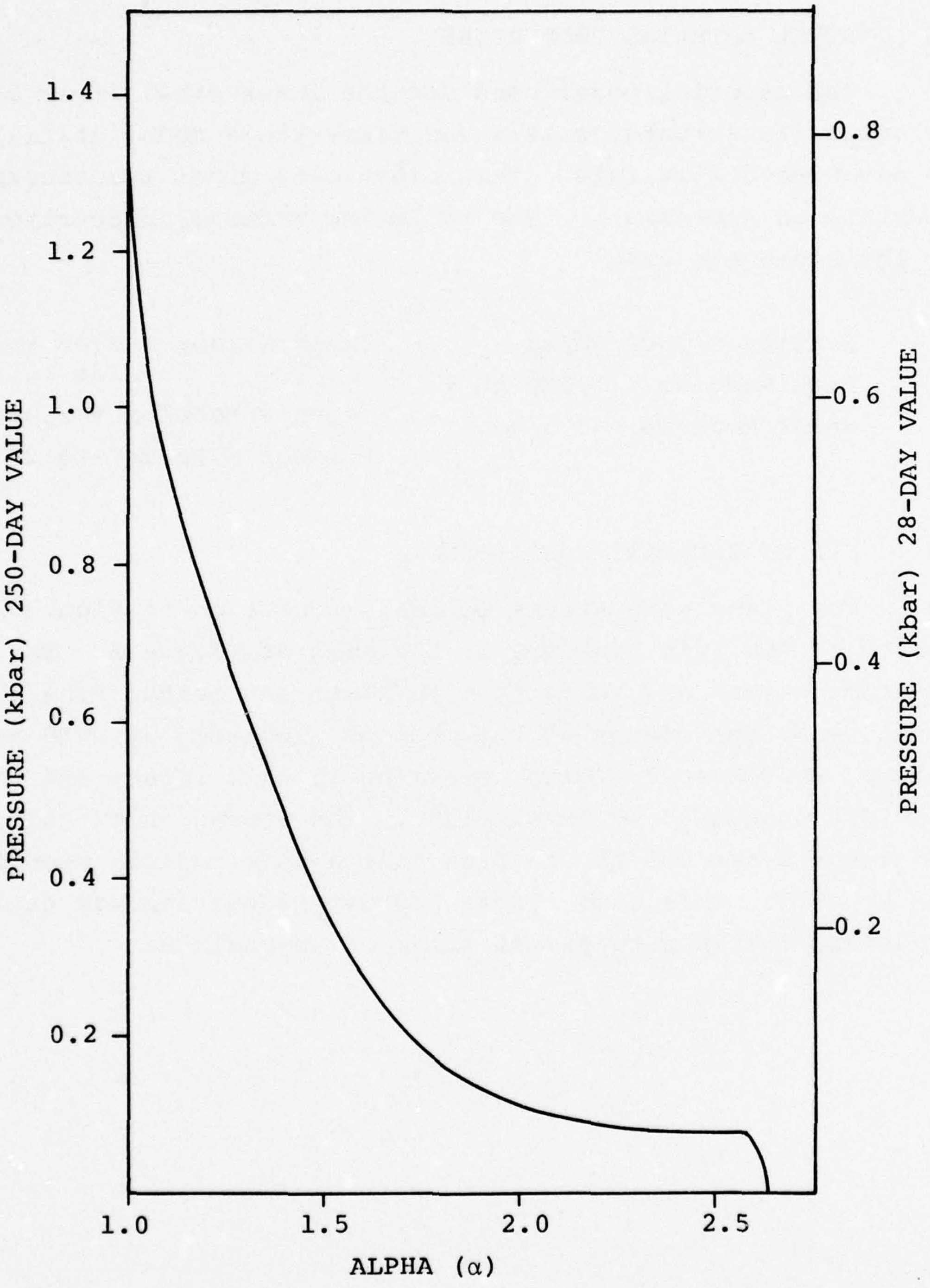

Figure 6. α(P) relationship for 28-day (static) and 250-day (dynamic) cellular concrete.

2.5 STEEL MATERIAL PROPERTIES

The material model used for the inner steel liner of the composite structures is a von Mises yield model utilizing the associated flow rule. This plasticity model is described in detail in Appendix A. The following material properties for the steel are used:

Density = 7.84 gm/cm
Bulk Modulus = 1,590 kbar
Shear Modulus = 775 kbar

Yield Stress = 2.48 kbar (36 ksi)
Young's Modulus = 2,000 kbar
Poisson's Ratio = 0.29

2.6 STRESS BOUNDARY CONDITION

The plane wave stress boundary condition of Figure 1 is applied at the left boundary of the mesh of Figure 2. The resulting stress and velocity time histories across from the structure at the bottom of the mesh as predicted by SWIS are depicted in Figure 7. Also appearing in this figure are the behaviors suggested by Baron, 1975. The steepness of the SWIS results are due to the fact that a more refined mesh was used by SWIS. This same stress boundary condition was used to perform the _in situ_ stress study of Appendix B.

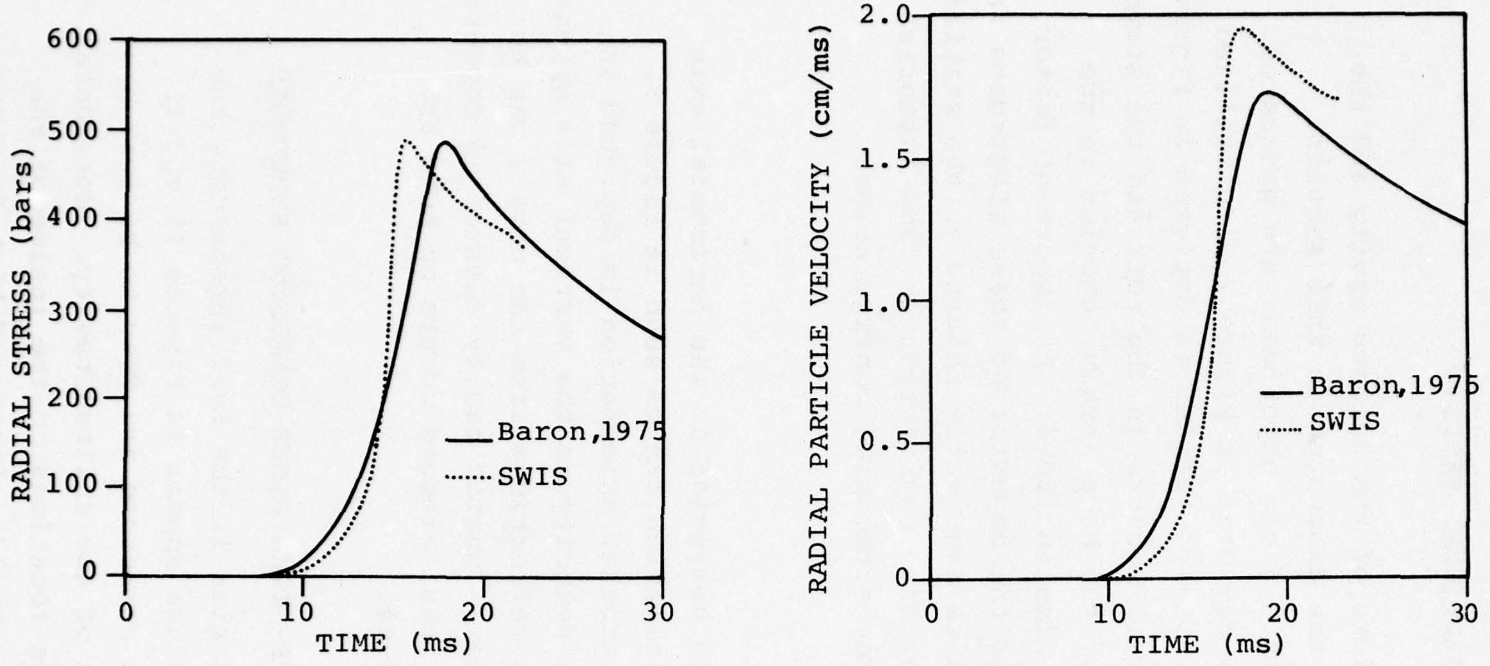

(a) Comparison of SWIS and Weidlinger stress waveforms at structure ℄; reinforced concrete-steel cylinder.

(b) Comparison of SWIS and Weidlinger velocity waveforms at structure ℄; reinforced concrete-steel cylinder.

Figure 7. Free-field stress and velocity transients at structure horizontal distance.

CHAPTER III
CALCULATIONAL RESULTS

The dynamic behaviors of the unlined cavity and the two composite structures are discussed in this section. Data typically measured in a field experiment are presented. The finite element meshes depicted in Figure 2 were utilized and the impinging plane wave description is depicted in Figure 7. Velocity histories at several points in the tuff and the structure are presented. Also, the hoop strain behavior in the composite structures are also included. An important factor that can be used to assess the behavior of these structures is the cavity closure, which is inherently related to the stability of these underground openings. Cavity closure time histories are presented for the three structural configurations.

3.1 UNLINED CAVITY

Three velocity time histories on the horizontal axis of the unlined cavity calculation can be seen in Figure 8. The nomenclature for the angular orientation is depicted in Figure 1. The horizontal velocity on the vertical axis appears in Figure 9. The obvious reflections from the cavity can be seen in both these figures. Dynamic cavity closure is depicted in Figure 10. As can be seen, closure occurs on both the horizontal and vertical axes.

3.2 REINFORCED CONCRETE-STEEL LINER COMPOSITE STRUCTURE

Velocity time histories in the tuff surrounding the reinforced concrete structure appear in Figures 11 and 12. The reflections from this structure are seen to be less pronounced compared to those of the unlined cavity. Horizontal velocity behavior at three locations on the inside of the steel liner appears in Figure 13. Increased high frequency

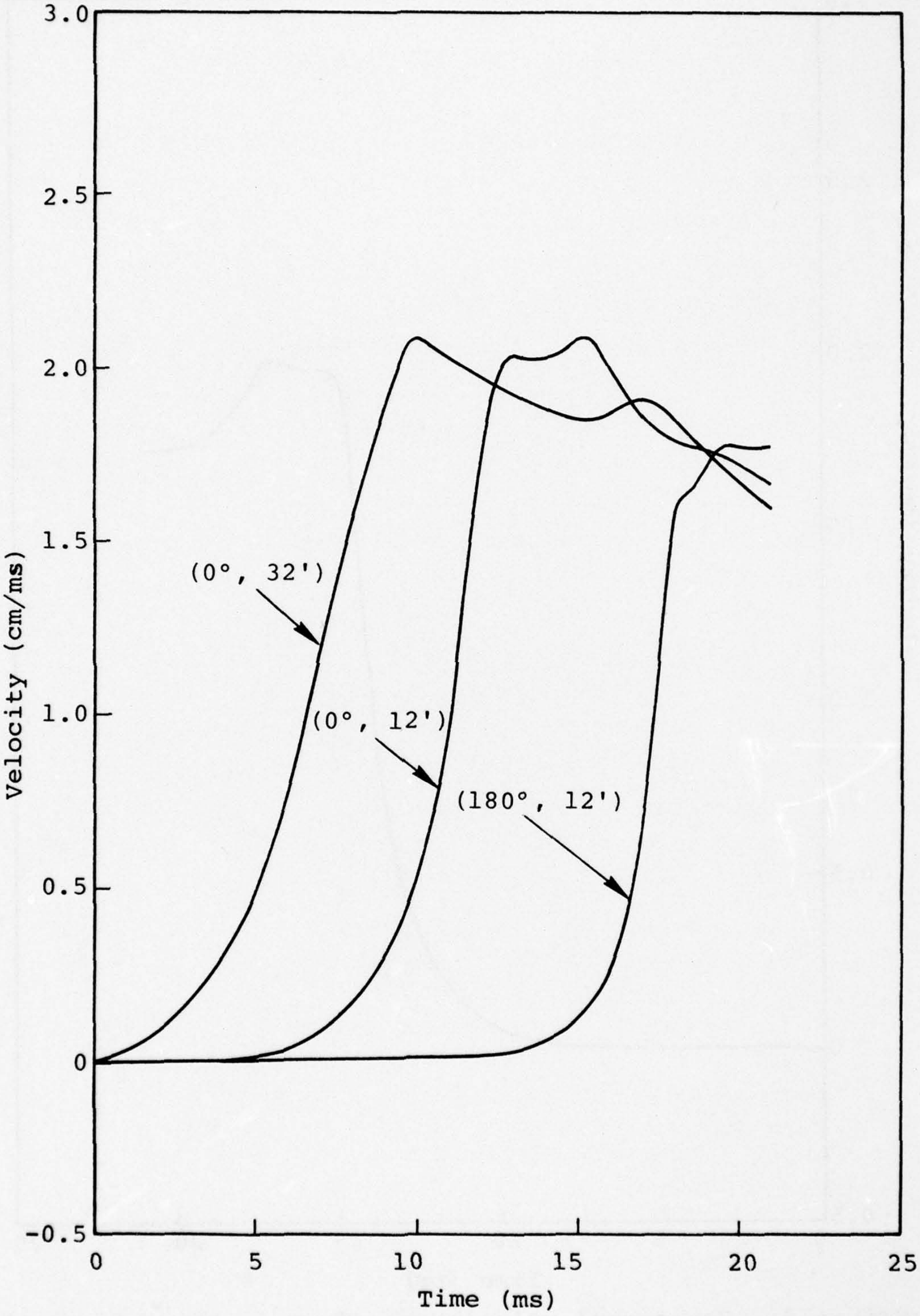

Figure 8. Horizontal velocity waveforms in the tuff on the horizontal axis, approximately 32 feet, and 12 feet in front of, and 12 feet in back of the unlined cavity.

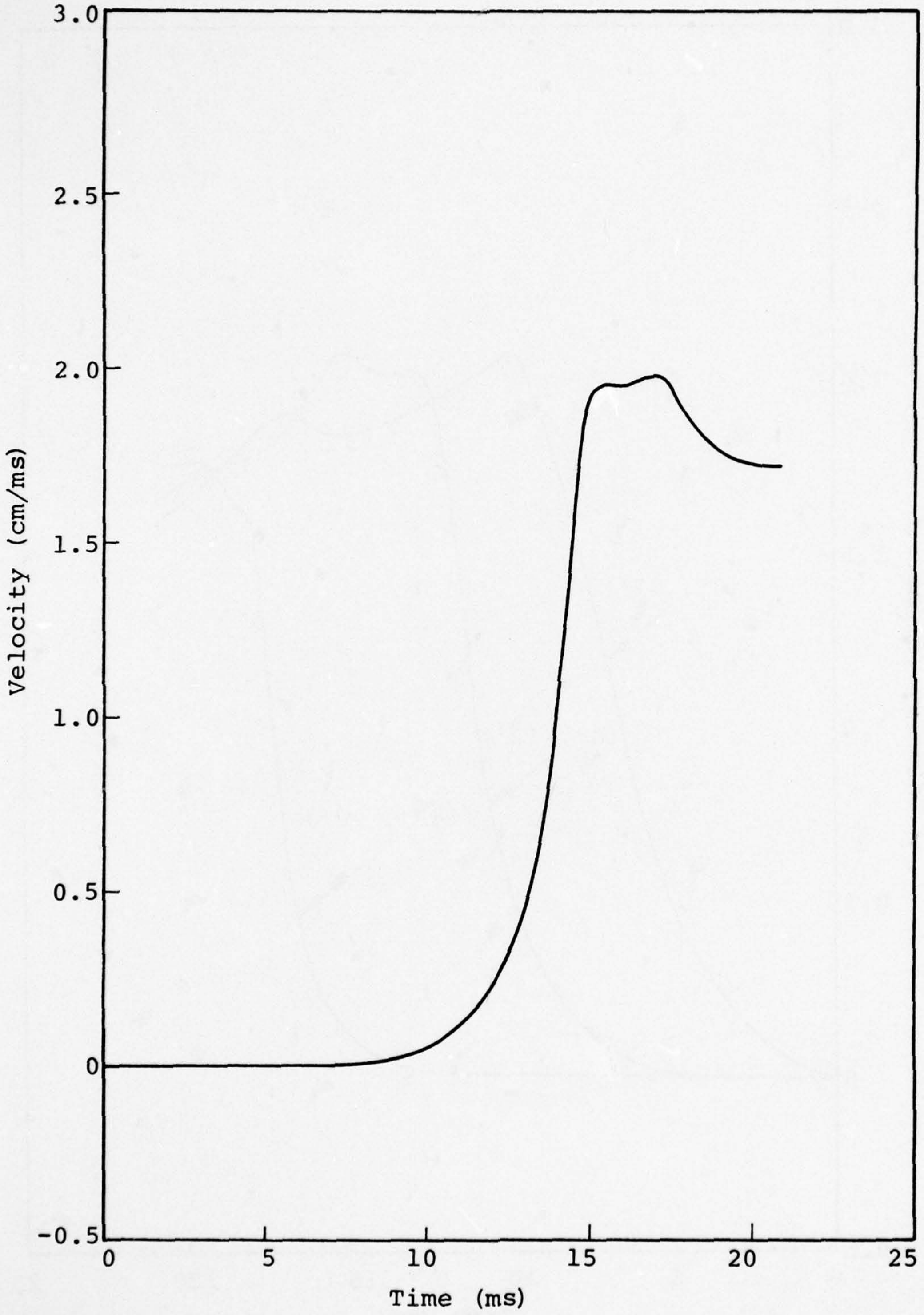

Figure 9. Horizontal velocity waveform in the tuff on the vertical axis, approximately 12 feet from the unlined cavity (i.e., 90° or 270°, 12').

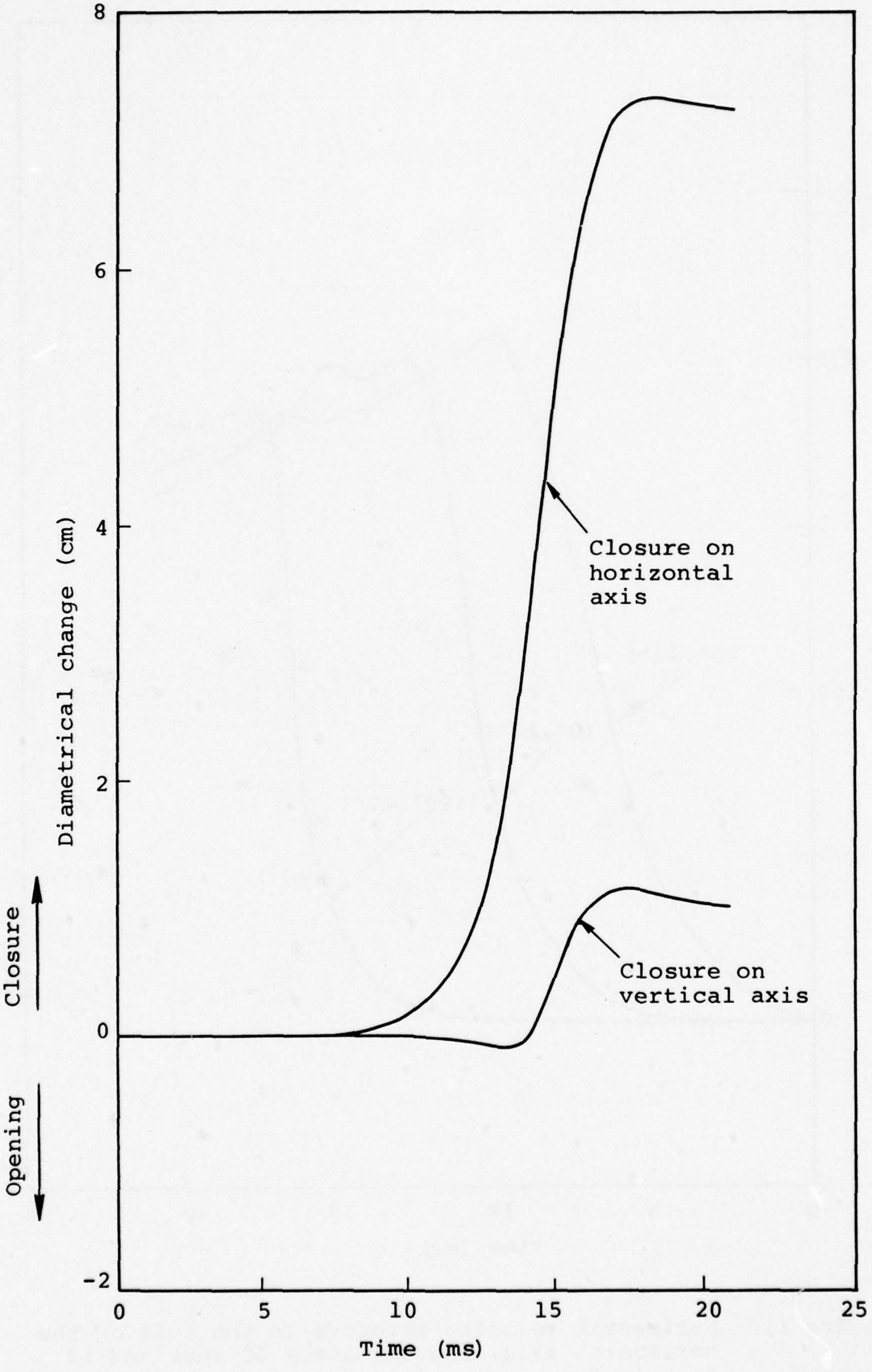

Figure 10. Diametrical behavior of the unlined cavity.

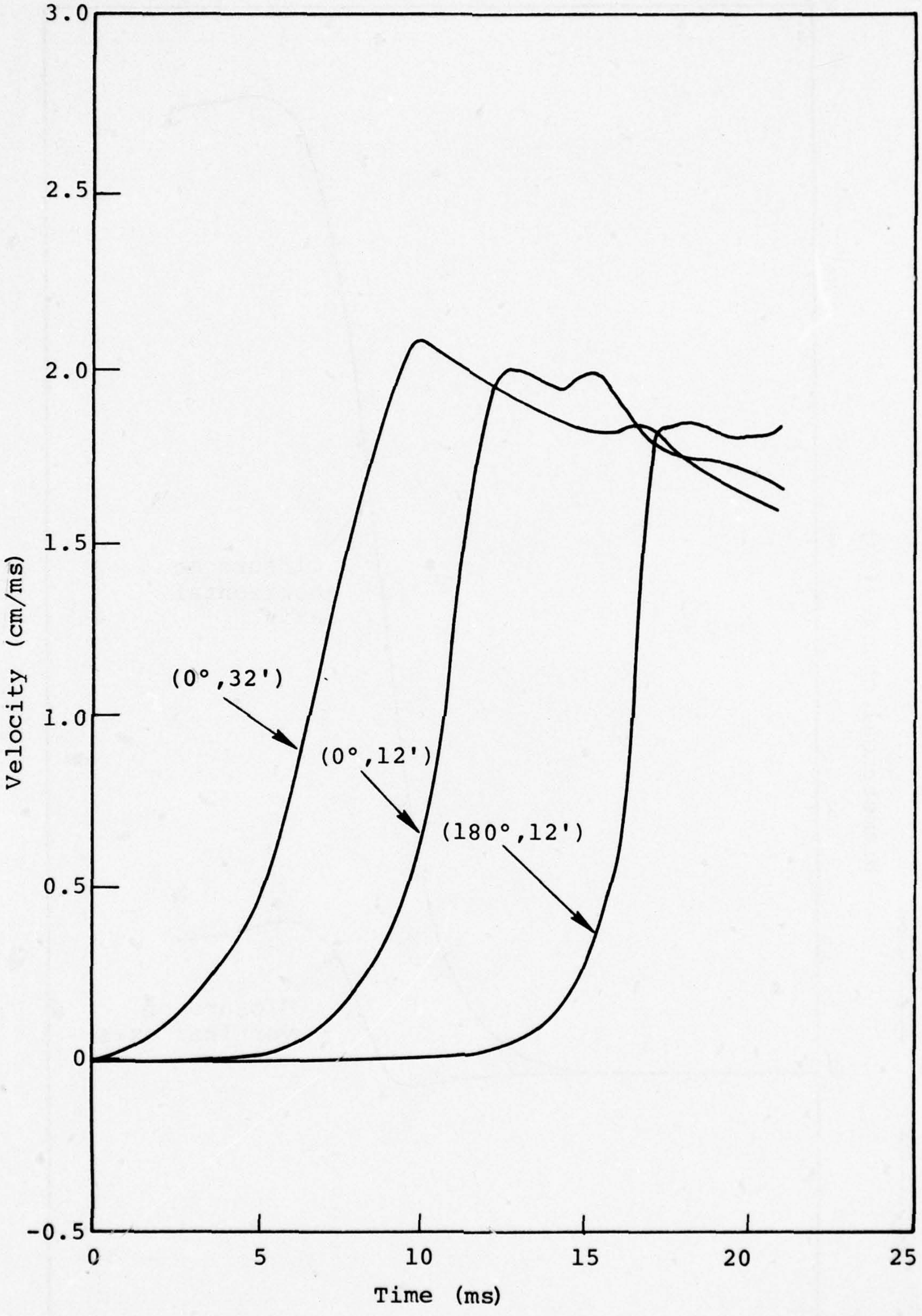

Figure 11. Horizontal velocity waveform in the tuff on the horizontal axis, approximately 32 feet and 12 feet in front of, and 12 feet in back of the reinforced concrete structure.

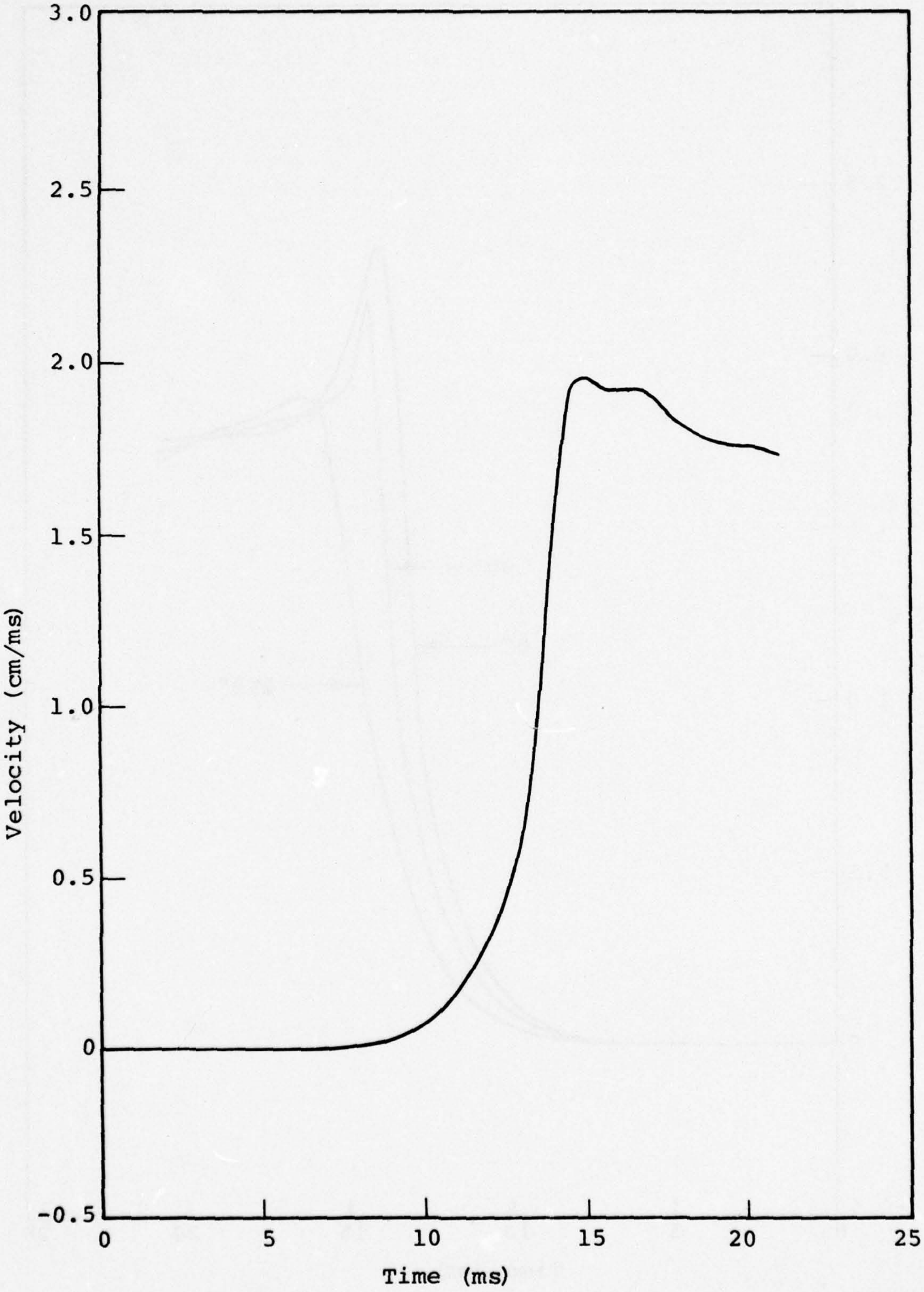

Figure 12. Horizontal velocity waveform in the tuff on the vertical axis, approximately 12 feet from the reinforced concrete structure (i.e., 90° or 270°, 12').

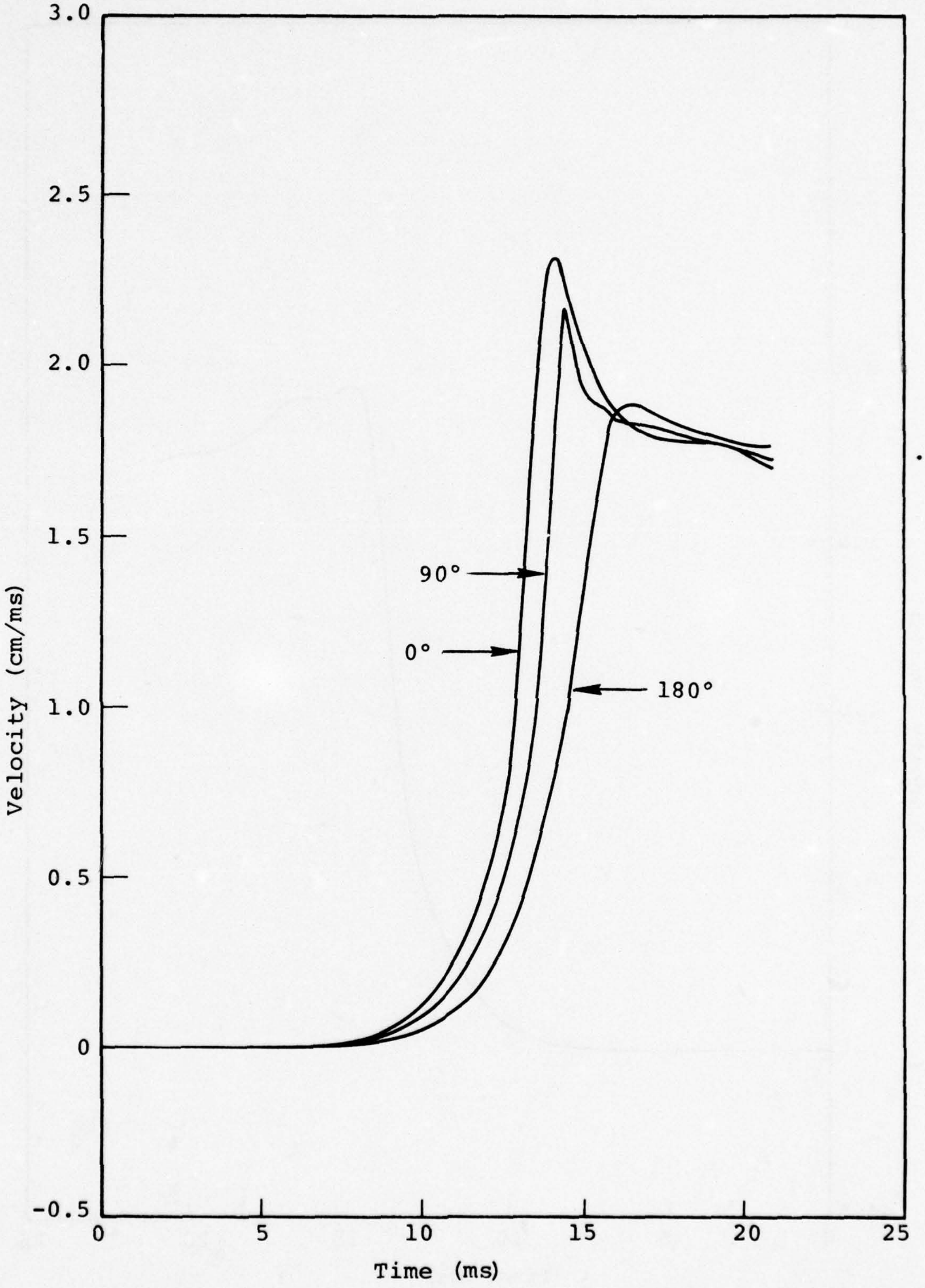

Figure 13. Velocity waveforms at the inner surface of the steel liner of the reinforced concrete structure at the 0°, 90° (or 270°) and 180° locations.

content is noticeable for the steel behavior compared to the free-field input.

The 0.5 kbar stress wave results in nonlinear behavior in both the reinforced concrete and steel liner, as well as the surrounding tuff. Hoop strain in the structural components resulting from the impinging plane is depicted in Figures 14 and 15. As can be seen, the focusing of energy around the structure is particularly apparent in the steel liner. The cavity closure appearing in Figure 16 exhibits closure on the horizontal axis and opening on the vertical axis.

3.3 CELLULAR CONCRETE-STEEL LINER COMPOSITE STRUCTURE

Because of the low compression strength of the cellular concrete, the velocity behavior in the tuff surrounding this structure, which appears in Figures 17 and 18, is quite similar to the unlined cavity results of Figures 8 and 9. Also, the reduced strength of the concrete has modified the steel liner velocity histories, presented in Figure 19, compared to those of the reinforced structure, Figure 13.

Strains in the cellular concrete and steel liner are given in Figures 20 and 21. Comparing Figures 15 and 21, quite dissimilar behavior in the steel liner is noted for the two composite structures. The cavity closure depicted in Figure 22 is similar to the reinforced structure in that closure on the horizontal axis and opening on the vertical axis occurs.

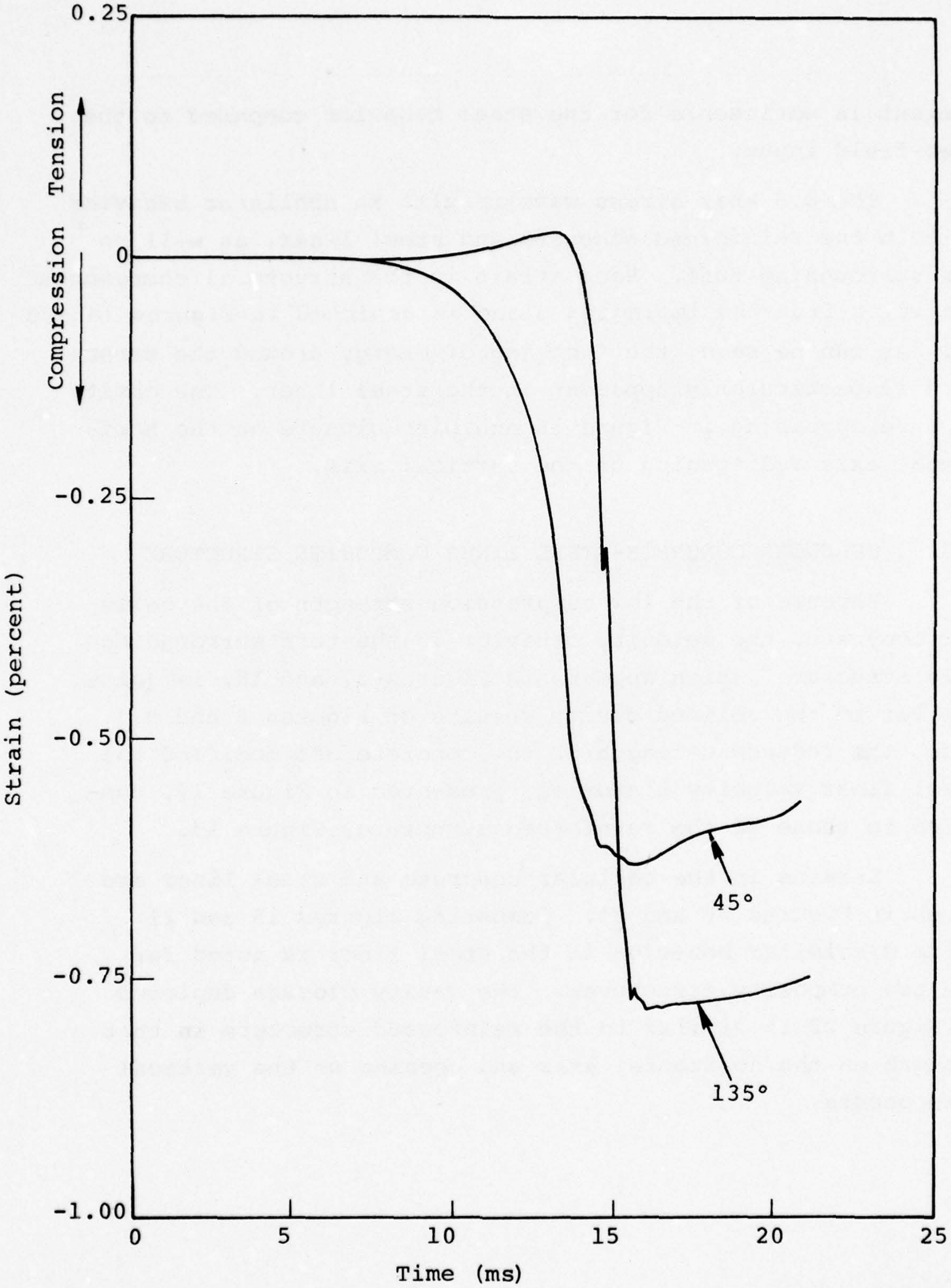

Figure 14. Hoop strain waveforms in the center of the reinforced concrete at the 45° (or 315°) and 135° (or 225°) locations.

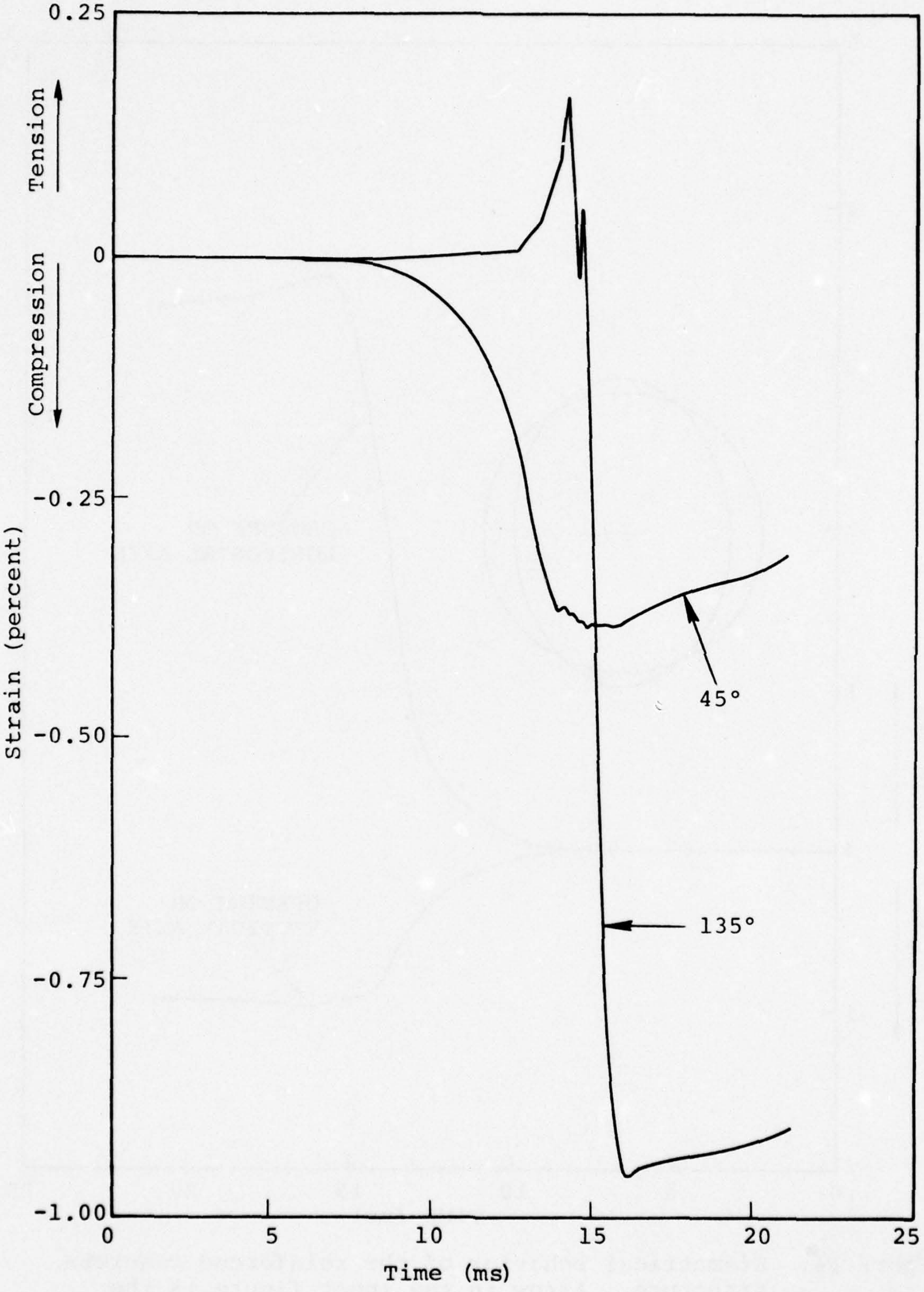

Figure 15. Hoop strain waveforms at the steel inner surface of the reinforced concrete structure at the 45° (or 315°) and 135° (or 225°) locations.

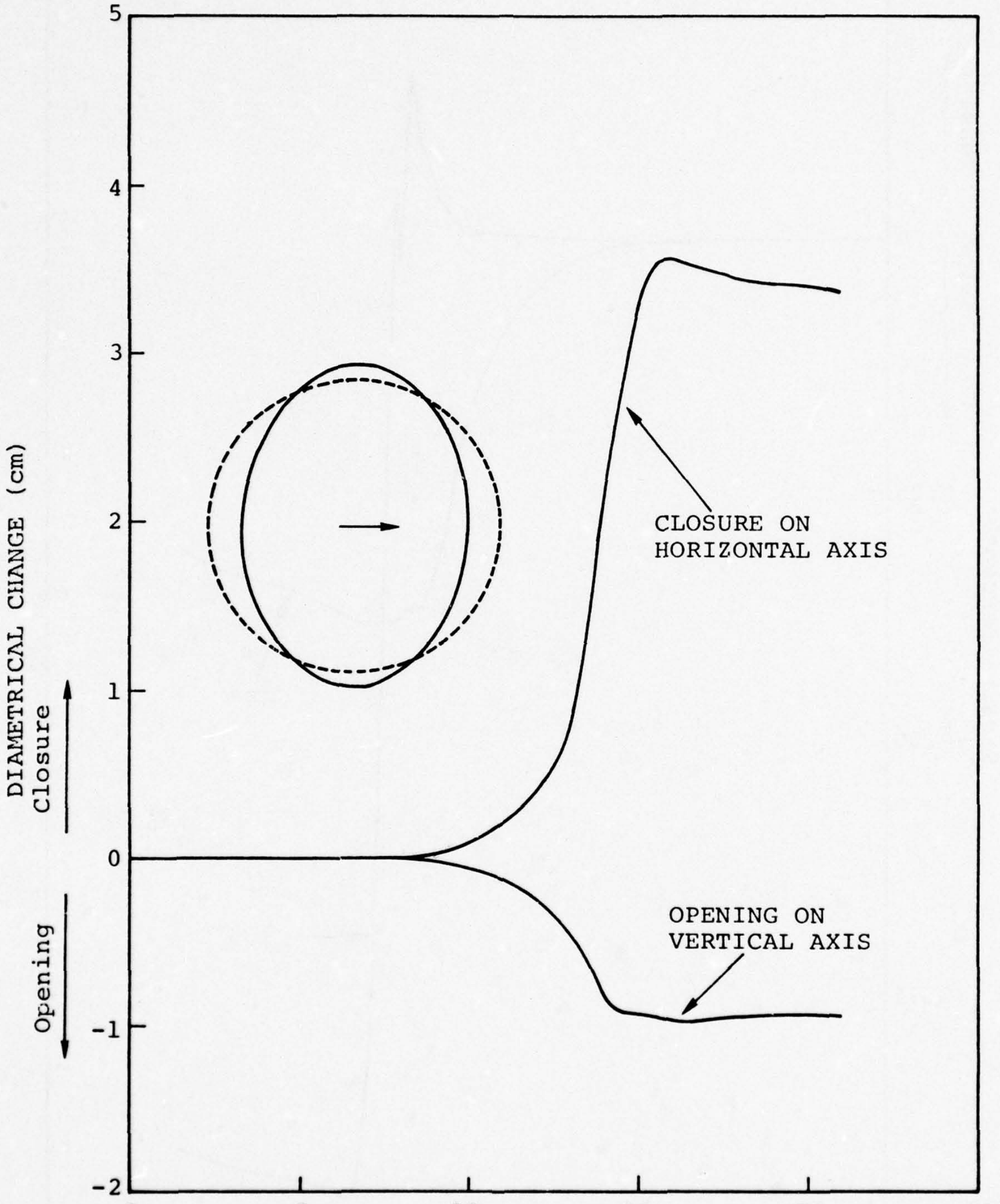

Figure 16. Diametrical behavior of the reinforced concrete structure. Arrow in the inset figure is the direction of the plane wave and lies along the horizontal axis.

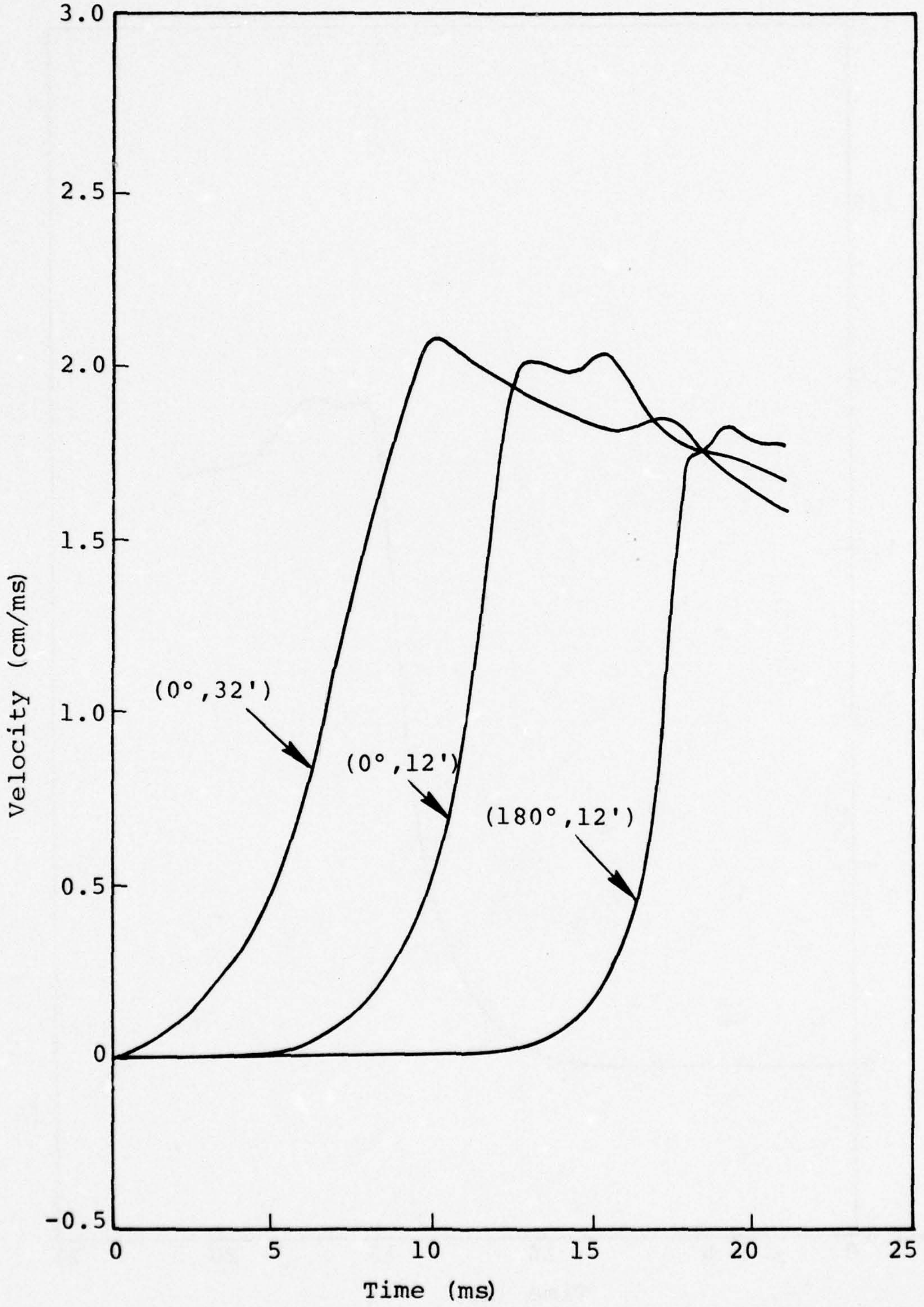

Figure 17. Horizontal velocity waveforms in the tuff on the horizontal axis, approximately 32 feet and 12 feet in front of, and 12 feet in back of the cellular concrete structure.

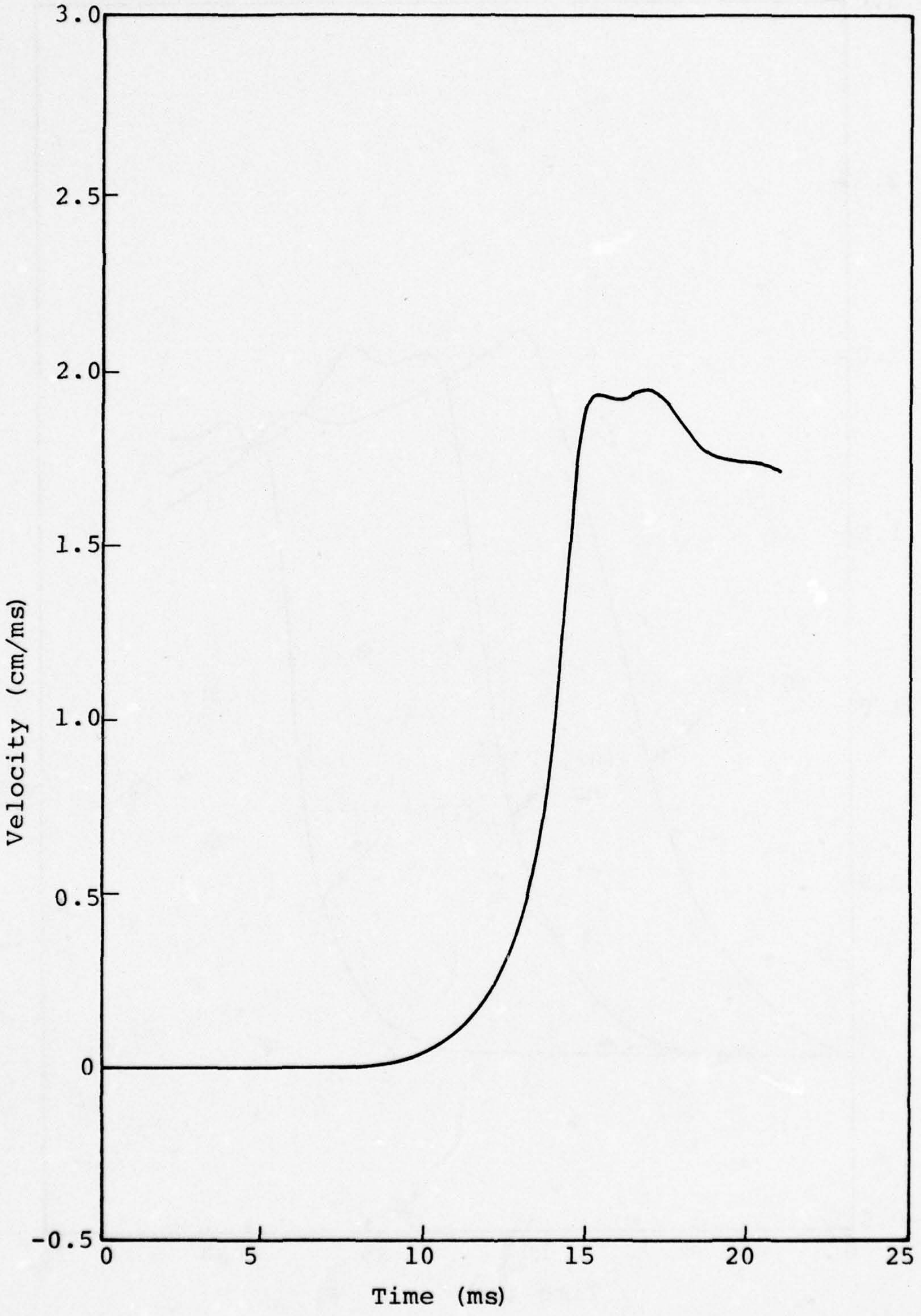

Figure 18. Horizontal velocity waveform in the tuff on the vertical axis, approximately 12 feet from the cellular concrete structure (i.e., 90° or 270°, 12').

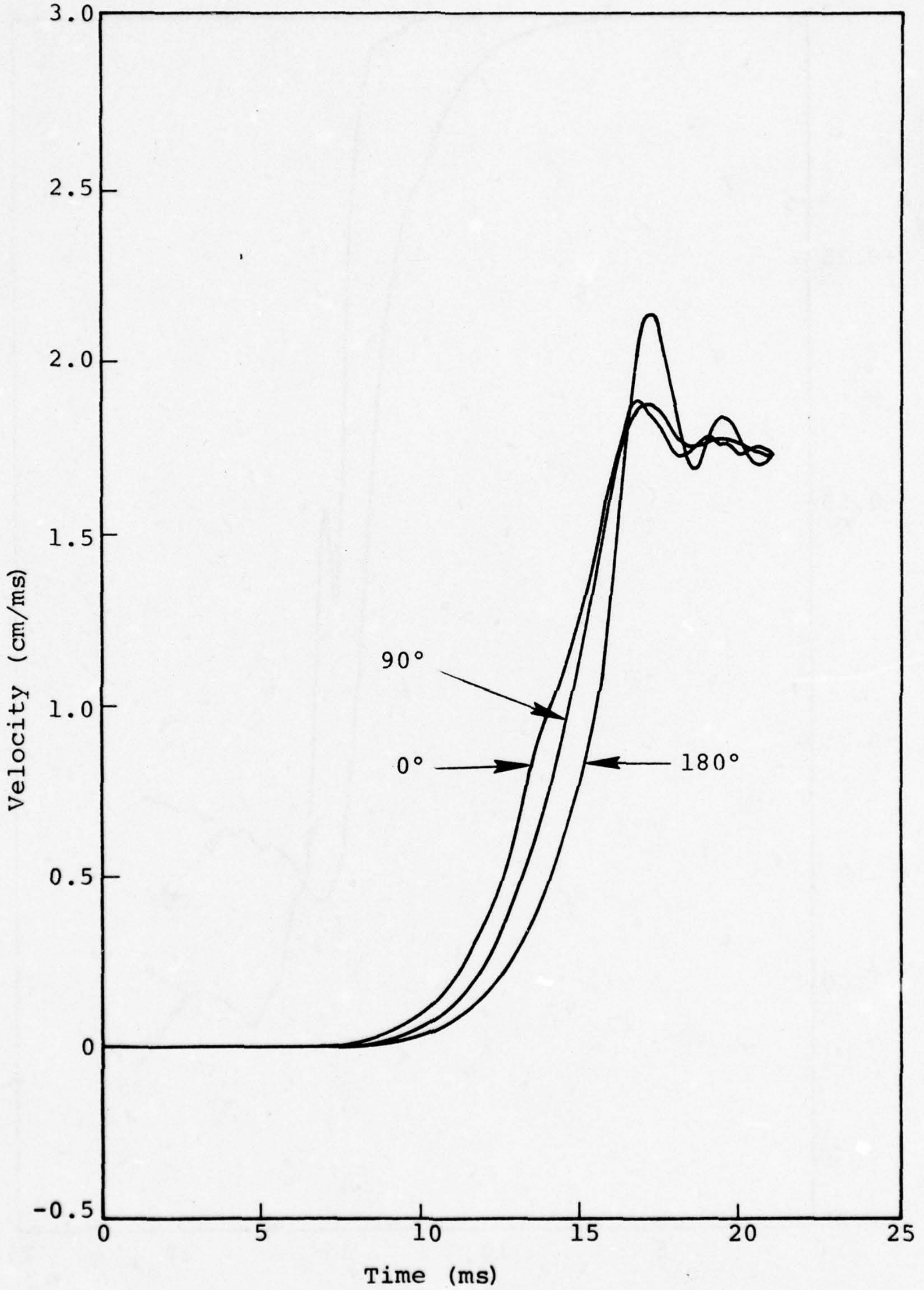

Figure 19. Velocity waveforms at the inner surface of the steel liner of the cellular concrete structure at the 0°, 90° (or 270°) and 180° locations.

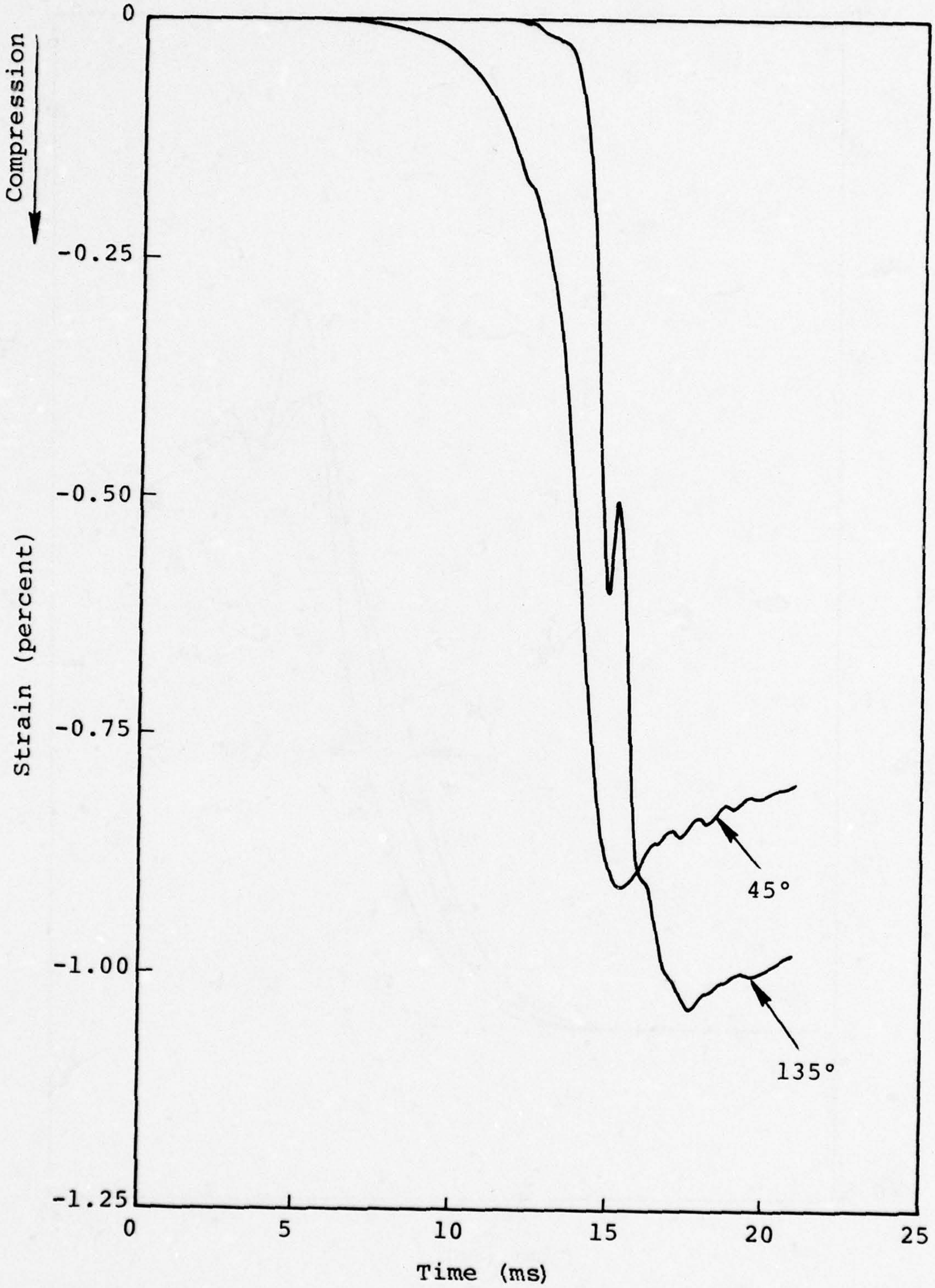

Figure 20. Hoop strain waveforms in the center of the cellular concrete at the 45° (or 315°) and 135° (or 225°) locations.

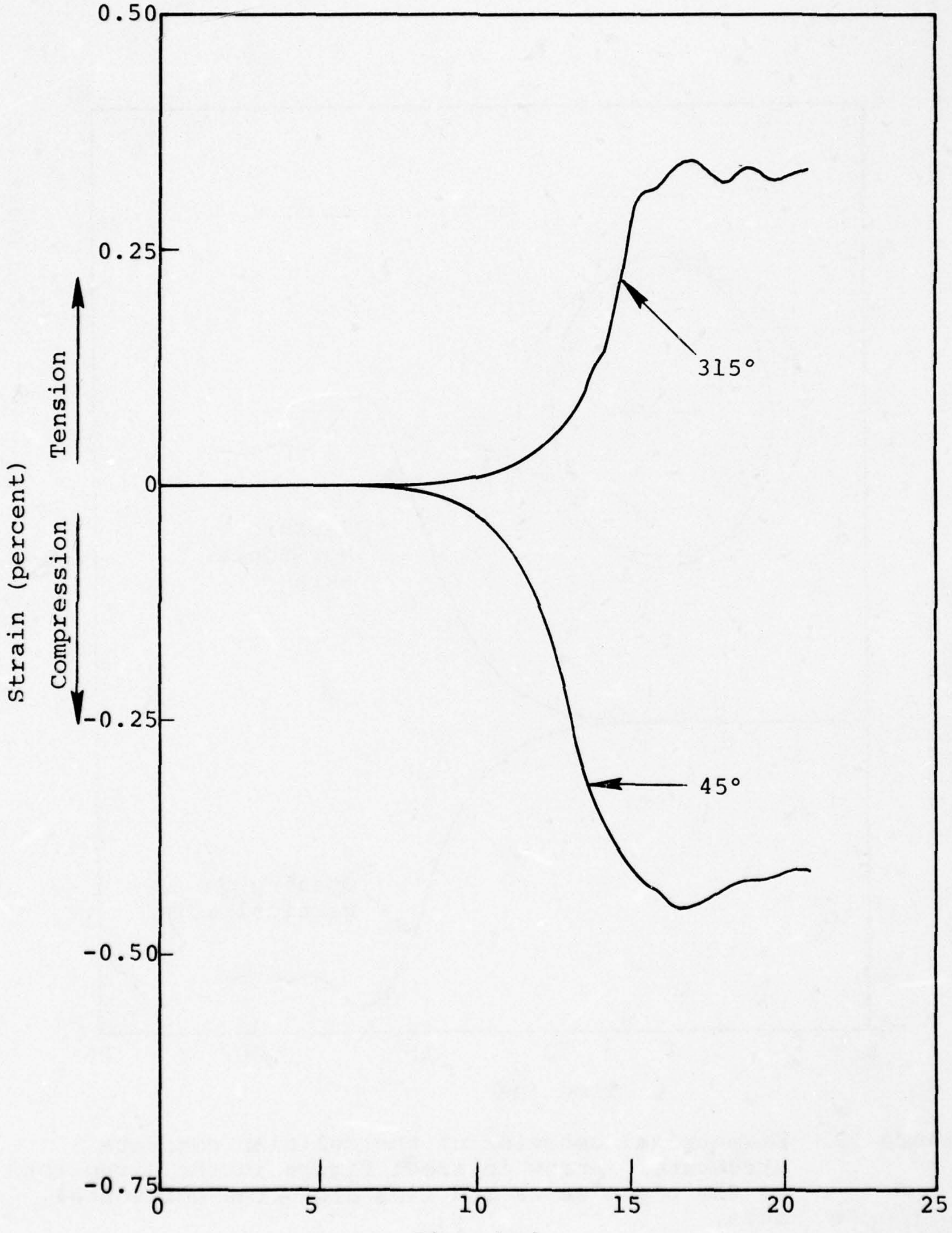

Figure 21. Hoop strain waveforms at the steel inner surface of the cellular concrete structure at the 45° (or 315°) and 135° (or 225°) locations.

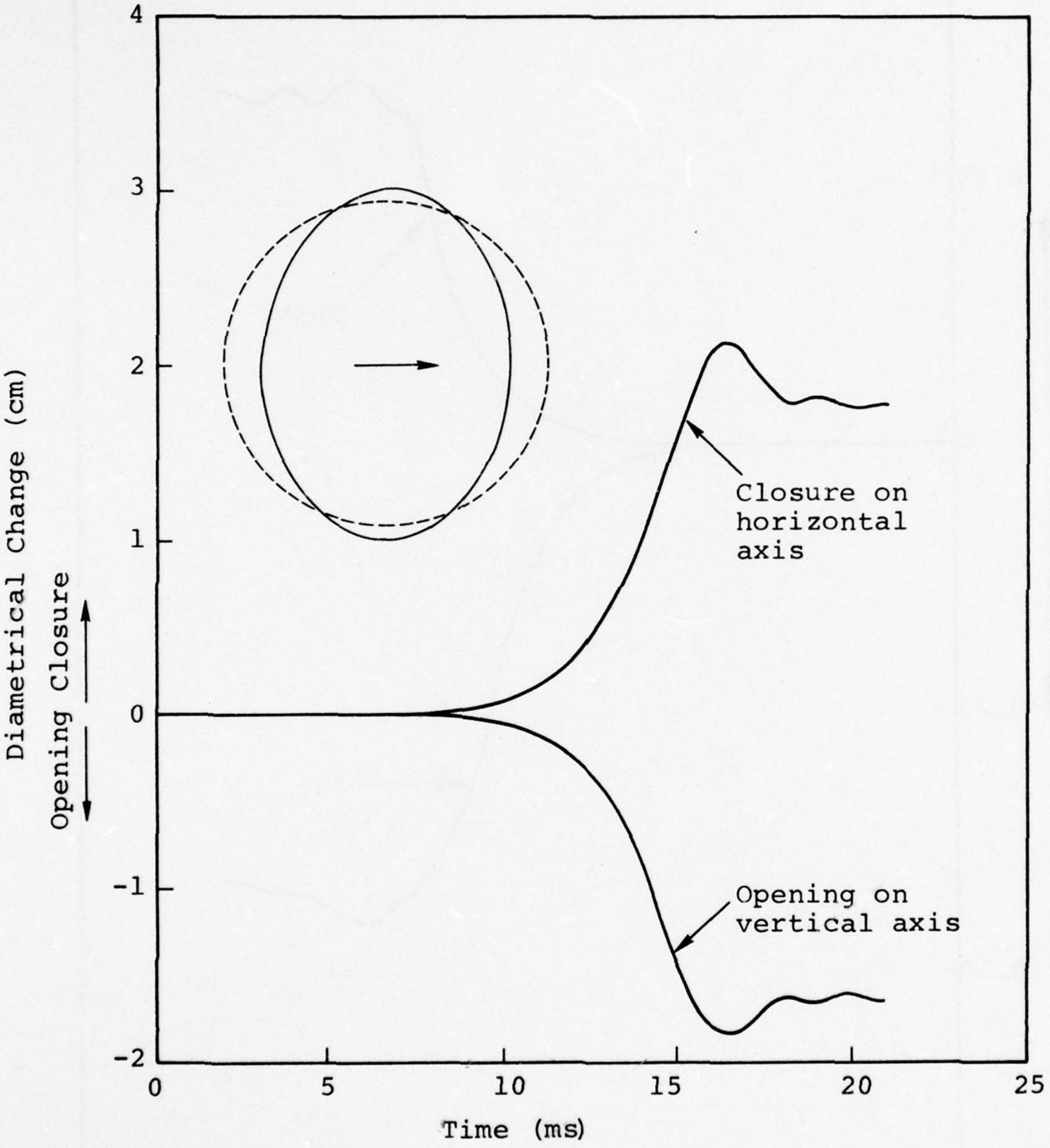

Figure 22. Diametrical behavior of the cellular concrete structure. Arrow in inset figure is the direction of the plane waves and lies along the horizontal axis.

CHAPTER IV

SUMMARY AND DISCUSSION

Results presented in the previous section serve to illustrate the difference in the three designs analyzed in this study. The unlined cavity does not attempt to increase the strength inherent in the surrounding tuff; while the reinforced concrete approach relies on the strength of the composite structure for integrity. However, as illustrated in Figure 15, the steel lining experiences a significant strain environment in the reinforced design concept. The use of cellular concrete reduces the maximum strain in the steel liner by approximately a factor of three.

Maximum cavity closure also varies significantly among the three cavity configurations. These values are approximately 7.5 cm, 3.8 cm and 2 cm for the unlined cavity, reinforced composite and cellular composite, respectively. The cellular concrete approach is obviously more effective since it decouples the behavior of the interior of the structure from the behavior of the surrounding tuff medium. This important advantage of the cellular concrete design can become even more significant for media with compressive strengths greater than tuff. For this type of medium, the reinforced design must also be strengthened to be effective. The disadvantage of this concept is that it may become prohibitively impractical to strengthen concrete much beyond 8000 psi. It should be cautioned that the effectiveness of the cellular concrete can be reduced if it becomes saturated with water. This is an important fact considering the wet environment of underground structures.

REFERENCES

Baron, M. L., H. H. Bleich, and P. Weidlinger, "Dynamic Elastic-Plastic Analysis of Structures," ASCE, J. Eng. Mech. Div., 87 (1961).

Baron, M. L. and A. T. Mathews, "Diffraction of a Pressure Wave by a Cylindrical Cavity in an Elastic Medium," J. Appl. Mech., 28, Series E (1961).

Baron, M. L., "Cap Model for Tuff," Deep Based Structures Modeling and Analysis Requirements Meeting, Defense Nuclear Agency (1975).

Bathe, K. J., H. Ozdemir, and E. L. Wilson, "Static and Dynamic Geometric and Material Nonlinear Analysis," Structural Engineering Laboratory, University of California, Berkeley, Report No. UCSESM 74-4 (1974).

Butcher, B. M., "Numerical Techniques for One-Dimensional Rate-Dependent Porous Material Compaction Calculations," Sandia Laboratories Research Report, SC-RR-710112 (1971).

Carroll, M. and A. C. Holt, "Suggested Modification of the P-α Model for Porous Materials," J. Appl. Physics, Vol. 43 (1972).

Cherry, J. T., J. Sweet, and E. J. Halda, "Prediction of Surface Vertical and Horizontal Displacements in Nonhomogeneous Media Resulting from Subsurface Nuclear Explosions," Systems, Science and Software Report SSS-R-73-1517 (1973).

DiMaggio, F. L. and I. Sandler, "Material Model for Granular Soils," J. Engr. Mechs. Div., ASCE, June (1971).

Frazier, G. A. and C. M. Petersen, "3-D Stress Wave Code for the ILLIAC IV," Systems, Science and Software Report No. SSS-R-74-2103 (1974).

Garnet, H. and J. Crouzet-Pascal, "Transient Response of a Circular Cylinder of Arbitrary Thickness, in an Elastic Medium, to a Plane Dilatational Wave," J. Appl. Mech., Trans. ASME (1966).

Good, A. J., "A Porosity Model for the SKIPPER Code," Systems, Science and Software, Topical Report SSS-IR-72-1337, (1972).

Hermann, W., "Constitutive Equation for the Dynamic Compaction of Ductile Porous Materials," J. Appl. Physics, Vol. 40 (1969).

Hoff, G. C., "Shock-Absorbing Materials, Report 2, Cellular Concrete as a Backpacking Material," U.S. Army Engineer Waterways Experiment Station, Miscellaneous Paper C-82-8 (1972).

Hoff, G. C., "Cellular Concrete Studies, Project Camphor, Report 1, Laboratory Investigations," U. S. Army Engineer Waterways Experiment Station, Miscellaneous Paper C-82-8 (1972).

Hoff, G. C., Chief, Materials Properties Branch, Concrete Laboratory, personal communication to H. E. Lindberg, Stanford Research Institute (1975).

Lee, L. M., "Low Stress Shock Behavior of Cellular Concrete," Sandia Laboratories, Development Report SLA-73-0164 (1973).

Lindberg, H. E., "Large- and Small-Scale Buried Structures Experiment for MIGHTY EPIC," Experiment Plan, Stanford Research Institute (1975).

Maenchen, G. and S. Sack, "The TENSOR Code," in *Methods of Computational Physics*, Vol. 3, Academic Press, New York (1964).

Marcus, M., "Basic Theorems in Matrix Theory," in *National Bureau of Standards Applied Mathematics*, Series 57 (1960).

Mow, C. C. and Y. H. Pao, "The Diffraction of Elastic Waves and Dynamic Stress Concentrations," RAND Corporation, Report No. R-482-PR (1971).

Nelson, J., M. L. Baron and I. Sandler, in *Shock Waves and the Properties of Solids*, Syracuse Press (1971).

Nickell, R. E., "Direct Integration Methods in Structural Dynamics," *ASCE*, *J. Eng. Mech. Div.*, Vol. 99, pp. 303-317 (1973).

Powell, G. H., "Inelastic Dynamic Analysis," Conference on the Earthquake Resistant Design of Engineering Structures, Berkeley, California (1972).

Read, H. E. and C. J. Maiden, "The Dynamic Behavior of Concrete," Systems, Science and Software Topical Report 3SR-707 (1971).

Read, H. E. and G. A. Frazier, "Calculations of the Free Field Response of a Layered Soil Medium to Airblast Loading Using the 3-D SWIS Code and the Weidlinger Soil Cap Model," Systems, Science and Software Report No. SSS-R-75-2730, (1975).

Riney, R. D., J. K. Dienes, G. A. Frazier, S. K. Garg, J. W. Kirsch, D. H. Brownell and A. J. Good, "Ground Motion Models and Computer Techniques," Systems, Science and Software Report 3SR-1071, DNA2915Z, (1972).

Sandler, I. and D. Rubin, "A Modular Subroutine for the Cap Model," Defense Nuclear Agency Report DNA3875F (1976).

Sandler, I., J. P. Wright and M. L. Baron, "Data Report, Pretest Ground Motion Calculations for the Mixed Company Event of the Middle North Series," Paul Weidlinger, Consulting Engineer, New York, (1972).

Sandler, I., Personal Correspondence, letter to Dr. Kent Goering, Defense Nuclear Agency (1975A).

Sandler, I., Personal Communication, letter to Dr. Gene Sevin (1975B).

Sweet, J., "Two-Dimensional Stress Wave Models for Porous Media," Systems, Science and Software Report SSS-R-72-1351, (1972).

Sweet, J., G. A. Frazier and H. E. Read, "SWIS-SMI, A Nonlinear Finite Element Code with Application for Static or Dynamic Structure-Media Interaction Problems," Systems, Science and Software Internal Report, SSS-IR-76-2830 (1976).

Sweet, J., "Dynamic Response of Underground Structures," Systems, Science and Software Report SSS-R-76-2829 (1976A).

Sweet, J., "Dynamic Response of a Buried Cylinder-SWIS Simulation," Systems, Science and Software Report SSS-R-76-2948 (1976B).

APPENDIX A

SWIS FINITE ELEMENT COMPUTER CODE - NONLINEAR VERSION

The SWIS Finite element computer code (Frazier and Petersen, 1974 and Sweet, et al., 1976) considers either static or dynamic problems in one-, two-, and three-dimensional geometries with equal efficiency. In addition, both nonlinear and linear behavior may be analyzed. The dynamic calculations may be performed using either the explicit or implicit time integration schemes. Also, for explicit dynamic calculations, SWIS has the capability of varying the time step within the computational mesh. This capability has been quite useful for structure-medium calculations (Sweet, 1976A and Sweet, 1976B). The present discussion primarily concerns the nonlinear version of the SWIS code. However, comparisons with known linear theoretical solutions are also included for information purposes.

A.1 INTRODUCTION

SWIS has been formulated in a manner that is similar to Lagrangian finite difference techniques in several respects. The spatial discretization is performed at each computational step to preclude the formation of a stiffness matrix. Also, stress is computed from strain in an incremental fashion explicitly in each element at each computational step. The resulting computational procedure, therefore, has the advantage of treating irregular geometries as well as the advantages of minimal storage requirements and the ease of incorporating nonlinear constitutive relationships.

The equilibrium equations are derived using conventional finite element techniques. Interpolation within skewed elements is accomplished in an isoparametric manner. This interpolation scheme is then combined with the virtual work expression to obtain the discrete governing equations. The mass matrix is diagonalized for computational efficiency. Element integrals are performed using a single-point quadrature. Bending within an element is modeled by utilizing the exact solution to simple bending (both linear and nonlinear bending solutions are applied when appropriate). This modified single-point quadrature technique has been demonstrated to be valid for several problem configurations (see Section A.5). A summary of the features of SWIS are as follows:

- Finite element formulation
- One-, two-, or three-dimensional spatial configurations
- Isoparametric elements with superior bending characceristics
- Lagrangian large displacement formulation
- Choice of several nonlinear material models
- Dynamic calculations using explicit central difference time integration
- Equilibrium calculations using the conjugate gradient method (static or dynamic implicit)
- The ability in a dynamic calculation to integrate a portion of the finite element mesh (usually the structure) using a smaller time step than in the surrounding elements
- Both regular and arbitrary element-node numbering
- Restart and graphics capabilities.

A.2 EXPLICIT DYNAMIC CALCULATIONS

SWIS employs a time-centered method for integrating the equilibrium equations for explicit calculations. Given the state of stress at time, t, the calculation procedure proceeds as follows:

(1) Restoring forces for each element are computed to determine the global restoring force vector which, in turn, determines the acceleration at t, $\ddot{u}(t)$.

(2) The velocity, displacement and nodal position vectors are updated as follows:

$$\dot{u}(t + \frac{dt}{2}) = \dot{u}(t - \frac{dt}{2}) + dt\ \ddot{u}(t)$$

$$u(t + dt) = u(t) + dt\ \dot{u}(t + \frac{dt}{2})$$

$$x\ (t + dt) = x(t) + dt\ \dot{u}(t + \frac{dt}{2})$$

(3) Strain rate at time $t + \frac{dt}{2}$ is determined from the velocity vector.

(4) Stresses at time $t + dt$ are determined from stresses at time, t, and the strain rate at time $t + \frac{dt}{2}$ using nonlinear constitutive relations. The stress tensor is also modified to account for material rotations.

(5) Time is incremented and steps (1) - (4) are repeated.

A.3 STATIC AND IMPLICIT DYNAMIC CALCULATIONS

The incremental discrete equilibrium equations for a dynamic configuration may be written in the following form

$$m\Delta\ddot{u}^n = \Delta F^n + \Delta R^n \qquad \text{(A-1)}$$

where $\Delta g = g^n - g^{n-1}$, m is the mass matrix, $\ddot{u}$ is the acceleration vector, F is the applied force vector, R is the restoring force vector, and the superscript n refers to time t^n. Time integration is accomplished by using either the midpoint constant acceleration algorithm (Powell, 1972) or the

Newmark β-method (Nickell, 1973). In either case, the acceleration increment at t^n can be expressed as a function of the displacement increment Δu^n and the motion at time t^{n-1}, i.e.,

$$\Delta \ddot{u}^n = a\ \Delta u^n + b^{n-1} \tag{A-2}$$

where a is a known constant and b is a function of the motion at time t^{n-1}. A first order approximation for ΔR^n is given by

$$\Delta R^n = \left(\frac{\partial R}{\partial u}\right)^{n-1} \Delta u^n \tag{A-3}$$

Combining Equations (A-1) - (A-3) yields

$$A\ \Delta u^n = B \tag{A-4}$$

where A is the effective stiffness matrix and B is the effective restoring force. These terms are defined by

$$A = m\ a - \left(\frac{\partial R}{\partial u}\right)^{n-1}$$

$$B = \Delta F^n - m\ b^{n-1}$$

Equation (A-4) is solved in SWIS using the conjugate gradient method (Marcus, 1960).

Since the stiffness term A is evaluated at time t^{n-1}, the above approach yields an unbalanced nodal force at the end of each time step. The procedure used in SWIS to obtain the correct solution is to use the solution of Equation (A-4) as the first approximation, ${}^{(1)}\Delta u^n$. The unbalanced forces are then used to obtain the next iteration and this procedure is repeated until convergence is noted (Bathe, et al. 1974). This iterative procedure for the k^{th} iteration is summarized by the following equation:

$$A\left({}^{(k)}\Delta u^n - {}^{(k-1)}\Delta u^n\right) = \Delta F^n + {}^{(k-1)}R^n$$

$$- R^{n-1} + m\left(\ddot{u}^{n-1} - {}^{(k-1)}\ddot{u}^n\right)$$

where ${}^{(1)}R^n$ equals R^{n-1}. In order to make this iteration procedure more efficient, the secant modulus may be used to define the matrix, A. Nonlinear static calculations are performed by eliminating the inertial terms and interpreting t^n as load step n.

A.4. MATERIAL MODELS

A.4.1 Von Mises Plasticity Model

The von Mises plasticity model is a constitutive relationship that models a material as an elastic-perfectly plastic continuum. The deviatoric stress tensor, S_{ij}, is related to the total stress tensor by

$$S_{ij} = \sigma_{ij} - \sigma_{kk}\frac{\delta_{ij}}{3}$$

A yield function is defined as

$$F = \sqrt{\frac{1}{2} S_{ij} S_{ij}} - \frac{Y}{\sqrt{3}}$$

where Y is the one-dimensional yield stress. The deviatoric behavior is assumed to be elastic when

$$F < 0$$

and perfectly plastic when

$$F = 0.$$

According to the associated flow rule, the strain tensor, ε_{ij}, is assumed to be composed of elastic and plastic components,

$$\varepsilon_{ij} = \varepsilon^{e}_{ij} + \varepsilon^{p}_{ij}$$

and the plastic strain rate tensor is related to the yield function by

$$\dot{\varepsilon}^{p}_{ij} = \lambda \frac{\partial F}{\partial \sigma_{ij}}$$

where λ is a scalar multiplier. The elastic strain rate tensor is assumed to be related to the state of stress by Hooke's law. This relationship becomes

$$\dot{S}_{ij} = 2\mu \left(\dot{\varepsilon}^{e}_{ij} - \dot{\varepsilon}^{e}_{kk} \frac{\delta_{ij}}{3} \right)$$

where μ is the shear modulus (assumed to be constant). Assuming a plastic state of stress ($F = 0$) yields the following expressions for λ and $\dot{S}_{ij}$

$$\lambda = \frac{\sqrt{3}\, \dot{\varepsilon}_{ij} \, S_{ij}}{Y}$$

$$\dot{S}_{ij} = 2\mu \left(\dot{\varepsilon}_{ij} - \dot{\varepsilon}_{kk} \frac{\delta_{ij}}{3} - \frac{\sqrt{3}\, \lambda}{2Y} S_{ij} \right) .$$

For completeness, the hydrostatic state of stress is defined as a function of the state of strain. In nonlinear analyses, the pressure, p ($\equiv -\sigma_{kk}/3$), is usually represented as a polynomial function of ($\rho/\rho_o - 1$), i.e.,

$$p = \sum_{i=1}^{n} A_i \left(\frac{\rho}{\rho_o} - 1 \right)^{i}$$

where ρ is the density and the density ratio is related to the strain by

$$\frac{\rho}{\rho_o} = \exp\left(-\varepsilon_{kk}\right) \quad .$$

The propagation of a plane wave in an elastic-perfectly plastic material has been simulated in SWIS. The result of this calculation is depicted in Figure A.1 where the correlation is seen to be excellent.

A.4.2 Soil Cap Constitutive Model

The soil cap model (DiMaggio and Sandler, 1971; Read and Frazier, 1975; and Sandler and Rubin, 1976) is a plasticity model whose plastic strain rate vector is normal to the yield surface in stress space. The yield surface (depicted in Figure A.2) is composed of a fixed failure envelope that encompasses a movable hardening cap.

Defining J_1 and J_2' as:

$$J_1 = \sigma_{kk}$$

$$J_2' = \frac{1}{2} S_{ij} S_{ij},$$

the yield function is given by

$$F = \begin{cases} F_1 = \sqrt{J_2'} - [A - C \exp(B J_1)] & , \text{ if } L \le J_1 , \\ F_2 = (J_1 - L)^2 + R^2 J_2' - (X - L)^2 & , \text{ if } L > J_1 \end{cases}$$

where X and L are defined as

$$X(\varepsilon^p_{kk}) = \ln\left[\left(1 - \frac{\varepsilon^p_{kk}}{W}\right)^{-1}\right]/D + X_0$$

$$L(\varepsilon^p_{kk}) = \begin{cases} \ell \text{ for } \ell \ge 0 \\ 0 \text{ for } \ell < 0 \end{cases}$$

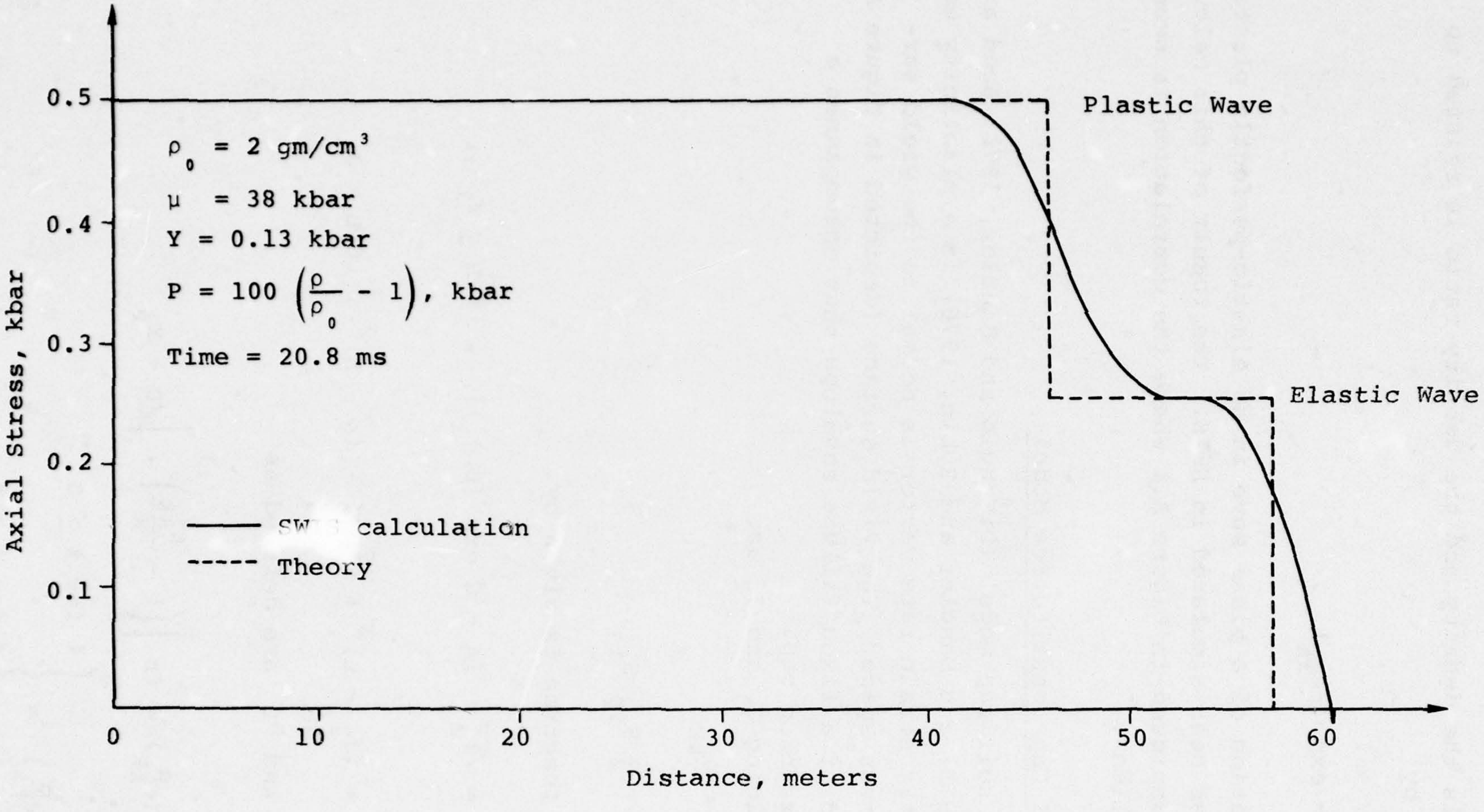

Figure A.1. Comparison of SWIS and theoretical solutions for an elastic-plastic uniaxial strain calculation.

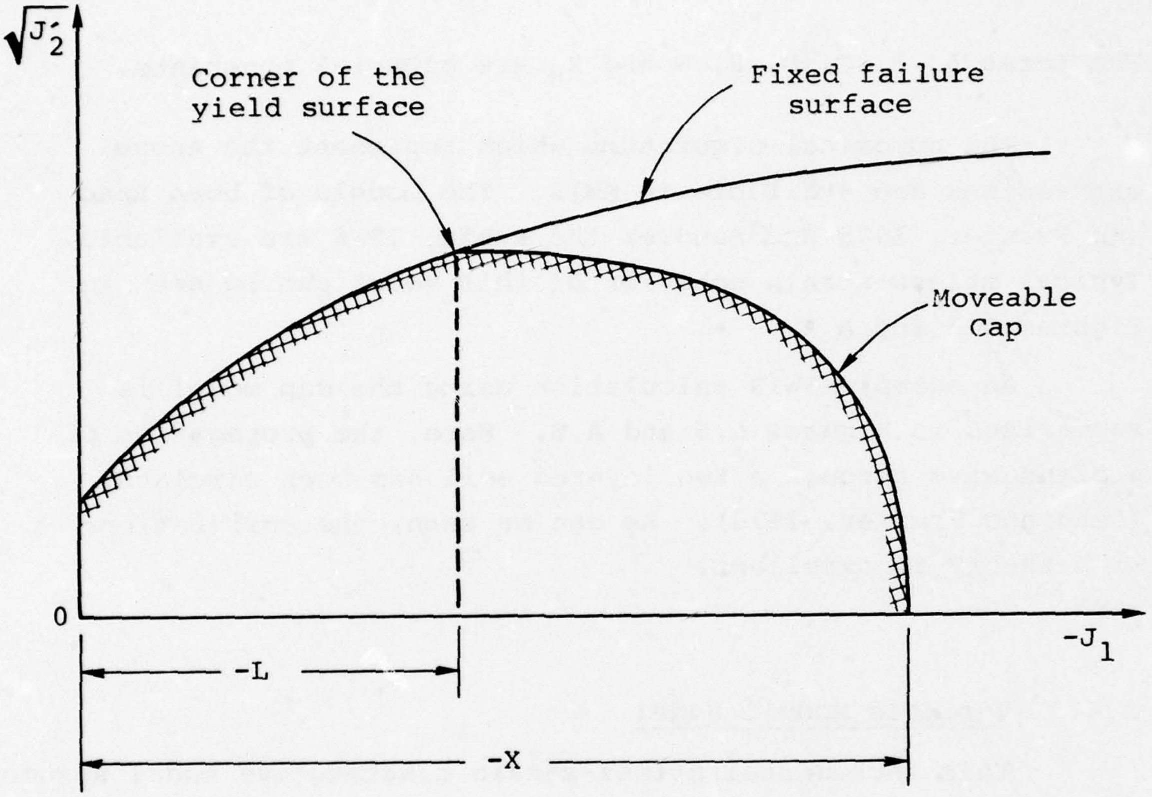

Figure A.2. The yield surface of the soil cap model.

and ℓ satisfies

$$\ell + R\,[A - C \exp(-B\ell)] = X\,(\varepsilon^{p}_{kk}) \quad .$$

The terms A, B, C, D, R, W and X_0 are material constants.

The numerical algorithms which represent the above expressions are available in SWIS. The models of both Read and Frazier, 1975 and Sandler and Rubin, 1976 are available. Typical stress-strain behavior of this model can be seen in Figures A.3 and A.4.

An example SWIS calculation using the cap model is summarized in Figures A.5 and A.6. Here, the propagation of a plane wave through a two layered soil has been simulated (Read and Frazier, 1975). As can be seen, the correlation with theory is excellent.

A.4.3 Variable Moduli Model

This incremental stress-strain constitutive model assumes that the material behavior can be separated into volumetric and deviatoric parts with no explicit yield behavior (Nelson, et al., 1971). This separation automatically precludes dilatancy in the material. Both the bulk (volumetric) modulus and shear (deviatoric) modulus depend upon the stress and/or strain invariants and the previous loading history.

The bulk modulus is assumed to obey the following relationship:

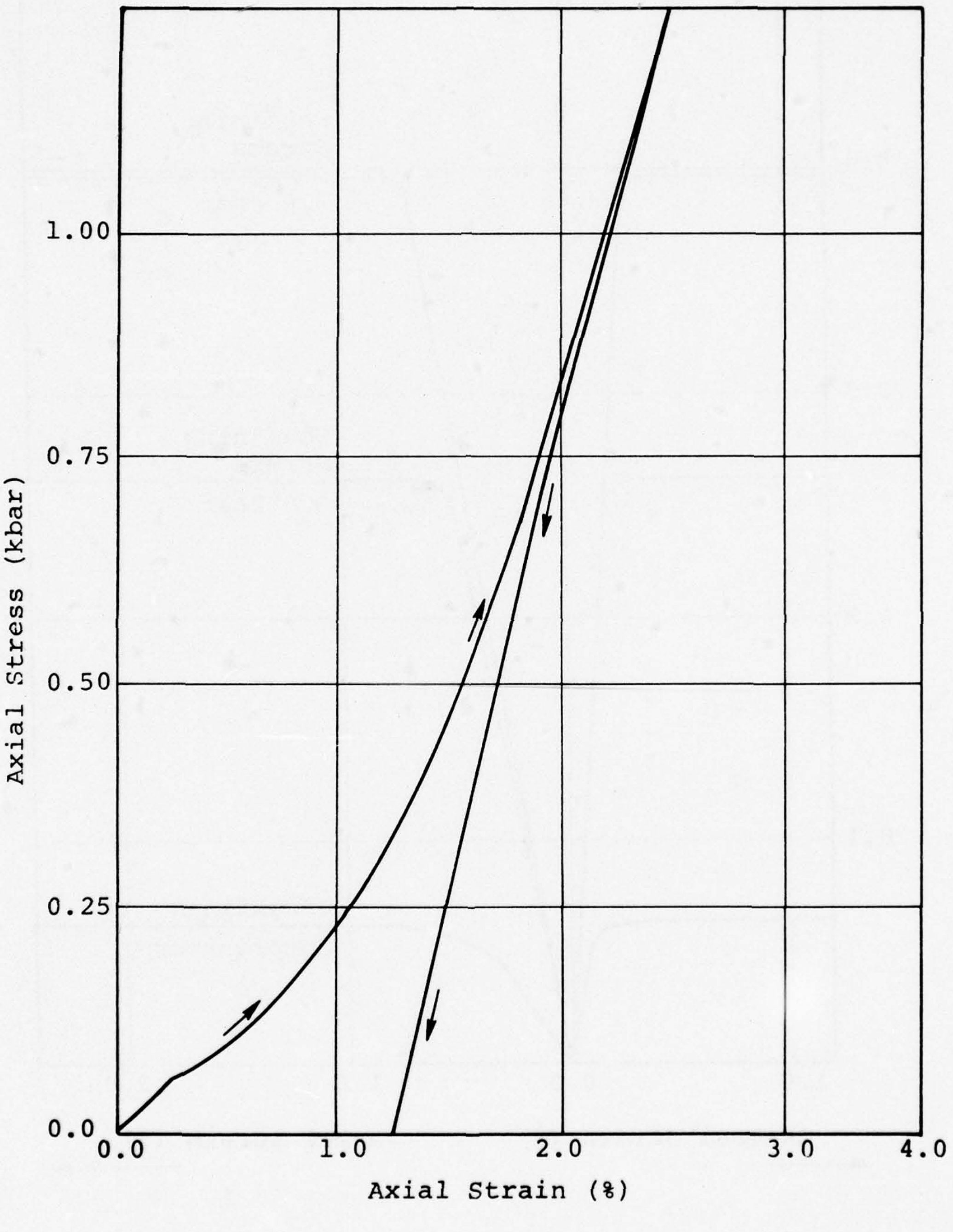

Figure A.3. Typical uniaxial strain behavior of the soil Cap model.

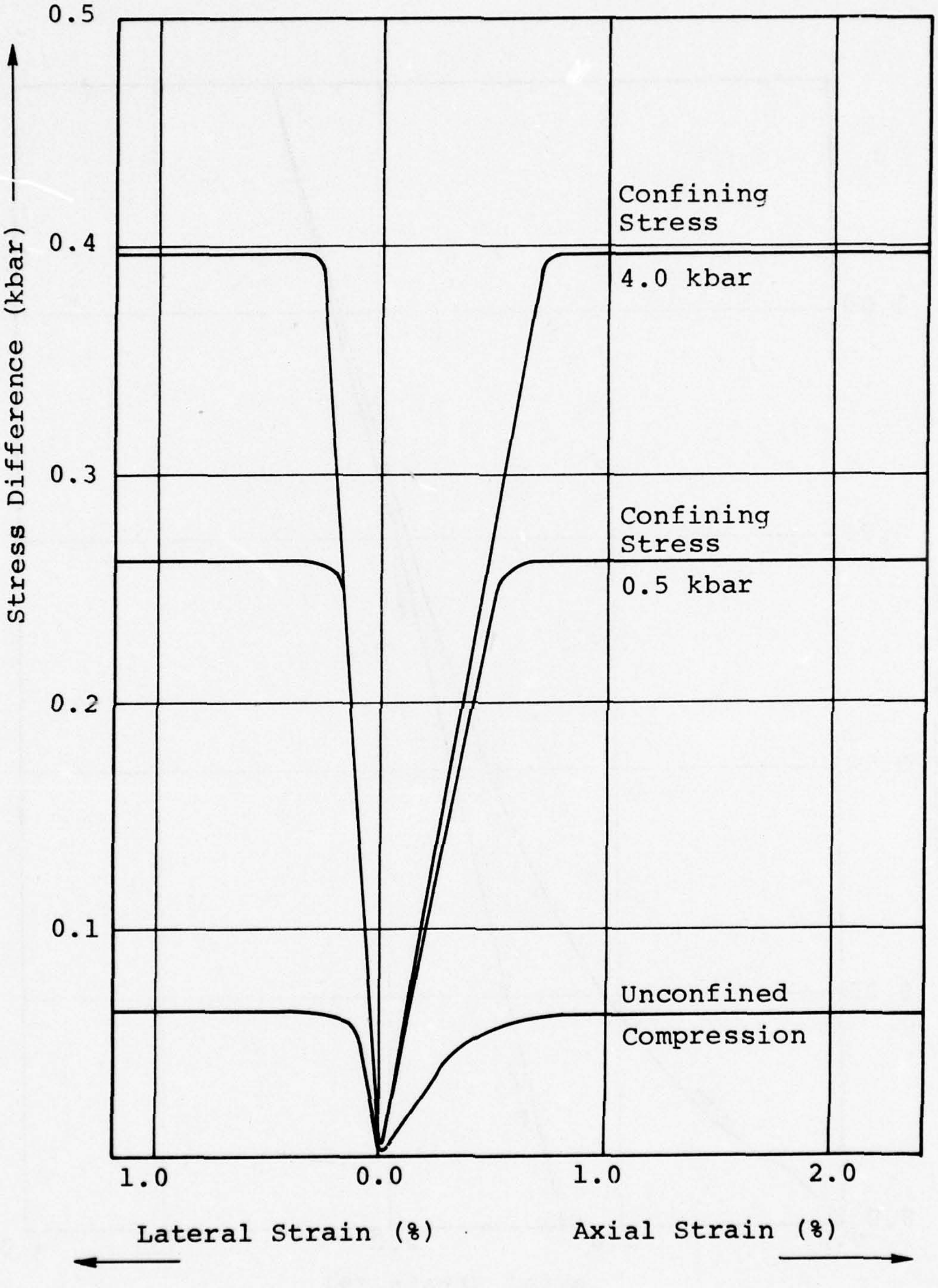

Figure A.4. Typical uniaxial stress behavior of the soil Cap model.

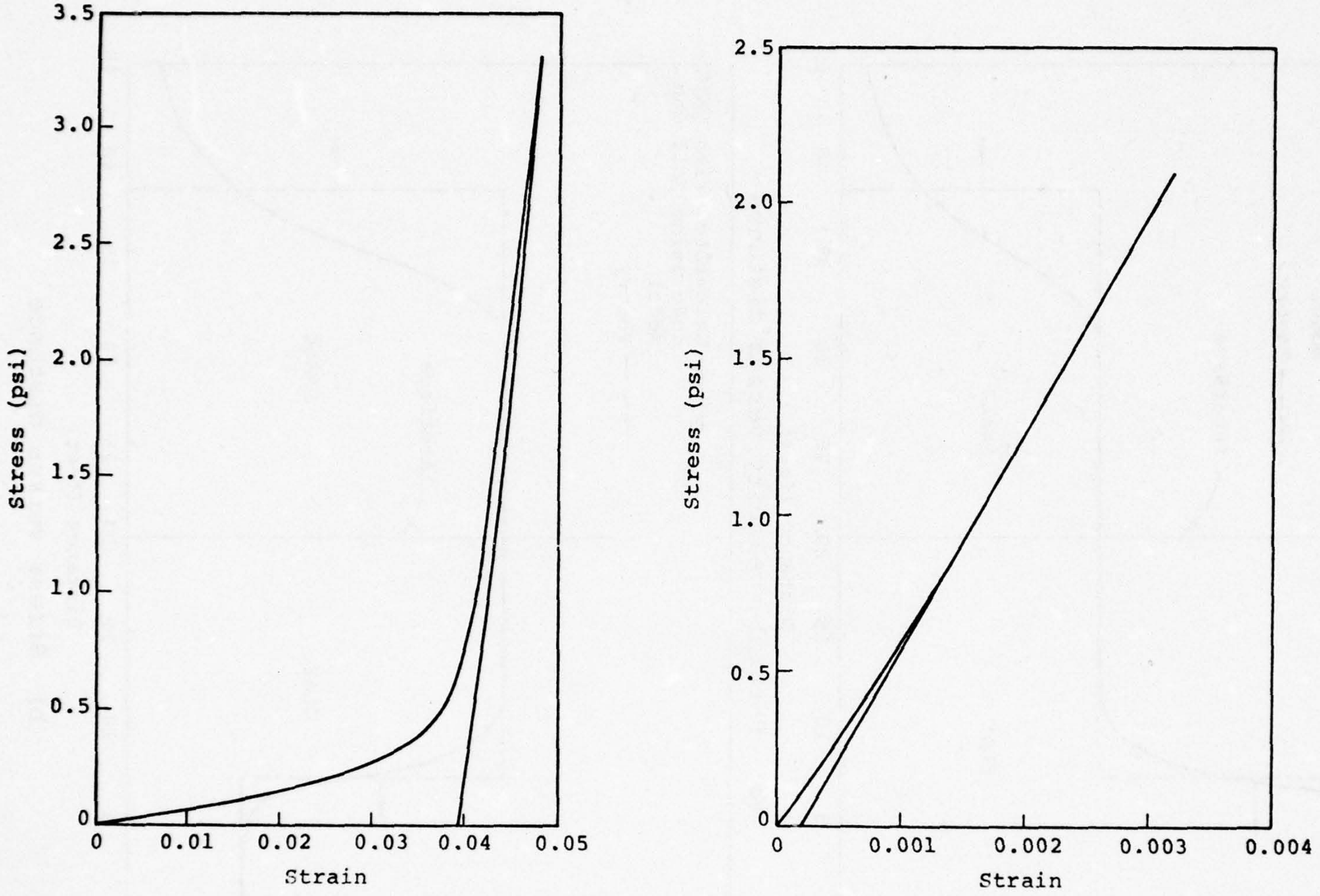

(a) Clay

(b) Shale

Figure A.5. The uniaxial strain response of the clay and shale used in two-layered example calculation. The materials are simulated using the soil cap model.

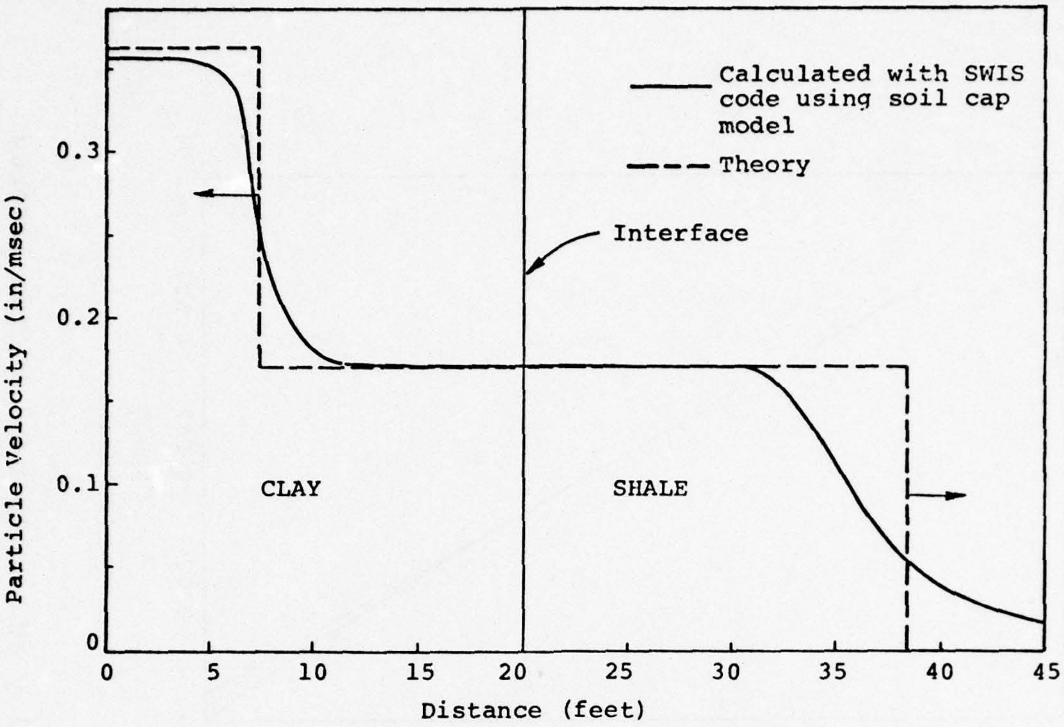

(a) Particle velocity versus distance

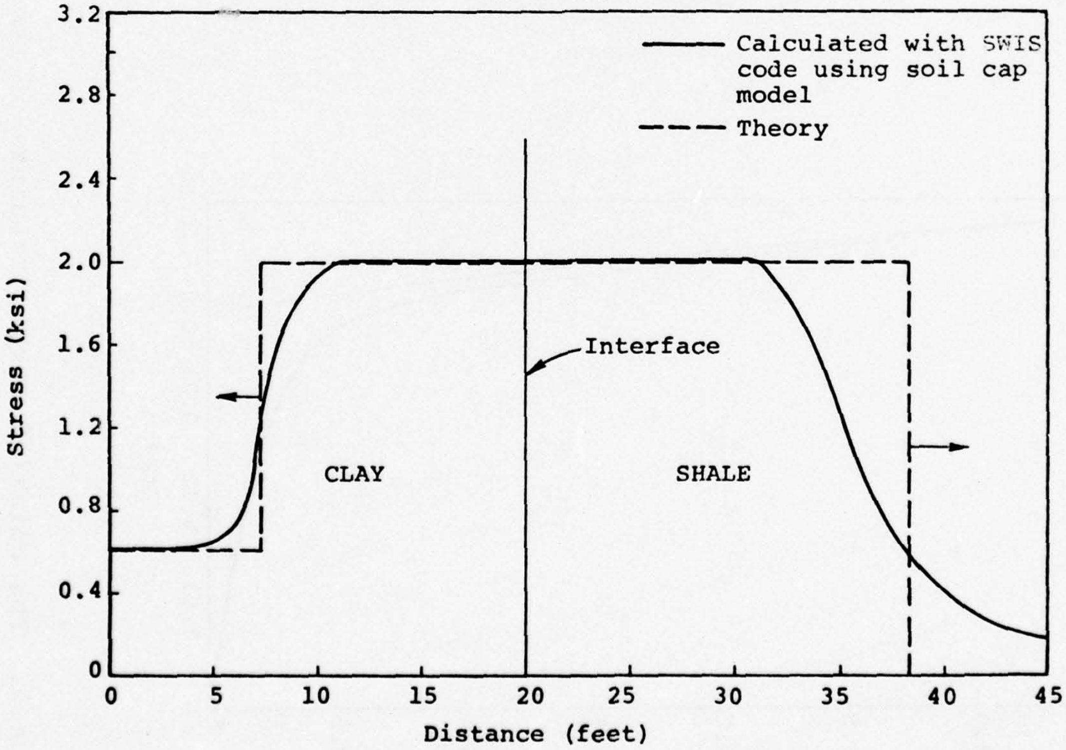

(b) Stress versus distance

Figure A.6. Comparison of theoretical and computational results for one-dimensional two-layered calculations.

$$K = \begin{cases} K_0 + K_1 e + K_2 e^2 & \text{when } p = p_{max} \text{ and } \dot{p} > 0 \\ K_0 \text{ when } p < p_{max} \text{ or } p = p_{max} \text{ and } \dot{p} < 0 \end{cases}$$

where p_{max} is the maximum previous pressure, e is the mean compressive strain and K_i are material parameters.

The shear modulus behavior is given by:

$$G = \begin{cases} G_0 + \gamma_1 p + \overline{\gamma}_1 \sqrt{J_2'} & \text{when } \dot{J}_2' > 0 \\ G_0 + \gamma_1 p & \text{when } \dot{J}_2' \leq 0 \end{cases}$$

where J_2' is the second deviatoric stress invariant, p is the pressure, and $(G_0, \gamma_1, \overline{\gamma}_1)$ are material parameters.

The above material model yields a behavior that is characterized by hardening in shear with increasing pressure and softening with increasing shear stress ($\gamma_1 > 0$ and $\overline{\gamma}_1 < 0$).

A.4.4 P-α Constitutive Model

The hydrostatic behavior of crushable materials may be represented using the "P-α" model (Herrmann, 1969; Riney, *et al.*, 1972; Good, 1972 and Carroll and Holt, 1972). This approach for representing the crushup of porous materials assumes that the equation-of-state of the solid (i.e., the non-porous material) is known. If the distension ratio, α, is defined as the ratio of the solid and porous densities, i.e.,

$$\alpha = \frac{\rho_s}{\rho} \quad ,$$

and the equation-of-state of the solid is given by

$$P_s = f(\rho_s) \quad ,$$

then the hydrostatic behavior of the porous material is assumed to be given by

$$P = \frac{1}{\alpha} f(\alpha\rho) \quad . \tag{A-5}$$

The P-α formulation is completed by specifying a functional relationship between α and P; a relationship that is usually experimentally determined. Writing this expression as

$$\alpha = \alpha(P) \quad , \tag{A-6}$$

the composite pressure, P, can be determined as a function of the composite density, ρ, by eliminating α from Equations (A-5) and (A-6). The term α may be related to the porosity, ϕ, by

$$\phi = 1 - \frac{1}{\alpha} \quad .$$

A typical stress-strain curve for crushable materials is depicted in Figure A.7. As can be seen, it is characterized by an initial nearly-linear behavior followed by a highly nonlinear character as the material crushes. These data can be utilized in order to formulate a P-α model if the behavior of the solid material is known. Assuming that the low kilobar stress regime is of interest, the solid equation-of-state becomes:

$$P_s = K_s \left(\frac{\rho_s}{\rho_{s_0}} - 1 \right) \quad . \tag{A-7}$$

Thus, using Equations (A-5) and (A-7), the composite pressure is given by

$$P = K_s \left(\frac{\rho}{\alpha_0 \rho_0} - \frac{1}{\alpha} \right)$$

or, in terms of the specific volume, $v \equiv \frac{1}{\rho}$ and the initial

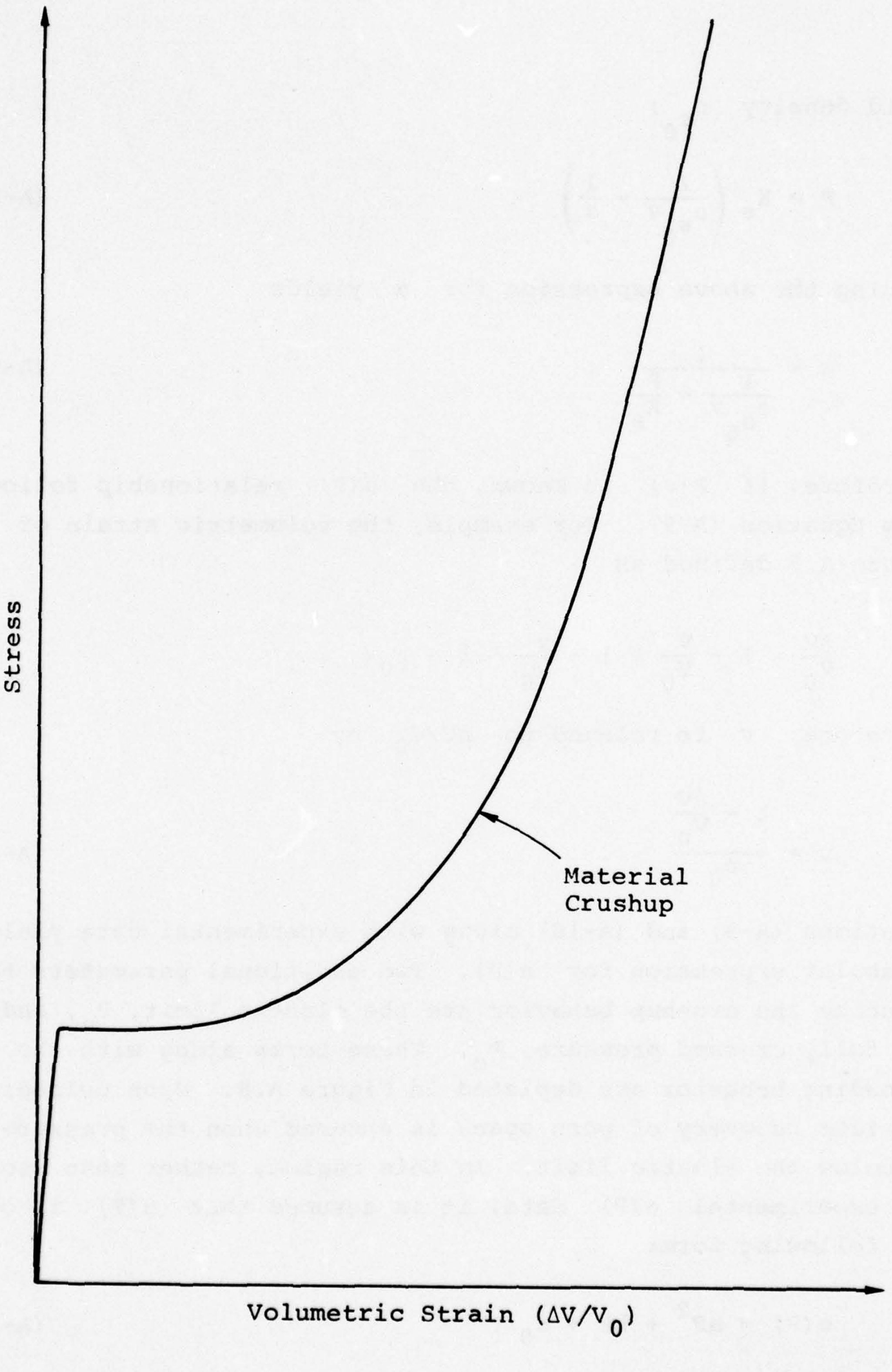

Figure A.7. Typical stress-strain curves for crushable materials.

solid density ρ_{s_0};

$$P = K_s \left(\frac{1}{\rho_{s_0} v} - \frac{1}{\alpha} \right) \quad . \tag{A-8}$$

Solving the above expression for α yields

$$\alpha = \frac{1}{\frac{1}{\rho_{s_0} v} - \frac{P}{K_s}} \quad . \tag{A-9}$$

Therefore, if $P(v)$ is known, the $\alpha(P)$ relationship follows from Equation (A-9). For example, the volumetric strain of Figure A.7 defined as

$$\frac{\Delta V}{V_0} = 1 - \frac{V}{V_0} \equiv 1 - \frac{v}{v_0} \equiv 1 - \rho_0 v \quad .$$

Therefore, v is related to $\Delta V/V_0$ by:

$$v = \frac{1 - \frac{\Delta V}{V_0}}{\rho_0} \quad . \tag{A-10}$$

Equations (A-9) and (A-10) along with experimental data yield a tabular expression for $\alpha(P)$. Two additional parameters that describe the crushup behavior are the elastic limit, P_e, and the fully crushed pressure, P_c. These terms along with the unloading behavior are depicted in Figure A.8. Upon unloading, complete recovery of pore space is assumed when the pressure is below the elastic limit. In this regime, rather than use the experimental $\alpha(P)$ data, it is assumed that $\alpha(P)$ is of the following form:

$$\alpha(P) = aP^2 + bP + \alpha_0 \tag{A-11}$$

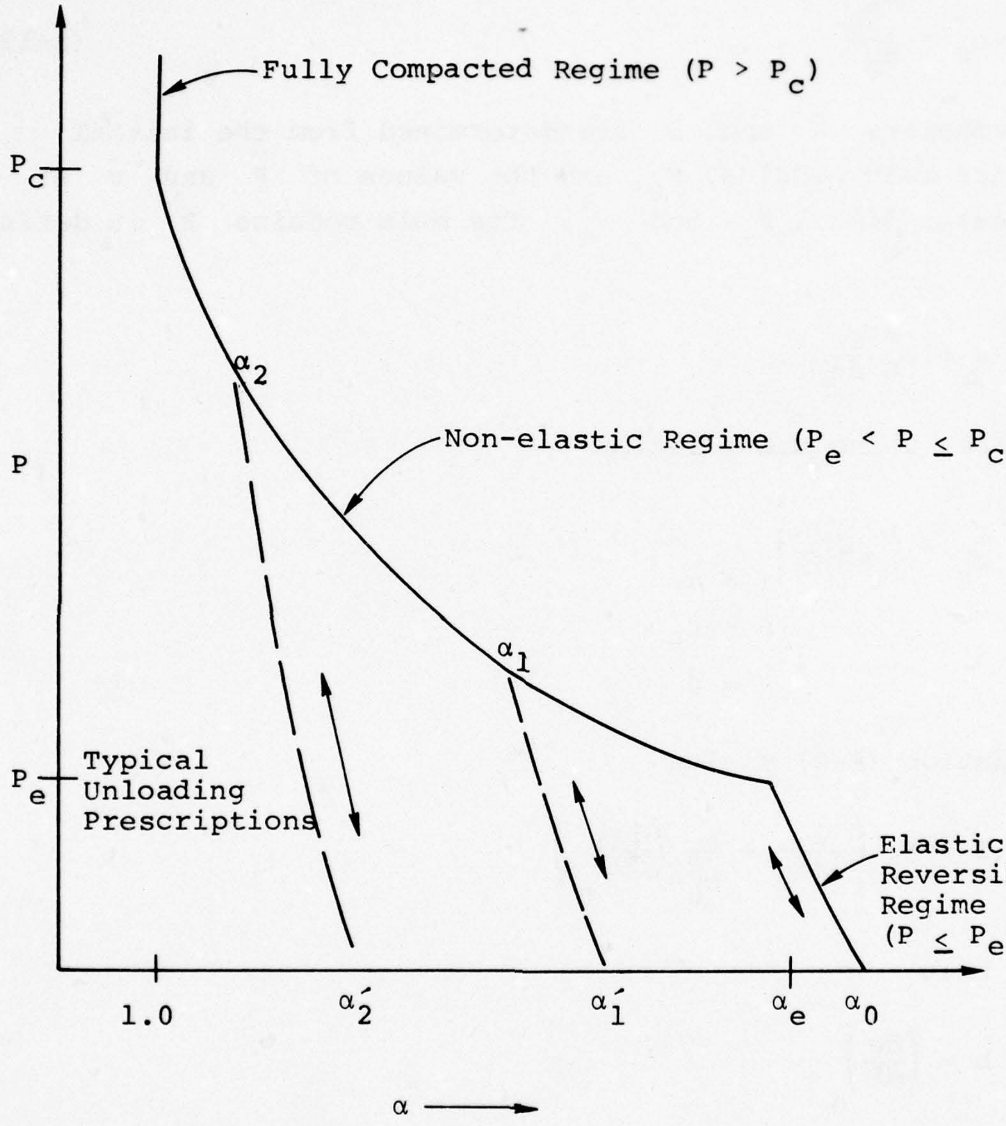

Figure A.8. Schematic of P-α model for the distension ratio, α(P). Note that above the elastic limit, release from a crush state occurs along a prescribed (reversible) release path which could result in some void recovery ($\alpha_2' > \alpha_2$). Release in the elastic regime is confined to the loading curve. After exceeding the crush pressure, P_C, the material loads/unloads according to the bulk modulus of the solid.

where α_0 is defined as

$$\alpha_0 = \frac{\rho_{s_0}}{\rho_0} \quad . \tag{A-12}$$

The parameters a and b are determined from the initial composite bulk modulus, K_0, and the values of P and v at the elastic limit, P_e and v_e. The bulk modulus K is defined as

$$K = \rho_0 \frac{dP}{d\rho} \quad .$$

Therefore, using the relation

$$\frac{1}{K_0} = \frac{1}{\rho_0} \left(\frac{d\rho}{dP}\right)_{\substack{\alpha = \alpha \\ \rho = \rho_0 \\ P = 0}}$$

and Equation (A-8) yields

$$1 = K_s \left(\frac{1}{\alpha_0 K_0} + \frac{1}{\alpha_0^2} \left(\frac{d\alpha}{dP}\right)_0 \right) \quad .$$

Noting that

$$b = \left(\frac{d\alpha}{dP}\right)_0$$

results in the following expression for b:

$$b = \alpha_0 \left(\frac{\alpha_0}{K_s} - \frac{1}{K_0} \right) \tag{A-13}$$

The parameter a is determined by evaluating Equation (A-11) at P_e' and becomes

$$a = \frac{\alpha_e - b P_e - \alpha_0}{P_e^2} \qquad \text{(A-14)}$$

where α_e follows from Equation (A-9)

$$\alpha_e = \frac{1}{\frac{1}{\rho_{s_0} v_e} - \frac{P_e}{K_s}} \quad . \qquad \text{(A-15)}$$

When the pressure is between the elastic limit and the crush pressure, the tabular expression for $\alpha(P)$ is used with Equation (A-8) to yield $P(v)$ or $\alpha(v)$. Partial pore recovery occurs when the pressure unloads from this regime. If α^* is the minimum value of α ever obtained and $\overline{\alpha}$ is the value of α using the tabulated $\alpha(v)$ relation, then the value of α *during unloading is given by (Good, 1972):*

$$\alpha = \frac{\alpha^* - \alpha_e}{1 - \alpha_e} (\alpha^* - \overline{\alpha}) + \overline{\alpha} \quad . \qquad \text{(A-16)}$$

Thus, during unloading, the amount of distension that is recovered is assumed to be linearly proportional to the excursion from the elastic limit.

Negative pressures are not allowed by the following technique. If a negative pressure is calculated, a new value of α is determined by setting P of Equation (A-8) to zero. This yields

$$\frac{1}{\rho_{s_0} v} - \frac{1}{\alpha} = 0$$

or

$$\alpha = \rho_{s_0} v \quad . \qquad \text{(A-17)}$$

In summary, the material properties required for the implementation of this constitutive model are:

- tabular $P\left(\frac{\Delta V}{V_0}\right)$ relation
- initial density and bulk modulus; ρ_0 and K_0
- solid properties, ρ_{s_0} and K_s

where the tabular $P\left(\frac{\Delta V}{V_0}\right)$ yields the values of P_e, P_c and v_e.

A.4.5 Tensile Failure Model

There exists a large class of problems where the geometry and/or loading configuration results in a significant region of interest where the tensile behavior is important. One modeling procedure that has been utilized to simulate tensile failure is to simply zero all calculated stresses which exceed the tensile strength (Sandler, et al., 1972). This technique is similar to approaches which alter the material stiffness properties in that it does not offer any insight concerning the inelastic strains (e.g., crack porosity) which result from tensile failure. The tensile failure model described here is an extension to the model presented by Maenchen and Sack, 1964 and Cherry, Sweet and Halda, 1973. Briefly, inelastic strains are introduced in order to zero those principal stresses which exceed the material tensile strength. The accumulation of these strains is the tensile failure-induced porosity. In the present analysis, careful attention is paid to the effect of this porosity on the determination of the mean stress from the equation of state.

The initial step in the computational procedure is to calculate the state of stress utilizing the equation of state for the mean stress and assuming elastic behavior to derive the deviatoric stresses. For a two-dimensional (x,y) configuration, these stresses are given by the deviatoric components (S_x', S_y', S_{xy}') and the mean stress P'. Using standard techniques, the principal stresses are given by

$$T_{11}' = -(P' + S_x' + S_y')$$

$$T_{22}', T_{33}' = -P' + \frac{1}{2}\left[S_x' + S_y' \pm \sqrt{(S_x'-S_y')^2 + (2S_{xy}')^2}\right] .$$

Each of these stresses is compared to the tensile strength of the mateiral if no previous tensile failure has occurred in the computational element. A zero tensile strength is appropriate if previous failure has taken place. When one of the principal stresses exceeds the tensile strength, an increment of strain in this direction is introduced to alter the primed state of stress. This strain increment is accumulated for each cycle and the sum for all three principal directions is interpreted as the tensile failure-induced porosity. The strain increment results in the principal stress increments (ΔT_{11}, ΔT_{22}, ΔT_{33}) and yields the following final state of stress:

$$\begin{aligned} T_{11} &= T_{11}' + \Delta T_{11} \\ T_{22} &= T_{22}' + \Delta T_{22} \qquad \text{(A-18)} \\ T_{33} &= T_{33}' + \Delta T_{33} . \end{aligned}$$

Upon fracturing, the stress increments must be chosen such that the principal stress that exceeded the tensile limit is "relaxed" to zero and also the mean stress resulting from the above expressions is consistent with the equation of state. This stress adjustment is assumed to occur with the deviatoric stress component determined using linear elasticity. Thus:

$$\Delta T_{ii} = -\Delta P - 2\mu \left(\Delta\varepsilon_{ii} - \frac{1}{3} \sum_{j=1}^{3} \Delta\varepsilon_{jj} \right) \qquad \text{(A-19)}$$

where ΔP is the increment in mean stress, μ is the shear modulus, and $\Delta\varepsilon_{ii}$ is the inelastic strain increment in the i^{th} direction. The sign of $\Delta\varepsilon_{ii}$ has been chosen so that a positive increment results in a positive change in the porosity content. The double subscripts do not denote summation. Using an approach similar to that developed for multi-phase material modeling (Riney, et al., 1972 and Sweet, 1972), the mean stress is given by

$$P = \frac{V_m}{V} f(V_m, E) \qquad \text{(A-20)}$$

where V is the specific volume of the computational cell, V_m is that portion of V occupied by the matrix material (volume of voids equals $V-V_m$), and f is the equation of state of the poreless matrix material. In general, the equation of state is assumed to be a function of V_m and the internal energy per unit mass, E.

As previously mentioned, the fracturing process introduces an increment of porosity in the calculational cell. Since the volume of the cell is not altered, this results in a change in the matrix content. Thus, the ΔP term required in Equation (A-19) and calculated from Equation (A-20) is given by

$$\Delta P = \frac{\partial P}{\partial V_m} \Delta V_m + \frac{\partial P}{\partial E} \Delta E \ . \qquad \text{(A-21)}$$

The use of Equation (A-21) ensures that, at least in an incremental sense, the adjusted mean stress satisfies the equation of state. The matrix volume change is related to the inelastic strain increments by

$$\Delta V_m = - V \sum_{i=1}^{3} \Delta\varepsilon_{ii} \qquad \text{(A-22)}$$

and the energy increment, ΔE, can be related to these strain increments and the state of stress using the energy equilibrium equation. This equilibrium relationship may be written

$$\dot{E} = - P \dot{V} + V S_{ij} \dot{e}_{ij}$$

where $\dot{e}_{ij}$ is the total strain rate tensor and S_{ij} are the deviatoric stresses. Remembering that the fracturing process does not change V, the above expression yields the following relationship:

$$\Delta E = - V \sum_{i=1}^{3} S'_{ii} \, \Delta\varepsilon_{ii} \equiv - V \sum_{i=1}^{3} \left(T'_{ii} + P'\right) \Delta\varepsilon_{ii} \; . \qquad \text{(A-23)}$$

When tensile failure occurs, any number of the primed principal stresses may exceed the tensile limit. The case when one of these stresses exceeds this limit will be investigated first. If this stress is T'_{11}, the strain increment $\Delta\varepsilon_{11}$ must be found. The stress increment ΔT_{11} equals $-T'_{11}$ and thus Equations (A-18) and (A-19) become

$$\begin{aligned} T_{11} &= T'_{11} - \Delta P - \tfrac{4}{3}\,\mu\Delta\varepsilon_{11} \equiv 0 \\ T_{22} &= T'_{22} - \Delta P + \tfrac{2}{3}\,\mu\Delta\varepsilon_{11} \\ T_{33} &= T'_{33} - \Delta P + \tfrac{2}{3}\,\mu\Delta\varepsilon_{11} \; . \end{aligned} \qquad \text{(A-24)}$$

Equations (A-21) - (A-23) are used to derive the expression for ΔP. This relationship becomes

$$\Delta P = - \left[V \frac{\partial P}{\partial V_m} + \frac{V}{V_0} \frac{\partial P}{\partial E} \left(T'_{11} + P'\right) \right] \Delta\varepsilon_{11} \qquad \text{(A-25)}$$

where the partial derivatives and pressure are evaluated at the primed stress state. Equation (A-25) may be written

$$\Delta P = K_{eff}\ \Delta\varepsilon_{11} \tag{A-26}$$

where K_{eff} is the effective bulk modulus and is defined by

$$K_{eff} = -\left[V\frac{\partial P}{\partial V_m} + \frac{V}{V_0}\frac{\partial P}{\partial E}\left(T'_{11} + P'\right)\right] .$$

Using Equation (A-26), Equation (A-24) becomes

$$\begin{aligned} T_{11} &= T'_{11} - \left(K_{eff} + \frac{4}{3}\mu\right)\Delta\varepsilon_{11} \\ T_{22} &= T'_{22} - \left(K_{eff} - \frac{2}{3}\mu\right)\Delta\varepsilon_{11} \\ T_{33} &= T'_{33} - \left(K_{eff} - \frac{2}{3}\mu\right)\Delta\varepsilon_{11} \end{aligned} \tag{A-27}$$

where, using Equation (A-24):

$$\Delta\varepsilon_{11} = \frac{T'_{11}}{K_{eff} + \frac{4}{3}\mu} . \tag{A-28}$$

When large tensile stresses are allowed before fracturing occurs, the direct application of Equation (A-27) and (A-28) can result in numerical instabilities if too large a stress drop is allowed on one cycle. This situation can be prevented by reducing the increment allowed by Equation (A-28) for the first few cycles after fracturing is initiated.

When two principal stresses exceed the tensile limit, say T'_{11} and T'_{22}, the strain increments $\Delta\varepsilon_{11}$ and $\Delta\varepsilon_{22}$ are introduced to "relax" both T_{11} and T_{22} to zero. The analysis is similar to that previously presented for one strain increment.

For this case, ΔP is given by

$$\Delta P = -V \frac{\partial P}{\partial V_m} \left(\Delta\varepsilon_{11} + \Delta\varepsilon_{22}\right) - V \frac{\partial P}{\partial E}\left[\left(T'_{11} + P'\right)\Delta\varepsilon_{11} + \left(T'_{22} + P'\right)\Delta\varepsilon_{22}\right] . \qquad \text{(A-29)}$$

As can be seen, its form does not lend itself to the definition of an effective bulk modulus. The stress state is now defined by

$$\begin{aligned} T_{11} &= T'_{11} - \Delta P - \frac{2}{3}\mu\left(2\Delta\varepsilon_{11} - \Delta\varepsilon_{22}\right) \equiv 0 \\ T_{22} &= T'_{22} - \Delta P - \frac{2}{3}\mu\left(2\Delta\varepsilon_{22} - \Delta\varepsilon_{11}\right) \equiv 0 \qquad \text{(A-30)} \\ T_{33} &= T'_{33} - \Delta P + \frac{2}{3}\mu\left(\Delta\varepsilon_{11} + \Delta\varepsilon_{22}\right) . \end{aligned}$$

Using Equation (A-29) and the first two equations of (A-30) yields expressions for $\Delta\varepsilon_{11}$ and $\Delta\varepsilon_{22}$. They are:

$$\begin{aligned} \Delta\varepsilon_{11} &= \frac{T'_{11}\left(b + \frac{4}{3}\mu\right) - T'_{22}\left(b - \frac{2}{3}\mu\right)}{\left(a + \frac{4}{3}\mu\right)\left(b + \frac{4}{3}\mu\right) - \left(b - \frac{2}{3}\mu\right)\left(a - \frac{2}{3}\mu\right)} \\ & \qquad \text{(A-31)} \\ \Delta\varepsilon_{22} &= \frac{T'_{22}\left(a + \frac{4}{3}\mu\right) - T'_{11}\left(a - \frac{2}{3}\mu\right)}{\left(a + \frac{4}{3}\mu\right)\left(b + \frac{4}{3}\mu\right) - \left(b - \frac{2}{3}\mu\right)\left(a - \frac{2}{3}\mu\right)} \end{aligned}$$

where a and b follow from rewriting Equation (A-29) as

$$\Delta P = a\Delta\varepsilon_{11} + b\Delta\varepsilon_{22}$$

and are given by

$$a = -V\frac{\partial P}{\partial V_m} - V\frac{\partial P}{\partial E}\left(T'_{11} + P'\right)$$

$$b = -V\frac{\partial P}{\partial V_m} - V\frac{\partial P}{\partial E}\left(T'_{22} + P'\right) .$$

When all of the principal stresses exceed the tensile limit, the material has become rubble and all of the stresses must be zeroed. For this case, the strain increments are all assumed to equal

$$\Delta\varepsilon_{ii} = \frac{P'}{3V\frac{\partial P}{\partial V_m}} \equiv \frac{-\Delta P}{3V\frac{\partial P}{\partial V_m}} . \qquad \text{(A-32)}$$

For a plane stress configuration, the above procedure is modified by introducing a crack porosity normal to the plane whose value is determined by constraining the normal stress to be zero.

The analysis just presented is also valid for crack closure. Once failure has occurred and nonzero crack porosity exists, Equation (A-28), (A-31) or (A-32) is used regardless of the sign of the principal stresses. The existence of compressive stresses automatically decreases the accumulated crack strain. This process is continued until the strain is detected to be negative. When this occurs, the strain component is equated to zero and the material is assumed to be "healed," with a future zero tensile strength.

A.5 EXAMPLE CALCULATIONS PERFORMED USING THE SWIS CODE

The following figures summarize several calculations that have been performed using the SWIS code. As can be seen, comparison with theory is excellent for all examples. Figures A.9 through A.11 demonstrate that the bending characteristics of the SWIS elements are valid for both linear and nonlinear behavior. Figure A.12 illustrates that the SWIS formulation is also valid for continuum wave propagation.

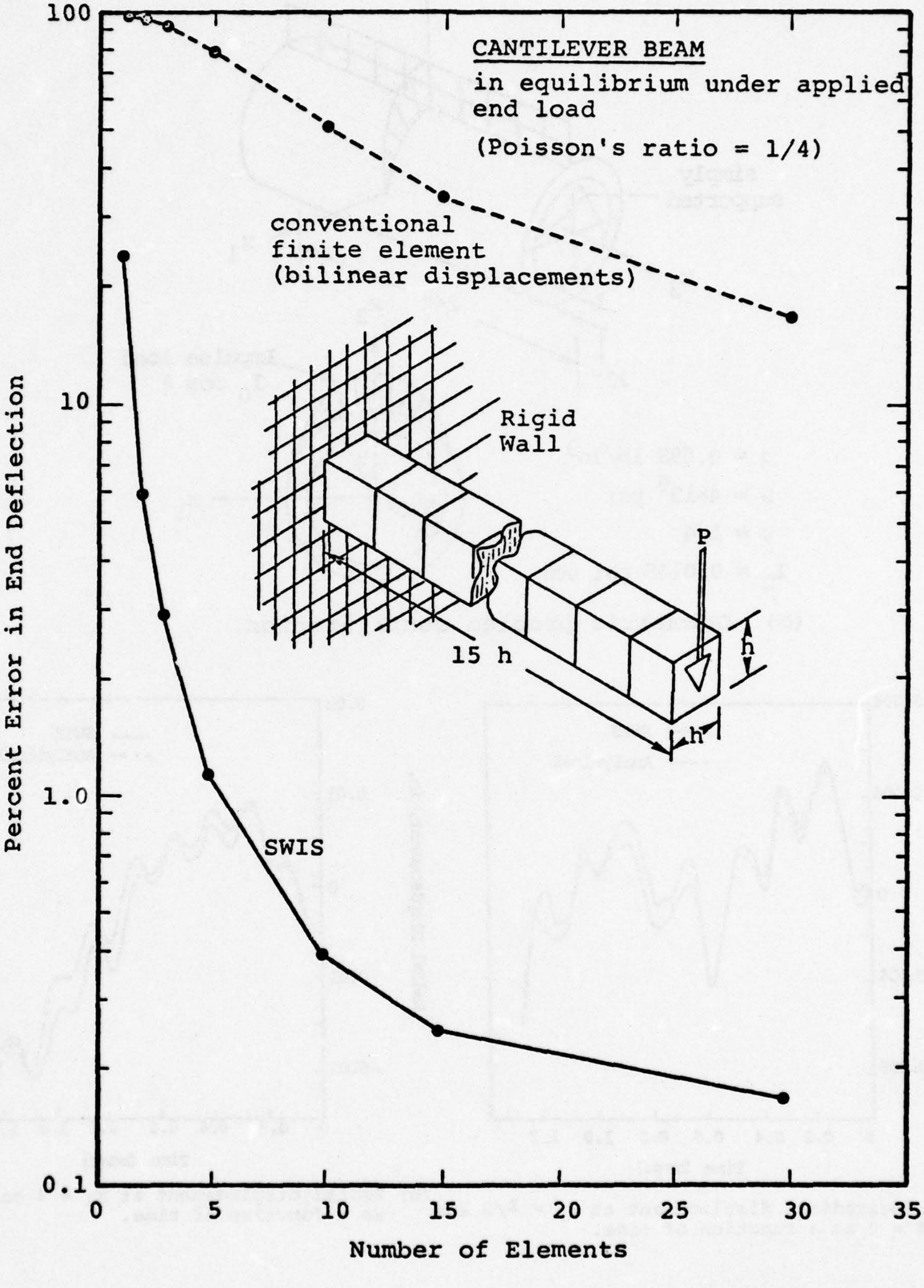

Figure A.9. A comparison of the bending scheme used in the SWIS code with that inherent in conventional bilinear finite elements for computing the end deformation of a cantilever beam.

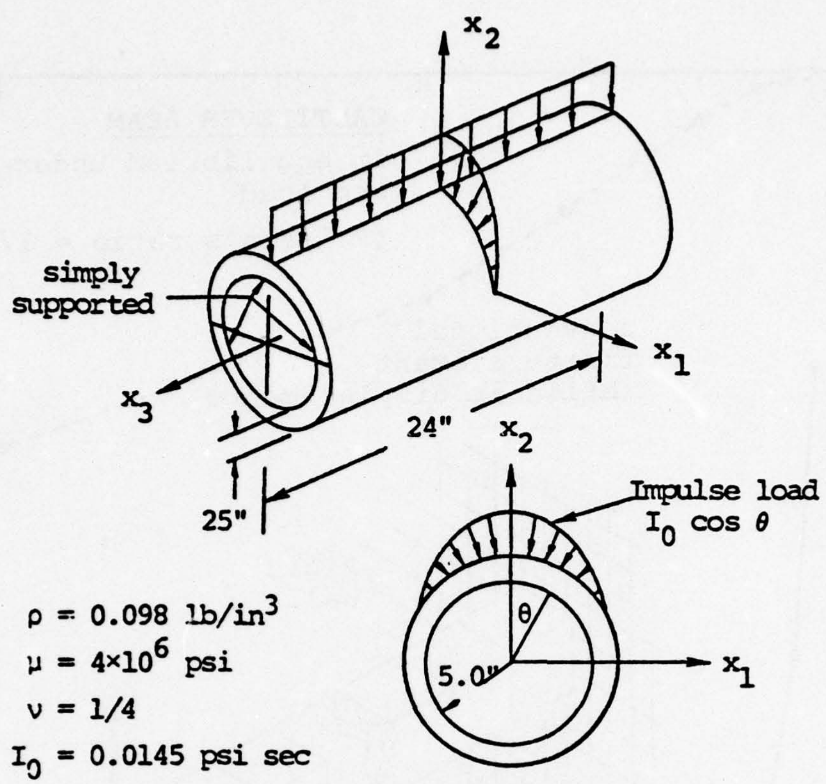

(a) Geometric problem configuration.

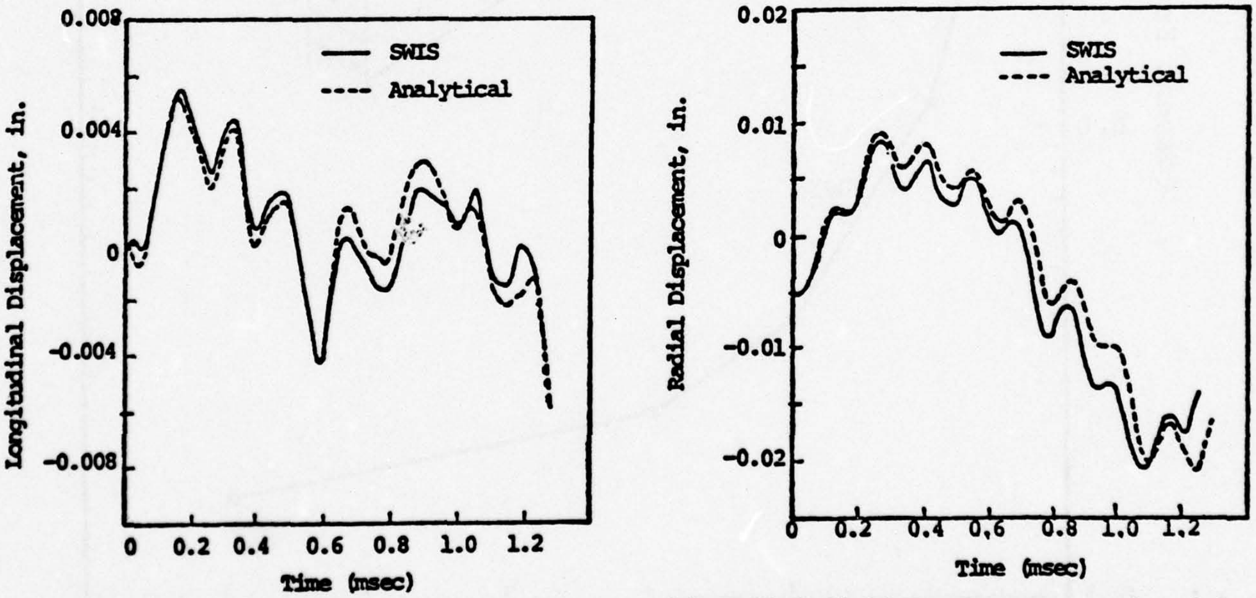

(b) Longitudinal displacement at $x_3 = L/2$ and $\theta = 0$ as a function of time.

(c) Radial displacement at $x_3 = 0$ and $\theta = 0$ as a function of time.

Figure A.10. **Comparison between theoretical and SWIS results for 3-D shell problem.**

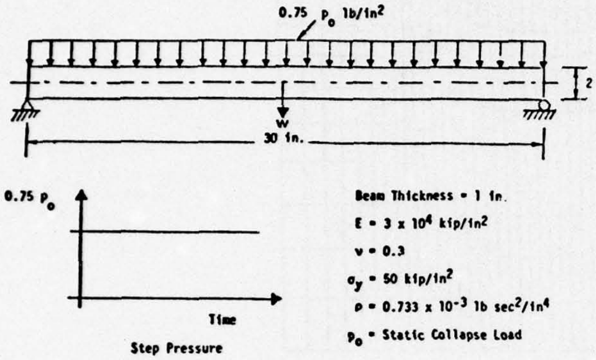

(a) Simply supported beam and applied load.

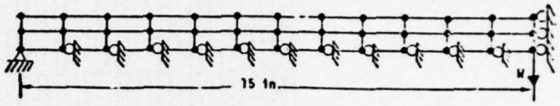

(b) Finite element idealization (twenty-four elements) for coarse mesh. Fine mesh has 36 elements along length and 3 elements through thickness.

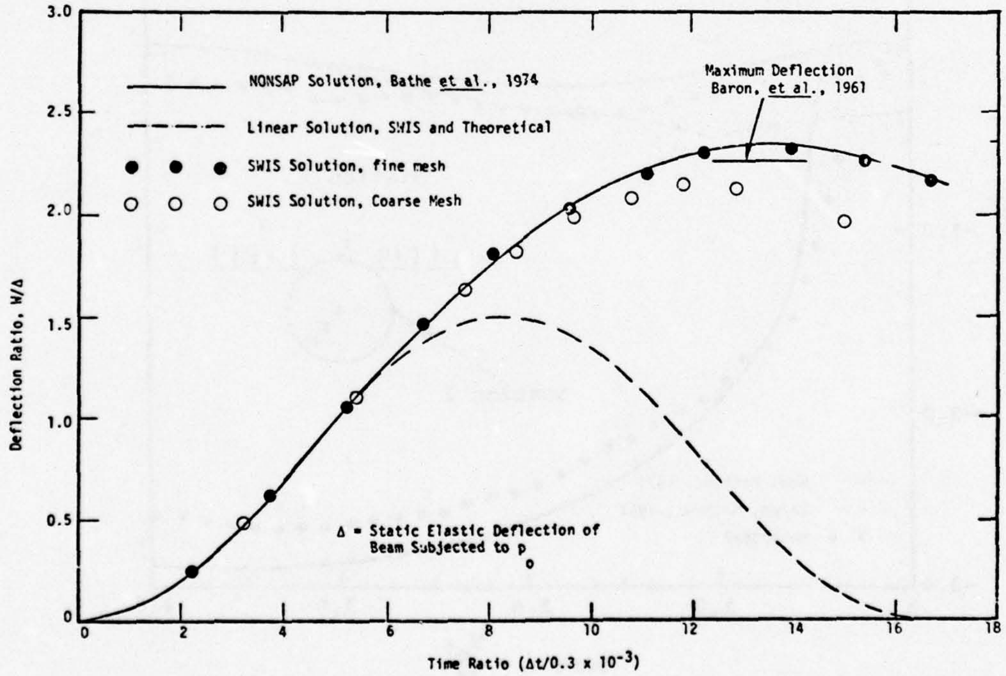

(c) Comparison of SWIS solutions with theoretical solutions. Fine Mesh.

Figure A.11. SWIS simulation of the dynamic response of a simply supported beam obeying a von Mises yield criterion.

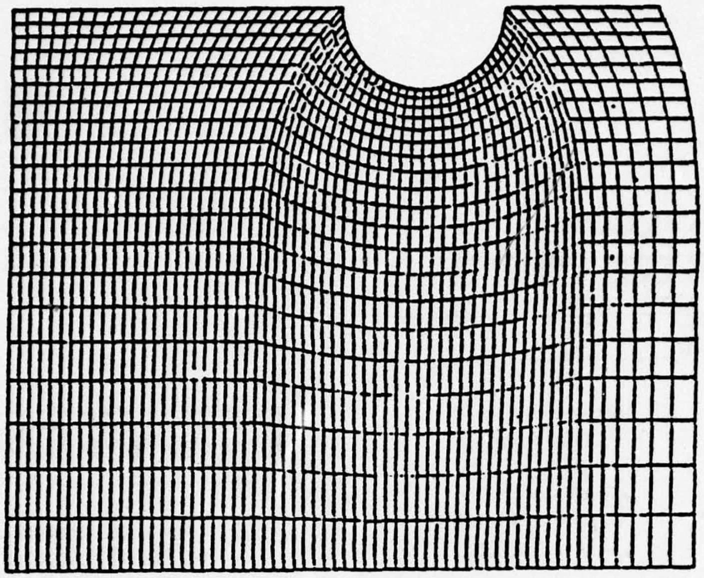

(a) Finite Element Mesh Configuration

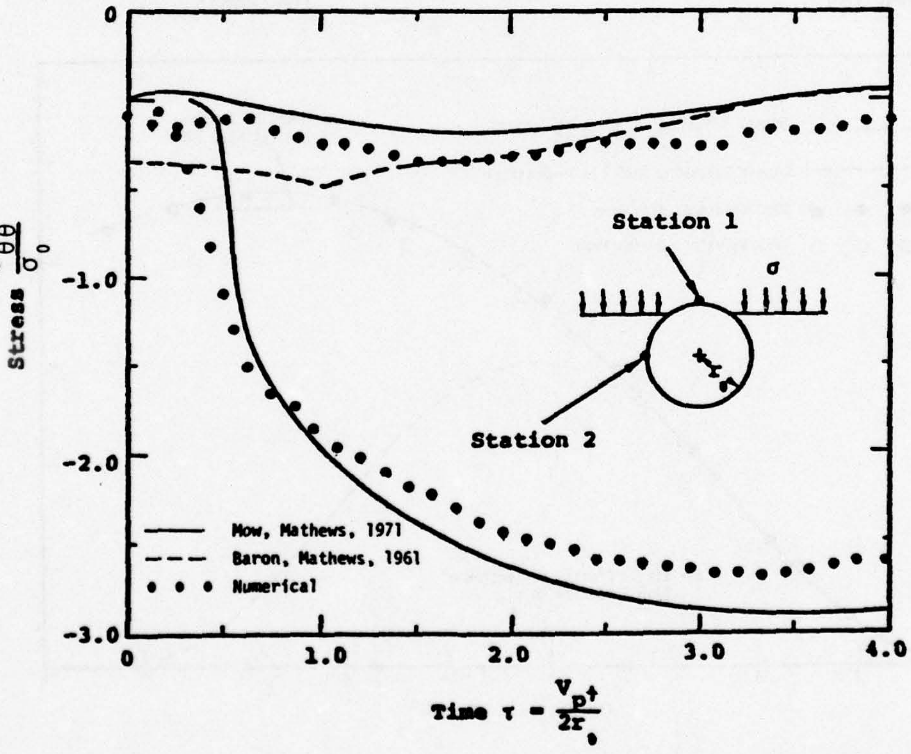

(b) Uniaxial Step Pressure Impinging on Tunnel Section

Figure A.12. Comparison of theory and SWIS results for a plane wave impinging on a tunnel.

The subcycling capability is particularly important for dynamic explicit structure-media calculations. As a test of this procedure, a calculation was performed for the dynamic response of a buried cylinder subjected to a plane wave (Sweet, 1976B). The finite element grid for this problem can be seen in Figure A.13. The characteristic time step in the cylinder is approximately 8 times smaller than that in the surrounding medium. Two calculations were performed: one without subcycling utilizing a uniform time step in the grid and another calculation with a time step in the subcycled region being one-eighth that in the surrounding medium. The excellent comparison for these two calculations can be seen in Figure A.14.

The example summarized in Figure A.15 considers the dynamic response of a structure-medium interaction configuration. The variables μ_c, V_{pm} and σ_θ not defined in this figure are the shear modulus in the cylinder, the p-wave velocity in the medium and the hoop stress in the cylinder, respectively. Parametric values of variables defined in Figure A.15 are as follows:

$\Delta = 5$, $\frac{b-a}{b} = 0.2$; pulse width and cylinder geometry

$\frac{E_m}{E_c} = 0.4$; Young's modulus ratio

$$\left.\begin{array}{l}\nu_m = 0.25\\ \nu_c = 0.2\end{array}\right\}\text{ Poisson ratios}$$

$$\left.\begin{array}{l}\rho_m = 2.68\text{ gm/cm}^3\\ \rho_c = 2.32\text{ gm/cm}^3\end{array}\right\}\text{ densities}$$

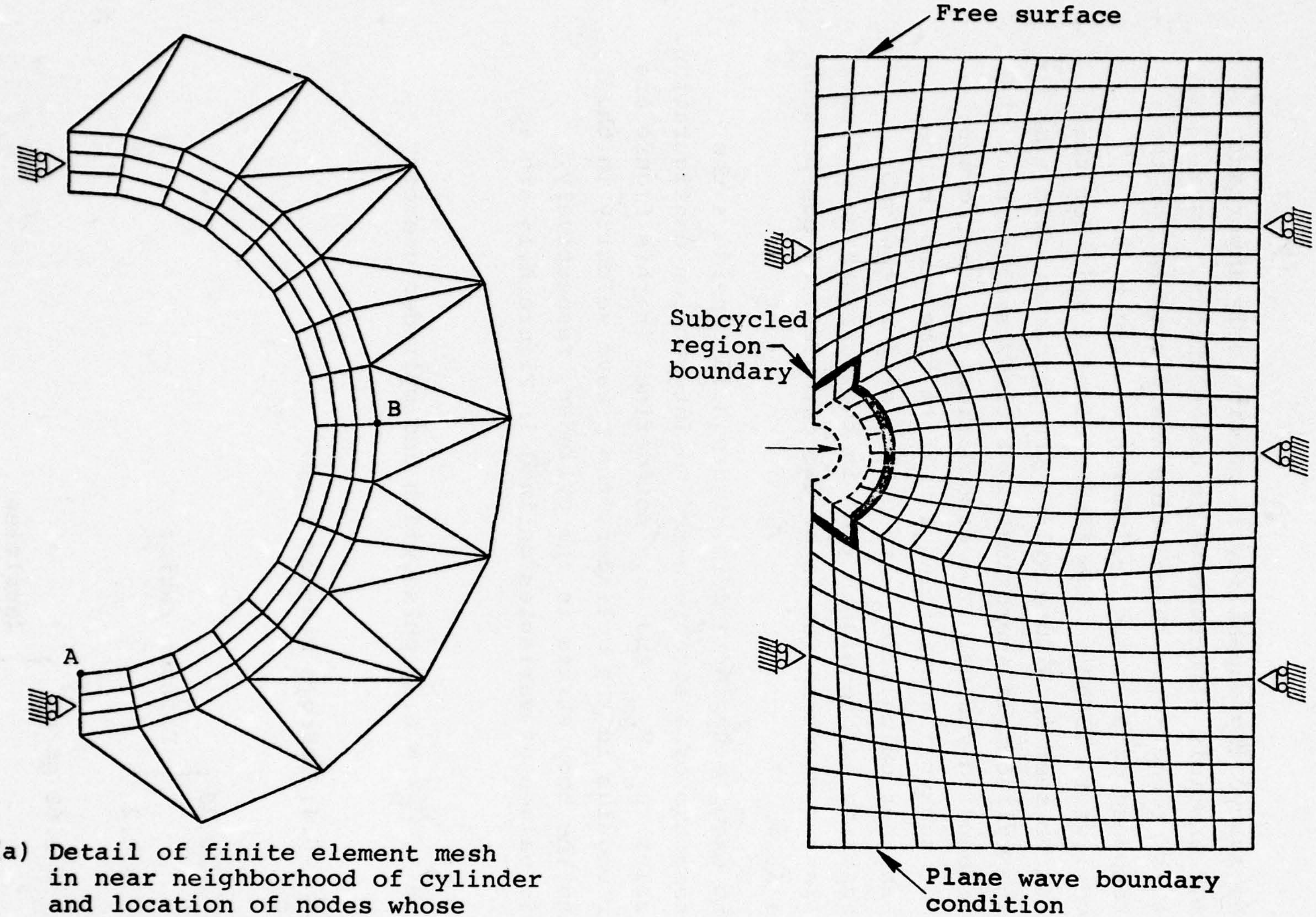

(a) Detail of finite element mesh in near neighborhood of cylinder and location of nodes whose velocity history was monitored during calculation.

(b) Finite element mesh for surrounding continuum.

Figure A.13. Finite element grid configuration of buried cylinder subjected to an impinging plane wave.

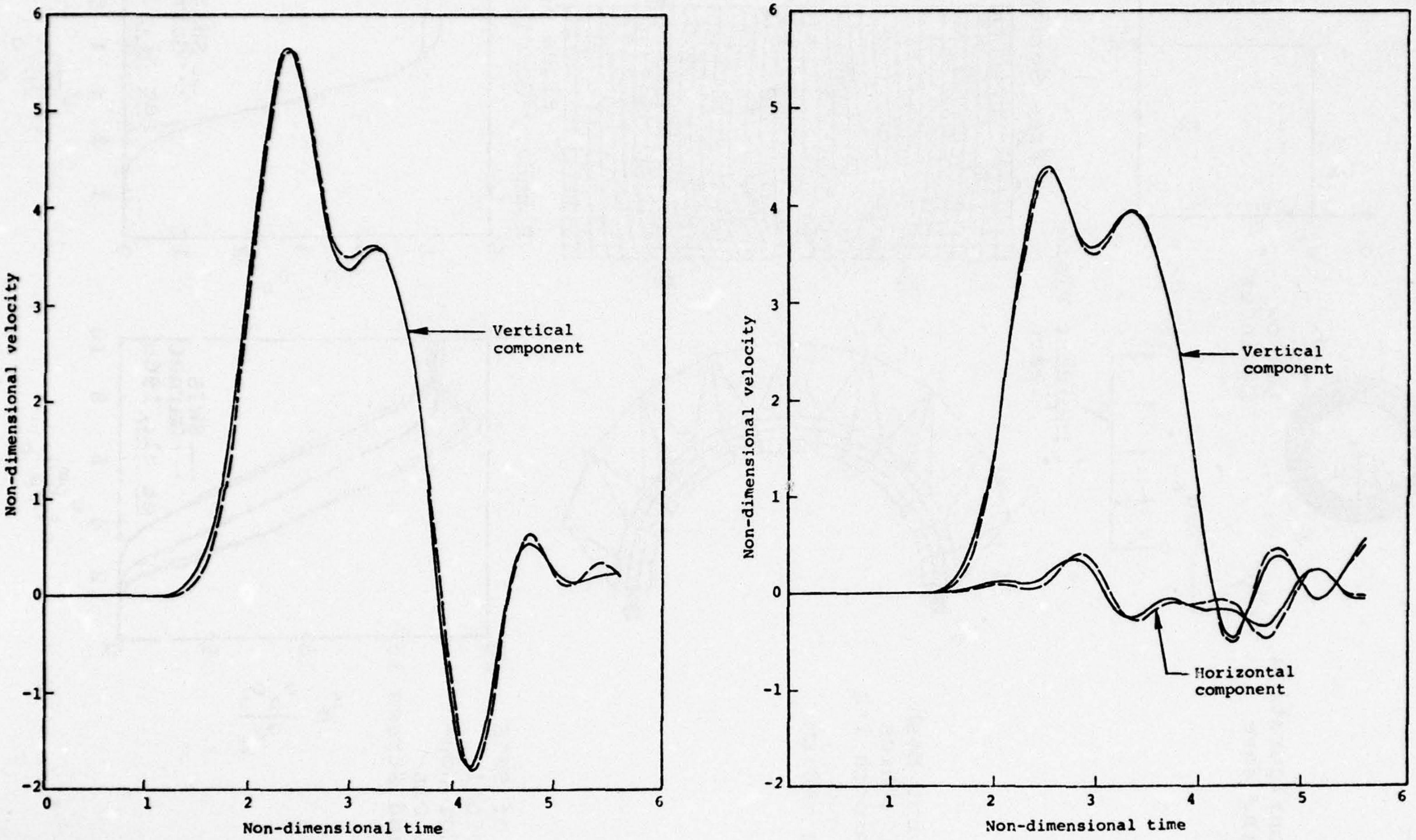

(a) Velocity time history for node A

(b) Velocity time history for node B

Figure A.14. Comparison of subcycled (dashed line) and uniform time step (solid line) results.

(a) Cylinder Configuration and Impinging Wave Description

(b) Finite Element Mesh of Cylinder (three elements through its thickness) and Surrounding Medium

(c) Comparison of SWIS and Theoretical Solutions for Non-dimensional Displacement and Stress

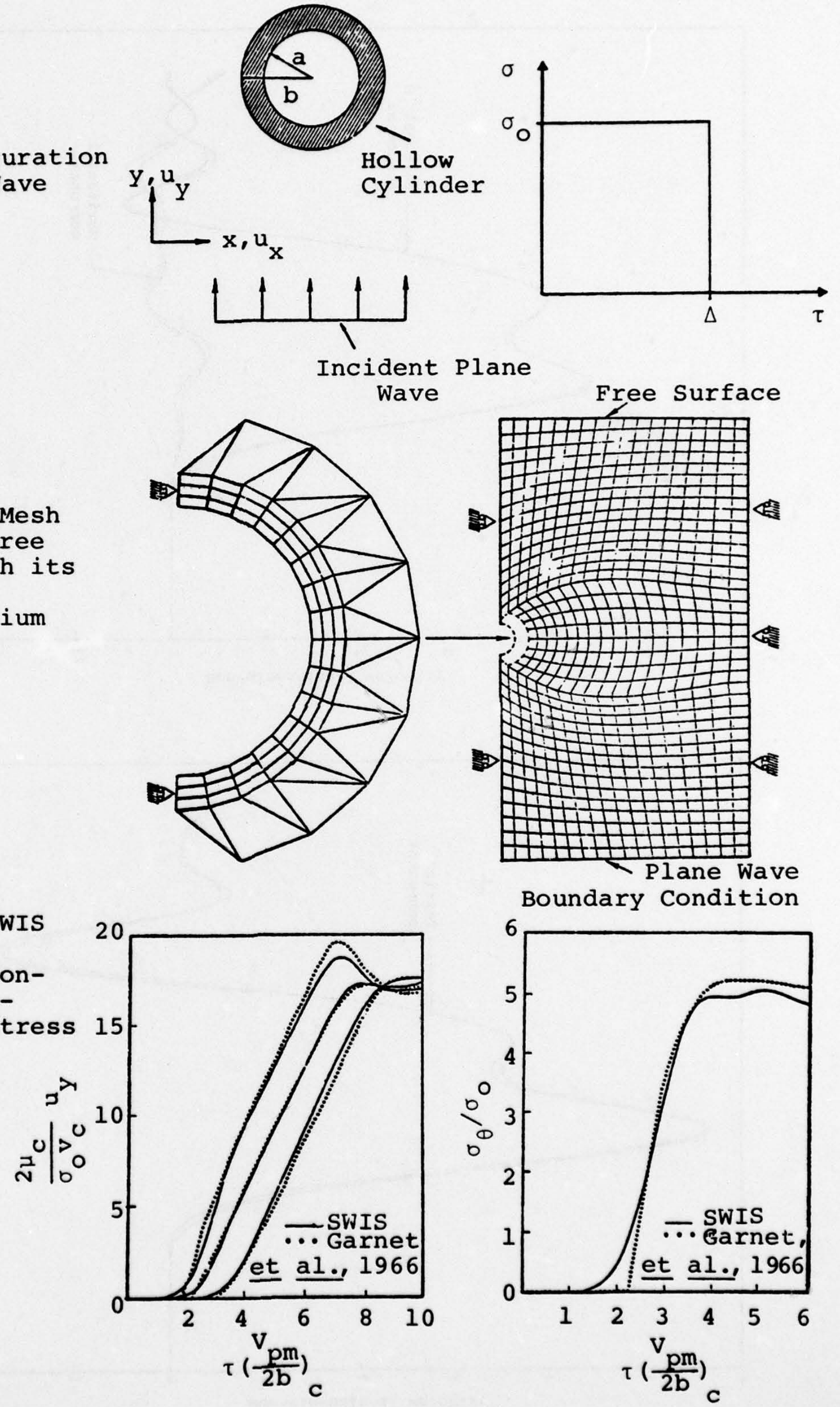

Figure A.15. SWIS simulation of the dynamic response of a buried thick-walled cylinder subjected to an impinging plane wave.

Figure A.16 summarizes the three-dimensional simulation of a buried fault. The configuration is a (prescribed) propagating 100 cm dislocation and thus does not consider the rupture process.

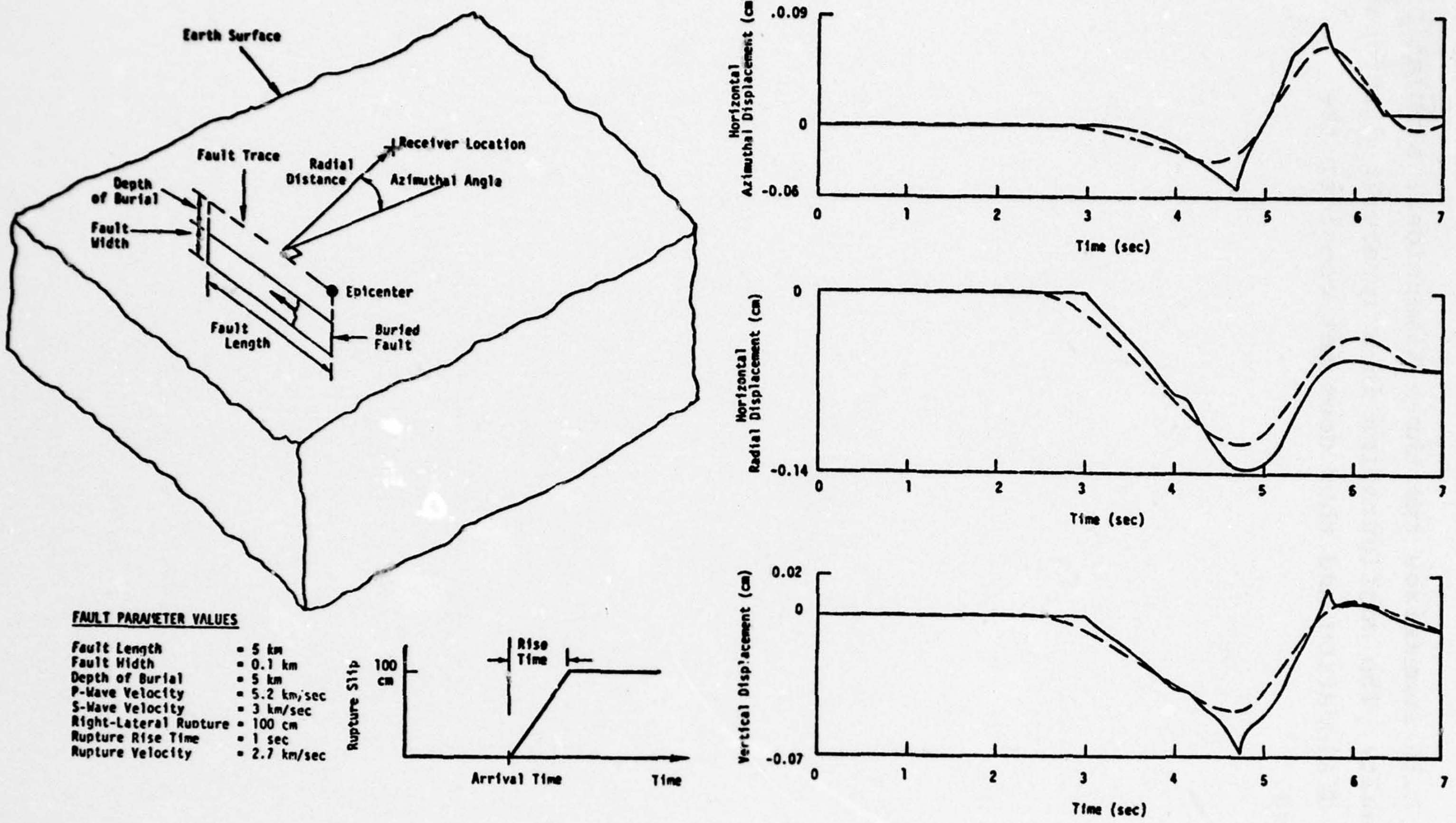

Figure A.16. Comparison between theoretical (solid line) and three-dimensional finite element (dashed line) results for a buried fault described by a propagating 100-cm dislocation. The receiver is located at a radius of 10 km and an azimuth of 30° from a buried fault. The finite element grid increment of 0.7 km resolves frequencies less than 0.5 Hz.

APPENDIX B

THE EFFECT OF IN SITU GRAVITATIONAL STRESSES ON THE BEHAVIOR OF AN UNLINED CAVITY

The analyses presented in this report assume that the explosion-induced stress wave acts in a stress-free medium. In reality, of course, in situ overburden as well as tectonic stresses exist in the neighborhood of the cavity. A precise simulation of the behavior of the cavity would first consider the actual fabrication of the cavity and the resulting relief of stresses near the cavity wall. The stress wave would then be treated as a stress superimposed on this existing state of stress. Because the tuff behaves in a nonlinear fashion, the response of the cavity can be expected to differ somewhat depending upon whether or not the in situ stresses are considered.

The effect of in situ gravitational stresses on the response of an unlined cavity is discussed in this appendix. This simulation is accomplished by prestressing the external boundaries of a two-dimensional finite element mesh containing a cylindrical cavity. The external stress consisted of an 88 bar vertical stress and an 18 bar horizontal stress. A stress-free boundary condition was maintained for the cavity wall. After this nonlinear static state of stress was imposed, a dynamic stress wave boundary condition was applied at the left hand mesh boundary (see Figure B.1) to simulate an impinging plane wave. It should be noted that both the static and explicit dynamic capabilities of the nonlinear version of the SWIS code were utilized. The tuff material model and the dynamic stress wave description are identical to those discussed in Section 2.

Results for this calculation and for a calculation without gravitational effects can be seen in Figures B.2

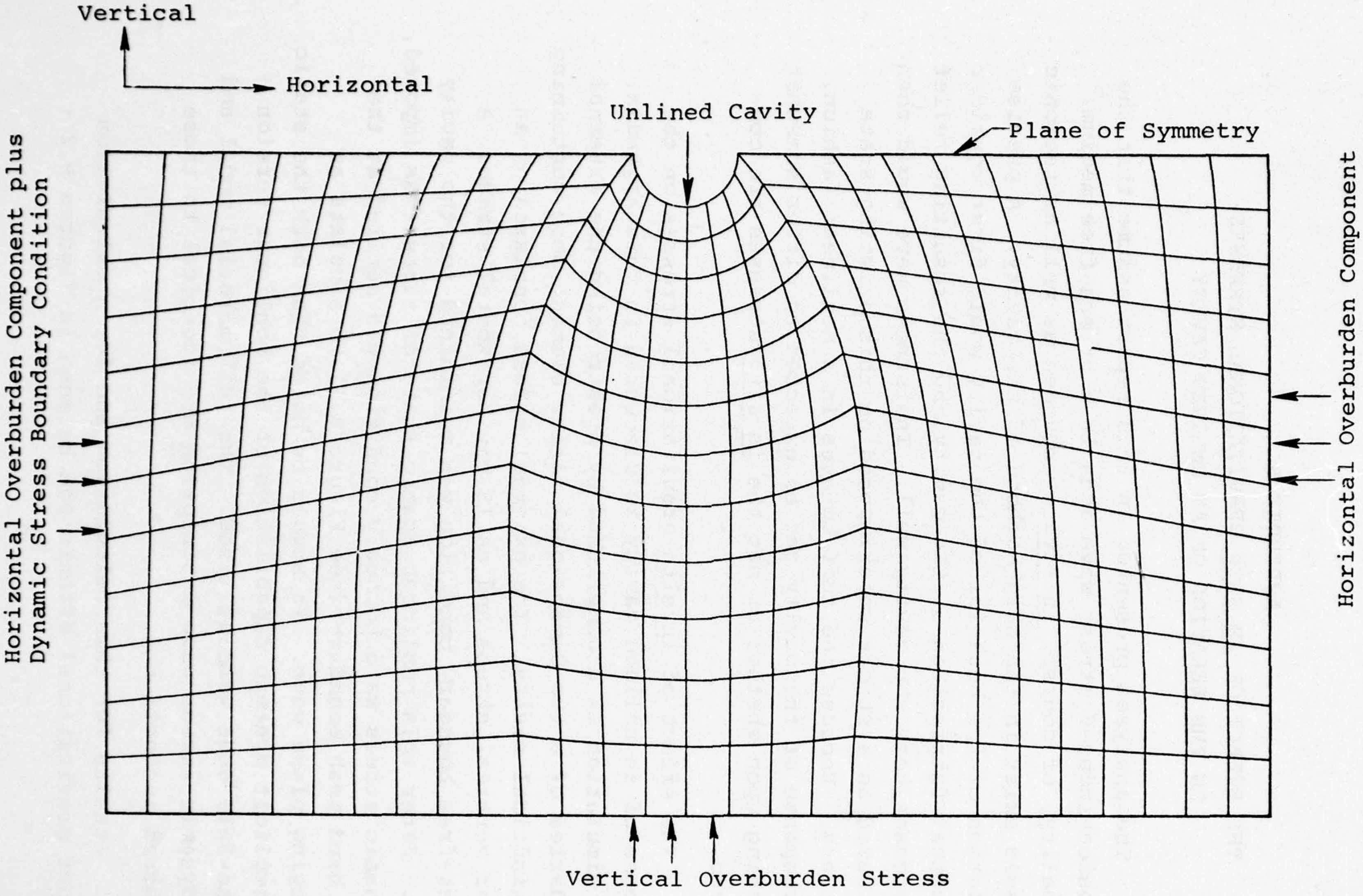

Figure B.1. Finite element mesh and boundary conditions utilized to simulate the effect of in situ overburden stresses.

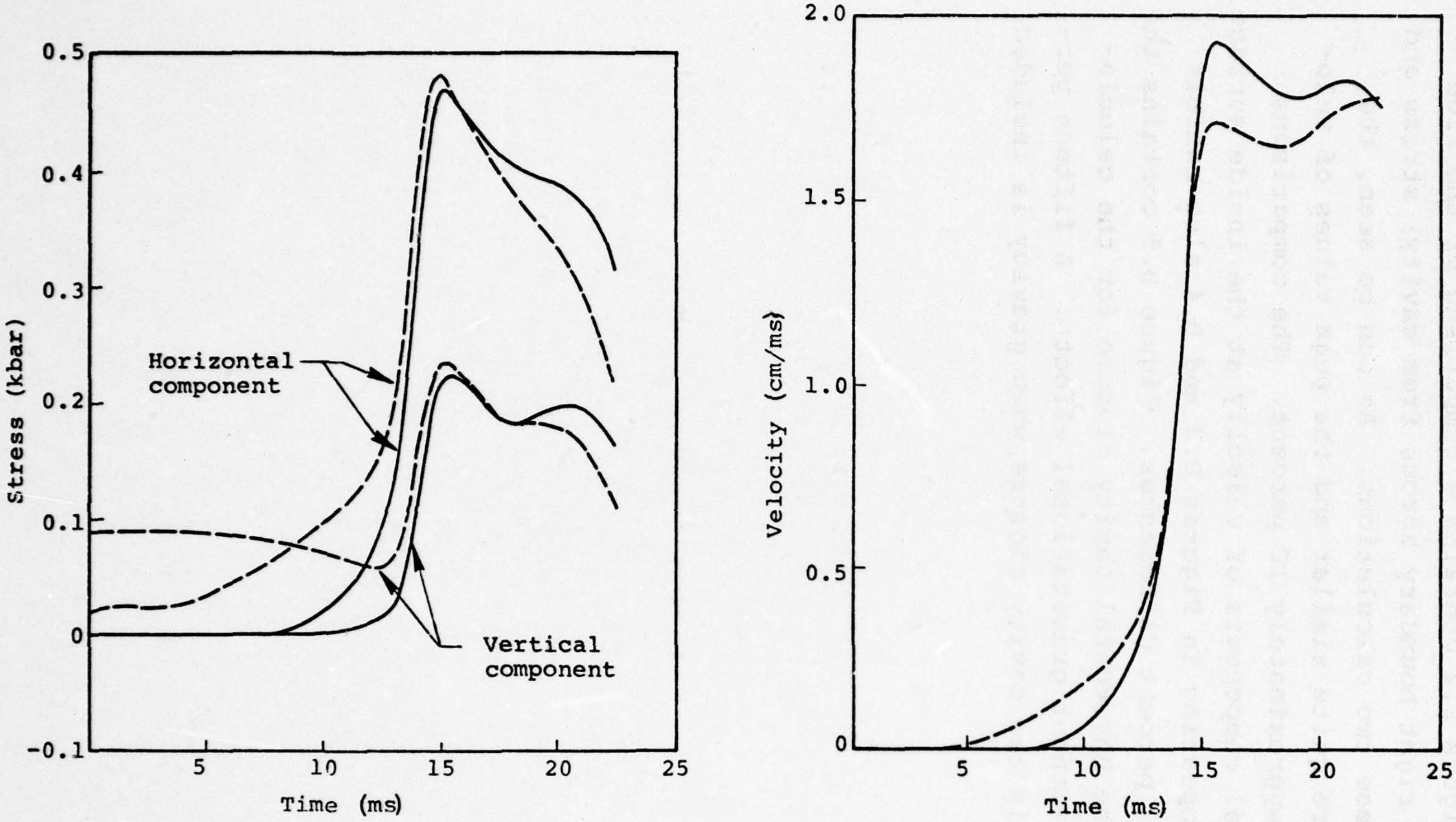

(a) Free field stress behavior

(b) Free field velocity behavior

Figure B.2. Comparison of free field stress and velocity behavior for calculations with (dashed lines) and without (solid lines) gravitational effects. Reflection from the cavity can be seen at approximately 17 ms through B.5. Figure B.2 contains a comparison of the free field (i.e., at right boundary across from cavity) stress and velocity for these two calculations. As can be seen, the peak stresses are quite similar and the peak values of velocity differ by approximately 12 percent. The comparisons of the horizontal components of velocity at the inside surface of the cavity appearing in Figures B.3 and B.4 also exhibit approximately 12 percent differences. Figure B.5 contains the comparison of the horizontal cavity closure for the calculations with and without gravitational effects. A fifteen percent reduction in the cavity closure when gravity is included can be noted.

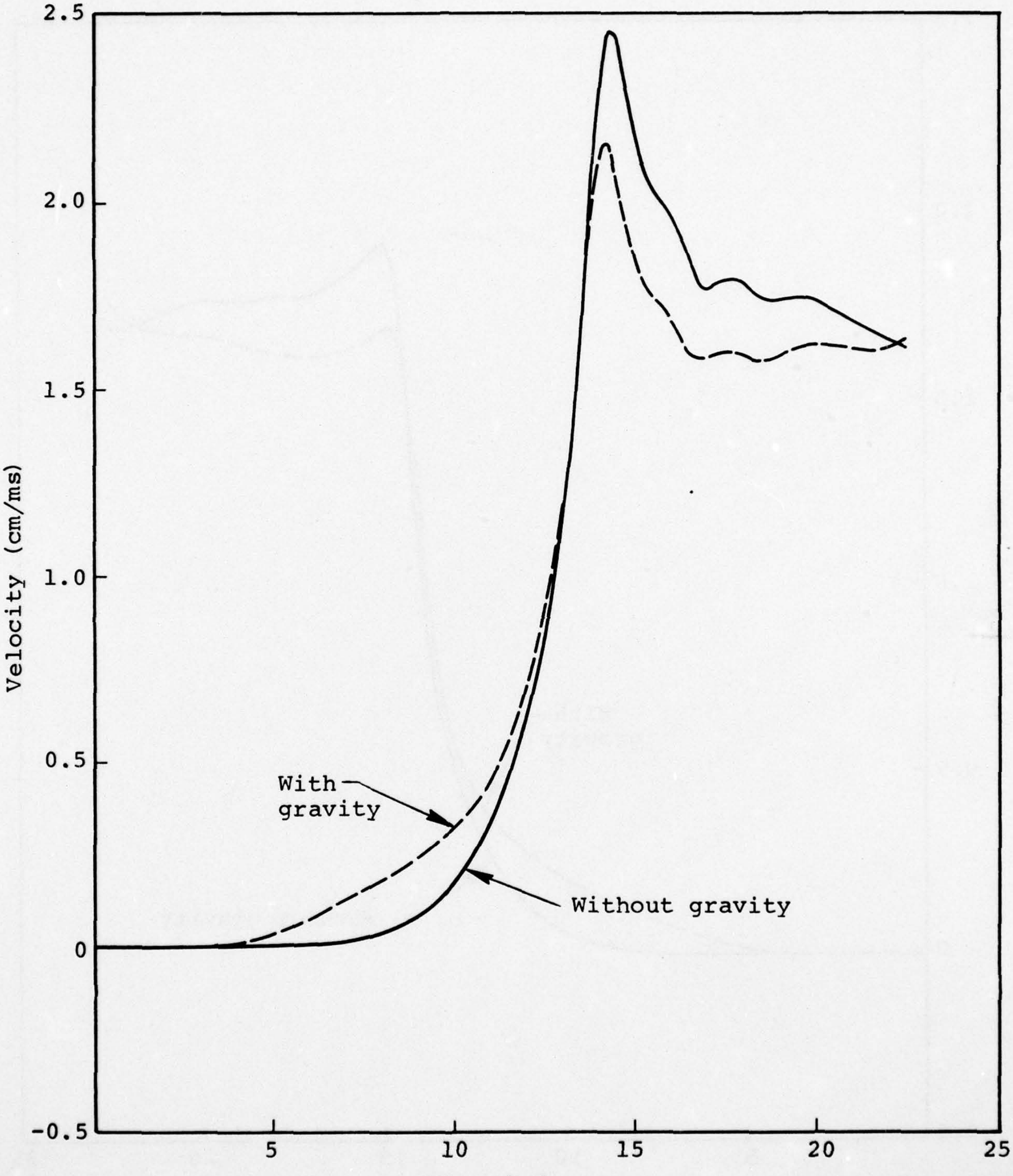

Figure B.3. Horizontal velocity comparison at the inside of the unlined cavity at the 0° (closest to left boundary) location.

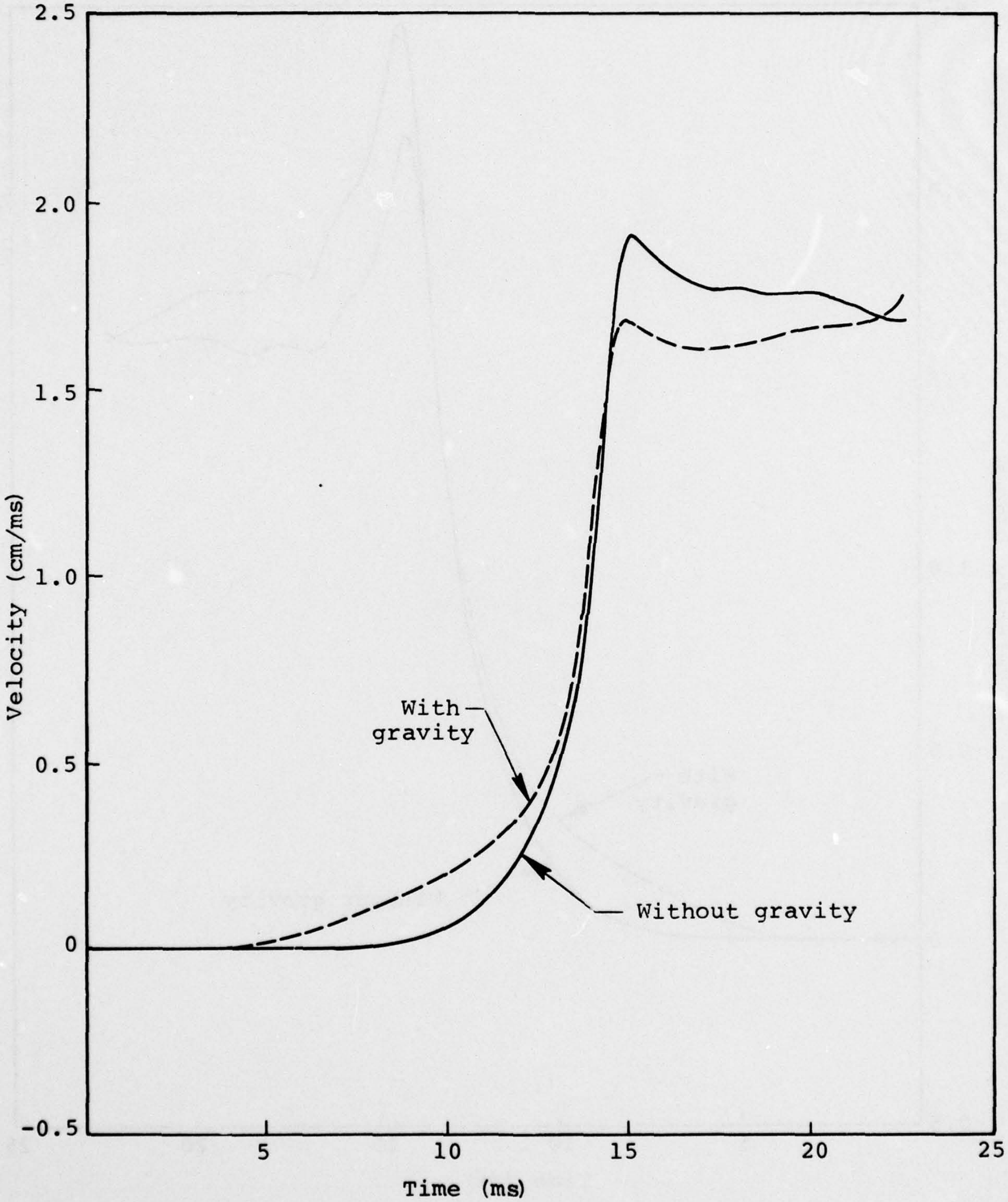

Figure B.4. Horizontal velocity comparison at the inside surface of the unlined cavity, 90° location.

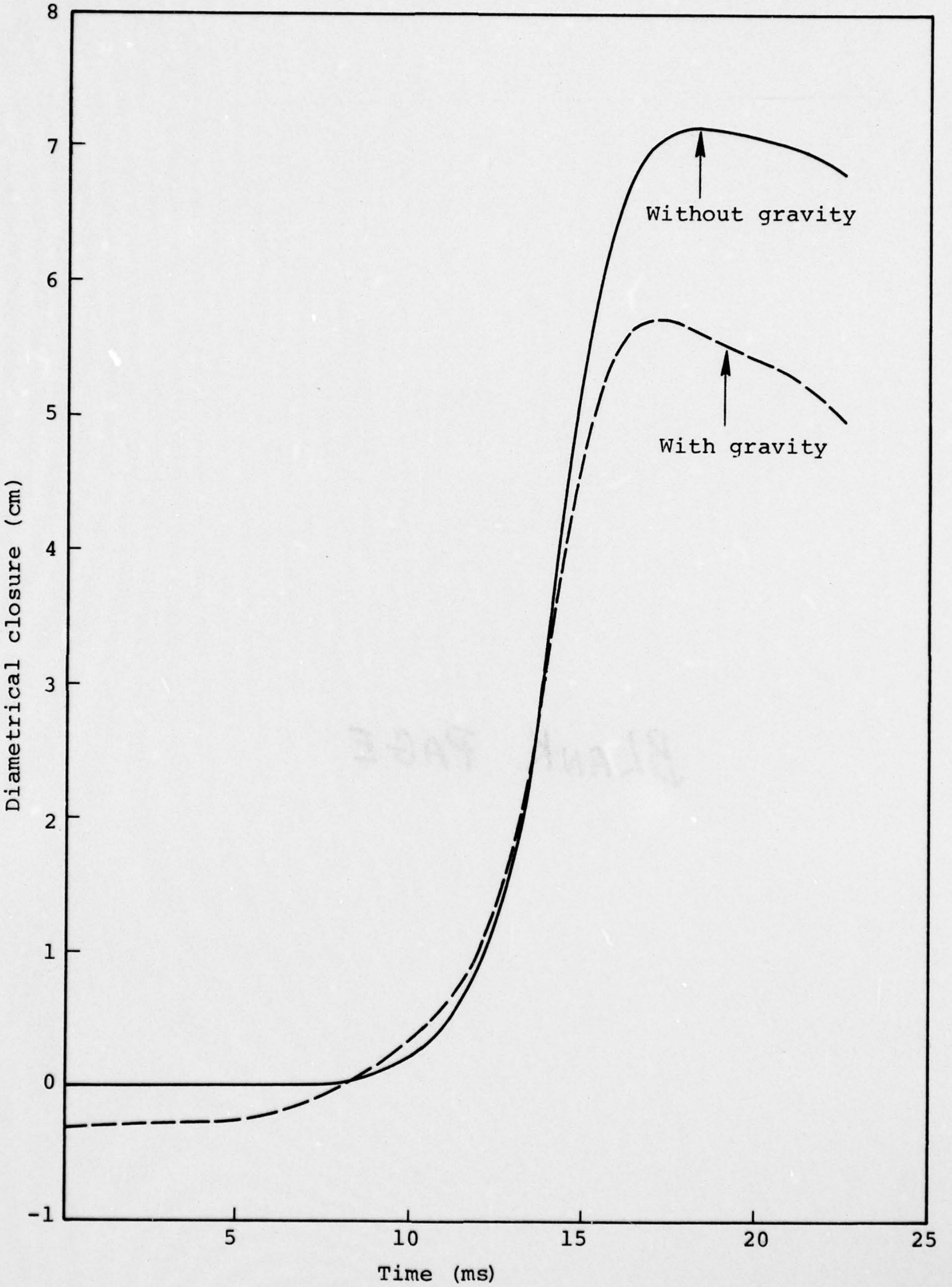

Figure B.5. Comparison of the cavity closure in the horizontal direction for the calculations with and without gravitational effects.

DISTRIBUTION LIST

DEPARTMENT OF DEFENSE

Director
Defense Advanced Rsch. Proj. Agency
ATTN: Technical Library

Director
Defense Civil Preparedness Agency
Assistant Director for Research
ATTN: Admin. Officer
ATTN: Staff Dir. Resr. George N. Sisson

Director
Defense Communications Agency
ATTN: CCTC/C672, Franklin D. Moore
ATTN: Code 930

Defense Documentation Center
12 cy ATTN: TC

Director
Defense Intelligence Agency
ATTN: Technical Library
ATTN: DB-4C2, Timothy Ross

Director
Defense Nuclear Agency
ATTN: TISI, Archives
3 cy ATTN: TITL, Tech. Library
ATTN: DDST
2 cy ATTN: SPAS
2 cy ATTN: SPSS

Dir. of Defense Rsch. & Engineering
ATTN: S&SS (OS)

Commander
Field Command
Defense Nuclear Agency
ATTN: FCPR
ATTN: FCTMOF

Director
Interservice Nuclear Weapons School
ATTN: Document Control

Chief
Livermore Division, Fld. Command, DNA
ATTN: FCPRL

Chief
Test Construction Division
Field Command Test Directorate
Defense Nuclear Agency
ATTN: FCTC

DEPARTMENT OF THE ARMY

Director
BMD Advanced Tech. Ctr.
ATTN: CRDABH-S
ATTN: 1CRDABH-X

Program Manager
BMD Program Office
ATTN: CRDABM-NE

DEPARTMENT OF THE ARMY (Continued)

Commander
BMD System Command
ATTN: BDMSC-TEN, Noah J. Hurst

Director
Construction Engineering Rsch. Lab.
ATTN: CERL-SL

Dep. Chief of Staff for Rsch. Dev. & Acq.
ATTN: Technical Library
ATTN: DAMA(CS), MAJ A. Gleim
ATTN: DAMA-CSM-N, LTC G. Ogden

Chief of Engineers
ATTN: DAEN-MCE-D
ATTN: DAEN-RDM

Deputy Chief of Staff for Ops. & Plans
ATTN: Dir. of Chem. & Nuc. Ops.
ATTN: Technical Library

Chief
Engineer Strategic Studies Group
ATTN: DAEN-FES, LTC Hatch

Commander
Harry Diamond Laboratories
ATTN: DRXDO-NP
ATTN: DRXDO-TI, Tech. Library

Commander
Picatinny Arsenal
ATTN: Technical Library

Commander
Redstone Scientific Information Ctr.
U.S. Army Missile Command
ATTN: Chief, Documents

Director
U.S. Army Ballistic Research Labs.
ATTN: W. Taylor
ATTN: DRXBR-X, Julius J. Meszaros
2 cy ATTN: Tech. Library, Edward Baicy

Commander
U.S. Army Comb. Arms Combat Dev. Acty.
ATTN: LTC Pullen
ATTN: LTC G. Steger

Commander
U.S. Army Communications Cmd.
ATTN: Technical Library

Commander
U.S. Army Engineer Center
ATTN: ATSEN-SY-L

Division Engineer
U.S. Army Engineer Div. Huntsville
ATTN: HNDED-SR

Division Engineer
U.S. Army Engineer Div. Ohio River
ATTN: Technical Library

DEPARTMENT OF THE ARMY (Continued)

Commandant
U.S. Army Engineer School
ATTN: ATSE-CTD-CS
ATTN: ATSE-TEA-AD

Director
U.S. Army Engr. Waterways Exper. Sta.
ATTN: William Flathau
ATTN: James Ballard
ATTN: Technical Library
ATTN: Leo Ingram
ATTN: Guy Jackson
ATTN: John N. Strange

Commander
U.S. Army Mobility Equip. R & D Ctr.
ATTN: Technical Library

Commander
U.S. Army Nuclear Agency
ATTN: Technical Library

Commandant
U.S. Army War College
ATTN: Library

DEPARTMENT OF THE NAV'

Chief of Naval Operations
ATTN: Code 604C3, Robert Piacesi
ATTN: OP 981
ATTN: OP 982, LCDR Smith
ATTN: OP 03EG

Chief of Naval Research
ATTN: John Haycock
ATTN: Technical Library
ATTN: Nicholas Perrone
ATTN: Code 464, Jacob L. Warner
ATTN: Code 464, Thomas P. Quinn

Officer-in-Charge
Civil Engineering Laboratory
Naval Construction Battalion Center
ATTN: Technical Library
ATTN: R. J. Odello
ATTN: Stan Takahashi

Commander
Naval Electronic Systems Command
Naval Electronic Systems Cmd. Hqs.
ATTN: PME 117-21A

Commander
Naval Facilities Engineering Command
ATTN: Technical Library

Superintendent (Code 1424)
Naval Postgraduate School
ATTN: Code 2124, Tech. Rpts. Librarian

Officer-in-Charge
Naval Surface Weapons Center
ATTN: Code WA501, Navy Nuc. Prgms. Off.

Commanding Officer
Naval Weapons Evaluation Facility
ATTN: Technical Library

DEPARTMENT OF THE AIR FORCE

Commander
ADCOM/XPD
ATTN: XP
ATTN: XPQDQ

AF Weapons Laboratory, AFSC
ATTN: DEP, Jimmie L. Bratton
ATTN: DES-C, Robert Henny
ATTN: DES-S, M. A. Plamondon
ATTN: DES-G, Mr. Melzer
ATTN: DED
ATTN: SUL

Headquarters
Air Force Systems Command
ATTN: Technical Library

Hq. USAF/RD
ATTN: RDQSM
ATTN: RDPM
ATTN: RDPS, Lt Col A. Chiota
ATTN: RDQPN, Maj F. Vajda
ATTN: RDQRM, Col S. C. Green

SAMSO/DE
ATTN: DEB

SAMSO/DY
ATTN: DYS

SAMSO/MN
ATTN: MNNH
ATTN: MMH

SAMSO/RS
ATTN: RSS/Col Donald Dowler

SAMSO/XR
ATTN: XRTB

Commander in Chief
Strategic Air Command
ATTN: NRI-STINFO Library

U.S. ENERGY RESEARCH AND DEVELOPMENT ADMINISTRATION

University of California
Lawrence Livermore Laboratory
ATTN: Tech. Info., Dept. L-3

Los Alamos Scientific Laboratory
ATTN: Doc. Control for Reports Lib.

Sandia Laboratories
ATTN: Doc. Control for Tech. Library

U.S. ENERGY Rsch. & Dev. Admin.
ATTN: Doc. Control for Tech. Library

U.S. Energy Rsch. & Dev. Admin.
Division of Headquarters Services
Library Branch G-043
ATTN: Doc. Control for Class. Tech. Library

U.S. Energy Rsch. & Dev. Admin.
Nevada Operations Office
ATTN: Doc. Control for Tech. Library

OTHER GOVERNMENT AGENCIES

Department of the Interior
Bureau of Mines
ATTN: Tech. Library

Department of the Interior
U.S. Geological Survey
ATTN: J. H. Healy
ATTN: Cecil B. Raleigh

DEPARTMENT OF DEFENSE CONTRACTORS

Aerospace Corporation
2 cy ATTN: Tech. Info. Services

Agbabian Associates
ATTN: M. Agbabian
ATTN: Carl Bagge

Applied Theory, Inc.
2 cy ATTN: John G. Trulio

Artec Associates, Inc.
ATTN: Steven Gill

The Boeing Company
ATTN: Robert Dyrdahl
ATTN: Aerospace Library
ATTN: R. H. Carlson

Brown Engineering Company, Inc.
ATTN: Manu Patel

California Research & Technology, Inc.
ATTN: Ken Kreyenhagen
ATTN: Technical Library
ATTN: Sheldon Shuster

Civil/Nuclear Systems Corp.
ATTN: Robert Crawford

EG&G, Inc.
ATTN: Technical Library

Electromechanical Sys. of New Mexico, Inc.
ATTN: R. A. Shunk

Engineering Decision Analysis Co., Inc.
ATTN: Robert Kennedy

The Franklin Institute
ATTN: Zenons Zudans

General Electric Company
TEMPO-Center for Advanced Studies
ATTN: DASIAC

H-Tech Laboratories, Inc.
ATTN: B. Hartenbaum

IIT Research Institute
ATTN: Technical Library

Illinois at Chicago, Univ. of
ATTN: Ted Belytschko

J. H. Wiggins, Co., Inc.
ATTN: Jon Collins

DEPARTMENT OF DEFENSE CONTRACTORS (Continued)

Kaman Avidyne
Division of Kaman Sciences Corp.
ATTN: Technical Library
ATTN: E. S. Criscione

Kaman Sciences Corporation
ATTN: Library

Karagozian and Case
ATTN: John Karagozian

Lockheed Missiles & Space Co., Inc.
ATTN: Technical Library

Lockheed Missiles and Space Co., Inc.
ATTN: D/52-33, Bldg. 205, Tom Geers

Merritt CASES, Incorporated
ATTN: Technical Library
ATTN: J. L. Merritt

University of New Mexico
ATTN: G. E. Triandafalidis

Newmark, Nathan M.
Consulting Engineering Services
ATTN: Nathan M. Newmark

Pacifica Technology
ATTN: R. Bjork
ATTN: G. Kent

Physics International Company
ATTN: Doc. Control for Coye Vincent
ATTN: Doc. Control for Tech. Library

R & D Associates
ATTN: J. G. Lewis
ATTN: Technical Library
ATTN: Robert Port
ATTN: Henry Cooper
ATTN: Cyrus P. Knowles

The Rand Corporation
ATTN: Technical Library
ATTN: C. C. Mow
ATTN: Armas Laupa

Science Applications, Inc.
ATTN: Technical Library

Science Applications, Incorporated
ATTN: Burt Chambers
ATTN: William M. Layson

SRI International
ATTN: George R. Abrahamson

Systems, Science and Software, Inc.
ATTN: Donald R. Grine
ATTN: Technical Library
ATTN: J. Sweet

Terra Tek, Inc.
ATTN: Technical Library
ATTN: Sidney Green

DEPARTMENT OF DEFENSE CONTRACTORS (Continued)

TRW Defense & Space Sys. Group
ATTN: Norm Lipner
2 cy ATTN: Peter K. Dai, R1/2170
ATTN: Tech. Info Center/S-1930

TRW Defense & Space Sys. Group
ATTN: E. Y. Wong, 527/712
ATTN: G. D. Hulcher

Universal Analytics, Inc.
ATTN: E. I. Field

DEPARTMENT OF DEFENSE CONTRACTORS (Continued)

The Eric H. Wang
Civil Engineering Rsch. Fac.
University Station
ATTN: Larry Bickle
ATTN: Neal Baum

Weidlinger Assoc. Consulting Engineers
ATTN: J. M. McCormick
ATTN: Melvin L. Baron

Weidlinger Assoc. Consulting Engineers
ATTN: J. Isenberg